E-ISSN: 2147-1959

MIRT

Molecular Imaging and Radionuclide Therapy

June 2024 Volume 33 Issue 2 www.tsnm.org

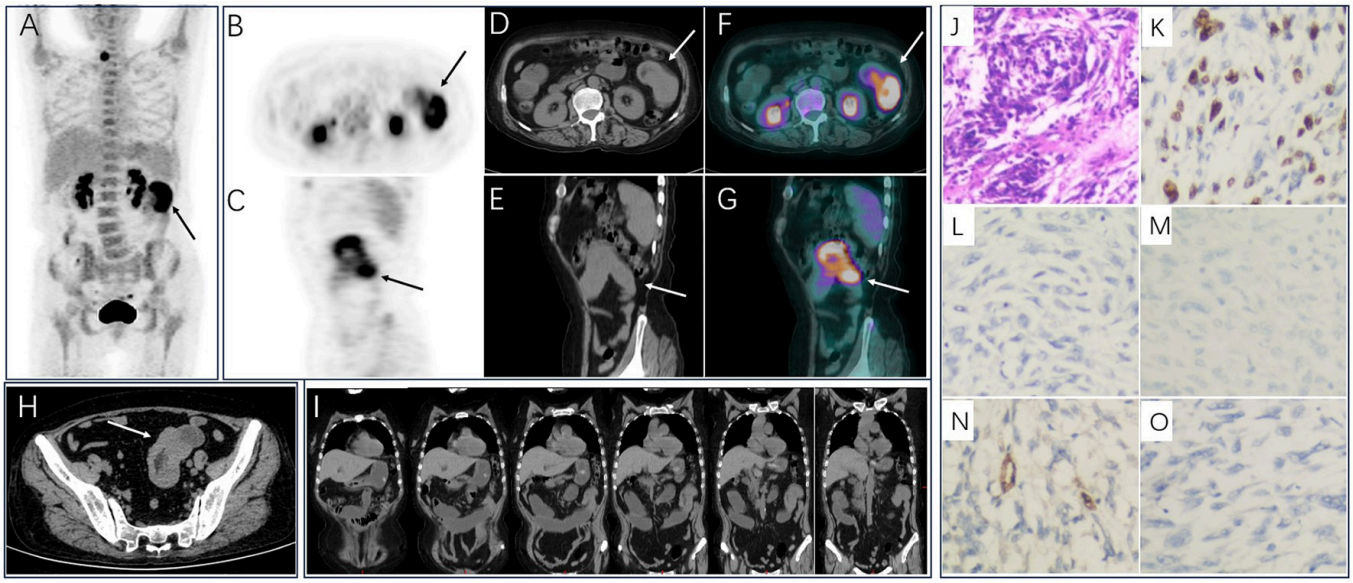

"Official Journal of the Turkish Society of Nuclear Medicine"

galenos yayınevi

TURKISH SOCIETY OF NUCLEAR MEDICINE 1975

MIRT

Molecular Imaging and Radionuclide Therapy

MIRT

Molecular Imaging and Radionuclide Therapy

Turkish Society of Nuclear Medicine
Cinnah Caddesi Pilot Sokak No: 10/12 Çankaya 06650 Ankara, Türkiye **Phone:** +90 312 441 00 45 **Fax:** +90 312 441 12 95 **Web:** www.tsnm.org **E-mail:** dernekmerkezi@tsnm.org
"Formerly Turkish Journal of Nuclear Medicine"

Reviewing the articles' conformity to the publishing standards of the Journal, typesetting, reviewing and editing the manuscripts and abstracts in English, creating links to source data, and publishing process are realized by Galenos.

Publisher Contact
Address: Molla Gürani Mah. Kaçamak Sk. No: 21/1 34093 İstanbul, Türkiye
Phone: +90 (530) 177 30 97 / +90 539 307 32 03
E-mail: info@galenos.com.tr/yayin@galenos.com.tr
Web: www.galenos.com.tr
Publisher Certificate Number: 14521

Online Publication Date: June 2024
ISSN: 2146-1414 **E-ISSN:** 2147-1959
International scientific journal published quarterly.

MIRT

Molecular Imaging and Radionuclide Therapy

Please refer to the journal's webpage **(https://mirt.tsnmjournals.org/)** for "Aims and Scope", "Instructions to Authors" and "Ethical Policy".

The editorial and publication process of Molecular Imaging and Radionuclide Therapy are shaped in accordance with the guidelines of ICMJE, WAME, CSE, COPE, EASE, and NISO. The journal is in conformity with the Principles of Transparency and Best Practice in Scholarly Publishing.

Molecular Imaging and Radionuclide Therapy is indexed in **Pubmed, Pubmed Central (PMC), Emerging Sources Citation Index (ESCI), TUBITAK-ULAKBIM, Scopus, Gale/Cengage Learning, EBSCO databases, ProQuest Health & Medical Complete, CINAHL, Embase, J-Gate, IdealOnline, Türkiye Atıf Dizini-Turkiye Citation Index, Turk Medline, Hinari, GOALI, ARDI, OARE, AGORA** and **CNKI**.

The journal is published electronically.

Owner: Murat Fani Bozkurt on Behalf of Turkish Society of Nuclear Medicine

Responsible Manager: Murat Fani Bozkurt

MIRT
Molecular Imaging and Radionuclide Therapy

CONTENTS

Original Articles

68 A Comprehensive Analysis of Volumetric ^{68}Ga-PSMA PET/CT Parameters, Clinical and Histopathologic Features: Evaluation of the Predictive Role

Volümetrik ^{68}Ga-PSMA PET/BT Parametreleri, Klinik ve Histopatolojik Özelliklerin Kapsamlı Bir Analizi: Prediktif Rolün Değerlendirilmesi

Gözde Mutevelizade, Yasemin Parlak, Ceren Sezgin Arıkbası, Gül Gümüşer, Elvan Sayit; Manisa, Türkiye

77 Diagnostic Performance of FAPI PET/CT vs. ^{18}F-FDG PET/CT in Evaluation of Liver Tumors: A Systematic Review and Meta-analysis

Karaciğer Tümörlerinin Değerlendirilmesinde FAPI PET/BT ve ^{18}F-FDG PET/BT'nin Tanısal Performanslarının Karşılaştırılması: Sistematik Bir Derleme ve Meta-analiz

Parneet Singh, Tejasvini Singhal, Girish Kumar Parida, Ashique Rahman, Kanhaiyalal Agrawal; Bhubaneswar, India

90 Can Pantoprazole be Used for Premedication in Meckel Scintigraphy?

Pantoprazol Meckel Sintigrafisinde Premedikasyon Amacıyla Kullanılabilir mi?

Aziz Gültekin, Tarık Şengöz, Samiye Demirezen, Doğangün Yüksel; Denizli, Türkiye

94 Quantitative Performance Evaluation of Commonly Used Colormaps for Image Display in Myocardial Perfusion Imaging: Analysis Based on Perceptual Metrics

Miyokardiyal Perfüzyon Görüntülemede Görüntü Ekranı için Yaygın Olarak Kullanılan Renk Haritalarının Kantitatif Performans Değerlendirmesi: Algısal Metriklere Dayalı Analiz

Mohsen Qutbi; Tehran, Iran

Interesting Images

106 Unusual Soft Tissue Uptake of Tc-99m MDP in Radiation-induced Sarcoma: Diagnostic Conundrum

Radyasyona Bağlı Sarkomda Yumuşak Dokuda Beklenmedik Tc-99m MDP Tutulumu: Tanısal İkilem

Sharjeel Usmani, Anjali Jain, Khulood Al Riyami, Zahida Niaz, Subhash Kheruka, Vipin V Jayakrishnan; Muscat, Oman

109 Diagnosis and Evaluation of Treatment Response in Relapsing Polychondritis Using ^{18}F-FDG PET/CT

Tekrarlayan Polikondrit Tanısında ve Tedavi Yanıt Değerlendirmesinde ^{18}F-FDG PET/BT

Caner Civan, Emine Göknur Işık, Duygu Has Şimşek, Mustafa Altınkaynak, Serkan Kuyumcu; İstanbul, Türkiye

112 Late ^{68}Ga PSMA-positive Pancreatic Metastasis From Renal Cell Carcinoma in a Patient with Metastatic Prostate Cancer: A Mission Impossible

Metastatik Prostat Kanserli Bir Hastada Renal Hücreli Karsinomdan Geç ^{68}Ga PSMA-pozitif Pankreas Metastazı: İmkansız Bir Görev

Gabriela Mateva, Nikolina Novoselska, Assen Dudov, Marina Garcheva-Tsacheva, Pavel Bochev; Sofia, Bulgaria

115 Misdiagnosis of a Drain-site Hernia Containing Fallopian Tube Fimbria on ^{18}F-FDG PET/CT

^{18}F-FDG PET/BT'de Fallop Tüpü Fimbriası İçeren Drenaj Yeri Fıtığının Yanlış Teşhisi

Hui Li, Le Song, Bing-Qi Li, Na Guo, Weifang Zhang; Beijing, China

118 Lincoln Sign: A Rare Presentation of Medication-related Osteonecrosis of the Jaw

Lincoln İşareti: İlaçla İlişkili Çene Osteonekrozunun Nadir Bir Göstergesi

Tsz-Kit Chow, Jocelyn Chu; Hong Kong, China

MIRT
Molecular Imaging and Radionuclide Therapy

CONTENTS

121 An Uncommon Case of Pediatric Nasopharyngeal Carcinoma with Bone Metastases and Enchondromas Evaluated Using ^{18}F-FDG PET/CT

^{18}F-FDG PET/BT Taraması ile Değerlendirilen, Kemik Metastazları ve Enkondromları Olan Nadir Bir Pediatrik Nazofaringeal Karsinom Olgusu

Natale Quartuccio, Salvatore Ialuna, Salvatore Poma, Vincenzo Luca Lentini, Alessandro Pitruzzella, Giuseppe Mario Galfano, Antonino Maria Moreci, Domenico Michele Modica; Palermo, Italy

125 ^{18}F-FDG and ^{68}Ga-FAPI-04 PET/CT Findings of a Rare Epithelial-myoepithelial Carcinoma Arising From Ex Pleomorphic Adenoma of Parotid

Parotidin Eski Pleomorfik Adenomundan Kaynaklanan Nadir Bir Epitelyal-miyoepitelyal Karsinomun ^{18}F-FDG ve ^{68}Ga-FAPI-04 PET/CT Bulguları

Caner Civan, Duygu Has Şimşek, Doğu Vurallı Bakkaloğlu, Serkan Kuyumcu; İstanbul, Türkiye

129 Jejunal Undifferentiated Spindle Cell Sarcoma with Intussusception Revealed by ^{18}F-FDG PET/CT

^{18}F-FDG PET/BT ile Gösterilen İntussusepsiyonlu Jejunal Farklılaşmamış İğsi Hücreli Sarkom

Haiyan Li, Xia Lu; Yangzhou, China

132 Isolated Diffuse Bone Marrow Metastases From Signet-ring Cell Gastric Carcinoma

Taşlı Yüzük Hücreli Mide Karsinomunun İzole Yaygın Kemik İliği Metastazları

Tsz-Kit Chow; Hong Kong, China

Case Report

134 Revision of the Histopathological Examination Following ^{68}Ga-DOTA-FAPI-04 PET/CT of a Breast Tumor Diagnosed as Invasive Ductal Carcinomatosis

İnvaziv Duktal Karsinoma Tanılı Meme Tümörünün ^{68}Ga-DOTA-FAPİ-04 PET/BT Sonrası Histopatolojik İncelemesinin Revizyonu

Nalan Alan Selçuk, Kaan Akçay, Gamze Beydağı, Ömer Sönmez, Serkan Çelik, Bala Başak Öven, Levent Kabasakal; İstanbul, Türkiye

Original Article

Mol Imaging Radionucl Ther 2024;33:68-76 *DOI:10.4274/mirt.galenos.2024.56933*

A Comprehensive Analysis of Volumetric ^{68}Ga-PSMA PET/CT Parameters, Clinical and Histopathologic Features: Evaluation of the Predictive Role

Volümetrik ^{68}Ga-PSMA PET/BT Parametreleri, Klinik ve Histopatolojik Özelliklerin Kapsamlı Bir Analizi: Prediktif Rolün Değerlendirilmesi

Gözde Mutevelizade[1], Yasemin Parlak[1], Ceren Sezgin Arıkbası[2], Gül Gümüşer[1], Elvan Sayit[1]

[1]*Manisa Celal Bayar University Faculty of Medicine, Department of Nuclear Medicine, Manisa, Türkiye*
[2]*Manisa City Hospital, Clinic of Nuclear Medicine, Manisa, Türkiye*

Abstract

Objectives: To evaluate the relationships between volumetric ^{68}Ga-prostate-specific membrane antigen (PSMA) positron emission tomography/computed tomography (PET/CT) parameters, Gleason score (GS), prostate-specific antigen (PSA) levels, histopathological data, and metastatic status in newly diagnosed prostate cancer (PCa) patients and to assess the predictive factors for progression despite treatment.

Methods: A total of 78 newly diagnosed patients with PCa who had ^{68}Ga-PSMA PET/CT scans were included. Clinical parameters, histopathological data, and metastatic status were documented, and volumetric parameters of primary prostate lesions were measured. All obtained data were compared statistically.

Results: Primary prostate tumor maximum standardized uptake value (SUV_{max}) and GS were significantly related to serum PSA levels ($p<0.05$). PSA levels and SUV_{max} values were significantly higher in patients with lymph node metastases than in those without. GS was found to be significantly increased in metastatic patients. PSMA-derived tumor volume (PSMA-TV) and total lesion PSMA of the primary lesion had a significant relationship with PSA value, GS, and regional lymph node metastases. Receiver operating characteristic analysis, conducted in patients with metastatic and localized disease, identified the cutoff value for SUV_{max} as 10.85. According to the results of the logistic regression analysis, PSMA-TV was found to be a predictive factor for progression despite treatment.

Conclusion: ^{68}Ga-PSMA PET/CT remains an invaluable imaging modality that should be considered first in PCa staging because of its superior compatibility with clinical and histopathologic data. The importance of this method goes beyond diagnostic accuracy; it also extends into the predictive domain, where the PSMA-TV value of primary prostate lesions is a potential predictor of treatment efficacy. This information is valuable for personalizing patient treatment, improving prognostic accuracy, and predicting clinical outcomes.

Keywords: ^{68}Ga-PSMA PET/CT, prostate cancer, volumetric parameters

Öz

Amaç: Bu çalışmanın amacı yeni tanı konmuş prostat kanseri (PKa) hastalarında volümetrik ^{68}Ga-prostat-spesifik membran antijeni (PSMA) pozitron emisyon tomografisi/bilgisayarlı tomografi (PET/BT) parametreleri, Gleason skoru (GS), prostat-spesifik antijeni (PSA) düzeyleri, histopatolojik veriler ve metastatik durum arasındaki ilişkileri ve prediktif faktörleri değerlendirmektir.

Yöntem: ^{68}Ga-PSMA PET/BT taramaları yapılmış toplam 78 yeni tanı PKa hastası çalışmaya dahil edildi. Klinik parametreler, histopatolojik veriler ve metastatik durum belgelendi ve prostat bezindeki primer tümörden elde edilen volümetrik parametreler ölçüldü. Elde edilen tüm veriler istatistiksel olarak karşılaştırıldı.

Address for Correspondence: Gözde Mutevelizade MD, Manisa Celal Bayar University Faculty of Medicine, Department of Nuclear Medicine, Manisa, Türkiye
Phone: +90 532 471 32 62 **E-mail:** gozdemutevelizadee@gmail.com ORCID ID: orcid.org/0000-0001-5986-8777
Received: 18.03.2024 **Accepted:** 05.05.2024 **Epub:** 14.06.2024

Bulgular: GS ve primer prostat tümöründen elde edilen maksimum standardize tutulum değeri (SUV_{maks}), serum PSA düzeyleri ile anlamlı olarak ilişkiliydi (p<0,05). PSA düzeyleri ve SUV_{maks} değerleri lenf nodu metastazı olan hastalarda olmayanlara göre anlamlı olarak daha yüksekti. GS metastatik hastalarda anlamlı olarak yüksek bulundu. Primer lezyonun PSMA-tümör volümü (PSMA-TV) ve total lezyon-PSMA değerlerinin PSA değeri, GS ve bölgesel lenf nodu metastazları ile anlamlı ilişkisi vardı. Metastatik ve lokalize hastalığı olan hastalarda yapılan alıcı işletim karakteristik analizi, SUV_{maks} için kesim değerini 10,85 olarak belirlemiştir. Lojistik regresyon analizi sonuçlarına göre, PSMA-TV progresyon için prediktif bir faktör olarak bulunmuştur.

Sonuç: ^{68}Ga-PSMA PET/BT, klinik ve histopatolojik verilerle üstün uyumluluğu nedeniyle PKa evrelemesinde ilk olarak düşünülmesi gereken çok değerli bir görüntüleme yöntemi olmaya devam etmektedir. ^{68}Ga-PSMA PET/BT'nin klinik yeri ve önemi, sadece tanısal doğruluğu ile sınırlı değildir. ^{68}Ga-PSMA PET/BT'den elde edilen primer prostat lezyonunun PSMA-TV değeri tedavi başarısını öngörebilecek potansiyel bir gösterge olarak önem taşımaktadır. Bu bilgi, hasta tedavisini kişiselleştirmek, prognostik doğruluğu artırmak ve klinik sonuçları tahmin etmek için değerlidir.

Anahtar kelimeler: ^{68}Ga-PSMA PET/BT, prostat kanseri, volümetrik parametreler

Introduction

Prostate cancer (PCa) is the most common cancer in men in the United States and the second most common cancer in men worldwide (1,2). Prostate-specific membrane antigen (PSMA) is a type II transmembrane protein with overexpression in most PCa cells and is of increasing interest as a target molecule for imaging and treatment (3). Gallium-68-PSMA (^{68}Ga-PSMA) [Glu-NH-CONH-Lys-(Ahx)-[Ga-68(HBED-CC)] positron emission tomography/computed tomography (PET/CT) scan is an advanced and promising imaging method having high sensitivity in determining lesions of PCa with a high tumor-to-background ratio (4). ^{68}Ga-PSMA PET/CT has been used with increasing frequency in recent years for staging, restaging, and treatment response evaluation in patients with PCa. ^{68}Ga-PSMA PET/CT shows higher diagnostic accuracy for restaging during biochemical recurrence and is superior to conventional imaging modalities in the preoperative staging of PCa (5). Classifying patients with PCa according to their risk status affects treatment management and makes an important contribution to predicting the response to treatment. Gleason score (GS) and serum prostate-specific antigen (PSA) levels are accepted as strong predictors of prognosis in patients with PCa and play an important role in clinical treatment (6). PCa risk classification criteria are generally based on clinical stage, GS, and pretreatment PSA levels. A detailed risk classification has been published by D'Amico et al. (7) low-risk group (PSA ≤10 ng/mL and GS ≤6 and T1-T2a), intermediate-risk group (PSA 10-20 ng/mL or GS 7 or T2b), and high-risk group (PSA >20 ng/mL or GS ≥8 or ≥T2c). With the widespread use of ^{68}Ga-PSMA PET/CT, studies have shown that increased PSMA expression is correlated with GS and the development of metastatic disease (8,9). The maximum standardized uptake value (SUV_{max}) is the most commonly used semi-quantitative parameter in PET/CT to assess tumor burden. However, SUV_{max} is not the only volumetric parameter obtainable in ^{68}Ga-PSMA PET/CT. PSMA-derived tumor volume (PSMA-TV) and total lesion PSMA (TL-PSMA) can also be calculated. There are clinical studies stating that ^{68}Ga-PSMA PET/CT results are highly predictive of treatment response (10,11). Volumetric analysis of ^{68}Ga-PSMA PET/CT in newly diagnosed PCa patients can provide comprehensive insights into tumor characteristics, aid in treatment planning, and predict clinical outcomes. This information is invaluable for personalizing patient care and improving prognostic accuracy (12,13).

In this study, we aimed to measure primary lesion SUV_{max}, PSMA-TV, and TL-PSMA; and to evaluate the relationships among volumetric parameters, GS, PSA levels, histopathological data, and metastases status in newly diagnosed PCa patients. Another endpoint of our study was the evaluation of the possible predictive role of volumetric ^{68}Ga-PSMA PET/CT parameters for clinical, radiological, or biochemical progression.

Materials and Methods

We retrospectively evaluated 78 patients with PCa who underwent ^{68}Ga-PSMA PET/CT for staging. All patients had a diagnosis of prostate adenocarcinoma by 10-12 core transrectal ultrasonography (TRUS)-guided prostate biopsy (bx) before imaging. All patients had PSA levels measured at most 3 weeks before the ^{68}Ga-PSMA PET/CT scan. Patients with missing laboratory or pathological data, treated for PCa, and in whom the primary tumor was indistinguishable from the surrounding prostate tissue were not included. This study protocol was reviewed and approved by the Manisa Celal Bayar University Health Sciences Ethics Committee (decision no: 20.478.486/506, date: 19.08.2020). Informed consent was obtained from all subjects when they were enrolled.

Preparation of the PSMA-targeting Ligand

^{68}Ga-PSMA I&T was synthesized by a fully automated, good manufacturing practice-a compliant procedure using a good radiopharmaceutical practice module (ITG iQS-TS)

connected to a 68Ge/68Ga generator (1.11-GBq, ITM) and equipped with a disposable single-use cassette kit. A standardized labeling sequence with 25 µg of unlabeled PSMA I&T was used. The synthesis of the ^{68}Ga peptides was performed using a cationic purification method with 25 µg of peptide used for the reaction. The labeling efficiency and radiochemical purity (≥95%) were determined using radio-high-performance liquid chromatography.

Image Acquisition and Reconstruction

Patient preparation, acquisition protocols, and reconstruction parameters were standardized for all patients. Sixty minutes after the intravenous injection of 2.2-2.5 MBq/kg ^{68}Ga-PSMA, the patients were scanned from the vertex to the proximal thigh, and low-dose CT (120 kVp and 80 mAs) and PET [Philips TrueFlight Select model, lutetium yttrium orthosilicate crystals; 3-dimensional acquisition; 180 s per bed position (s/bp); 5-6 bed positions] images were obtained. CT was obtained for attenuation correction. The ordered subset expectation maximization reconstruction algorithm was used with reconstruction parameters of three iterations and 33 subsets.

Image Analysis

Images were evaluated by two experienced nuclear medicine physicians blinded to the pathological and laboratory results. Any disagreement was resolved by consensus. Focal or diffuse ^{68}Ga-PSMA uptake in the prostate gland was identified as the primary lesion. Lesions with a ^{68}Ga-PSMA uptake higher than that in the blood pool and discordant with the physiological distribution were considered metastases. Regional lymph node (RLN), extra-regional lymph node (ERLN), bone, and visceral organ metastases were determined. Using a three-dimensional segmentation method, an isodontous volume of interest was created around the prostate gland, avoiding bladder activity, to calculate the volumetric parameters (Figure 1). Primary tumor TL-PSMA was calculated by multiplying PSMA-TV by the mean standardized uptake value (SUV_{mean}).

Statistical Analysis

The data obtained were entered into SPSS version 23.0 (IBM, Türkiye), and a p-value of 0.05 was considered statistically significant. Quantitative variables were described using means, standard deviations, and ranges. Mean comparisons between the groups were performed using one-way ANOVA for the quantitative variable. The relationships between the D'Amico risk groups and metastatic status were analyzed using the chi-square test. Correlations between different parameters were analyzed using the Pearson correlation test. Receiver operating characteristic (ROC) analysis was used to determine the cut-off values of SUV_{max}, PSMA-TV, and TL-PSMA for metastatic and non-metastatic patients. Possible predictive factors for clinical and biochemical recurrence were evaluated using logistic regression analysis.

Results

Patients were classified according to the D'Amico risk stratification system. The majority of patients (n=51) (65.4%) in our study were in the high-risk group. Nineteen patients (24.3%) were in the intermediate-risk group and eight patients (10.3%) were in the low-risk group. ^{68}Ga-PSMA PET/CT and PSA tests were performed within 3 weeks. The mean PSA level was 45.2 ng/mL. Descriptive characteristics are presented in Table 1. We observed

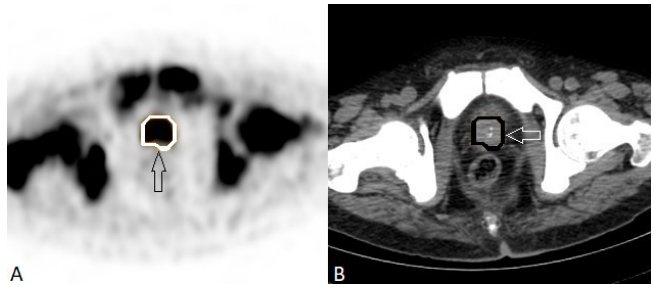

Figure 1. ^{68}Ga-PSMA PET/CT axial PET (A) and axial CT (B) images. A volume of interest was drawn around the prostate lesion (arrow)
^{68}Ga-PSMA: ^{68}Ga-prostate-specific membrane antigen, PET/CT: Positron emission tomography/computed tomography

Table 1. Distribution of descriptive characteristics

Parameter	Value
Patients (n)	78
Age	
Mean ± SD	68.5±7.3 years
Range	49-87 years
PSA	
Range	3.3-277 ng/mL
Gleason score (GS)	
GS6	10 (12.8%)
GS7	26 (33.3%)
GS8	12 (15.4%)
GS9	23 (29.5%)
GS10	7 (9%)
D'Amico risk stratification	
High-risk	51 (65.4%)
Intermediate-risk	19 (24.3%)
Low-risk	8 (10.3%)

SD: Standard deviation, PSA: Prostate-specific antigen

significant relationships between GS, SUV_{max}, and PSA levels ($p<0.05$). Of the patients included in the study, 29 (37.2%) had bone metastases (BM), and most of the ^{68}Ga-PSMA uptake observed in the bones was sclerotic on CT (Figure 2). However, pathological ^{68}Ga-PSMA accumulations that could not be detected on CT were also observed. These patients were considered highly suspicious of metastases. Magnetic resonance imaging (MRI) correlation was performed for these patients, and bone marrow infiltration on MRI was considered positive for BM. Visceral organ involvement was detected only in the lungs and was observed in 7 (9.0%) patients. Five of these seven patients had concomitant BM. When patients with and without BM were compared, differences were significant between the two groups in terms of PSA, SUV_{max}, and SUV_{mean} ($p=0.000$, $p=0.008$, and $p=0.003$, respectively). When patients with and without lung metastases (LM) were compared, a significant difference was detected only in PSA values ($p=0.002$). However, no statistically significant difference was detected between LM and SUV_{max}. We believe that this result is due to the small number of patients with LM in our study group. Isolated RLN metastases were observed in 42 of 78 (53.8%) patients. ERLN metastases were observed in 23 (29.5%) patients, and all were accompanied by RLN metastases. When the presence of ERLN and RLN metastases were compared with the SUV_{max} of the primary lesion, significant relationships were found ($p<0.05$). The mean PSA value was significantly higher in patients with RLN metastases (63.6±66.6) compared to those without lymph node metastases (23.65±32.3, $p=0.002$), and similarly, patients with ERLN metastases showed a significantly higher mean PSA value (82.9±69.2) than those without ERLN metastases (29.37±42.5, $p<0.05$). When the relationships between GS and the presence of lymph node, bone, and visceral organ metastases were examined, the sum of GS was statistically significantly increased in patients with positive metastases ($p<0.05$). We also analyzed the risk groups of patients with metastases and observed that the majority were in the high-risk group, which was an expected finding. This analysis revealed statistically significant differences between the presence of pelvic, extrapelvic, and BM and risk groups ($p=0.001$, $p=0.001$, $p=0.002$, respectively). Primary lesion PSMA-TV and TL-PSMA were compared with PSA, LM, BM, GS, and lymph node metastases. Significant relationships were observed when the PSA and GS levels of the patients were compared with PSMA-TV and TL-PSMA ($p<0.05$). When PSMA-TV and TL-PSMA were compared with the presence of bone, lung, and ERLN metastases, the relationships were not statistically significant ($p\geq0.05$). Considering the metastatic status, a significant relationship was found between the parameters defined only with RLN metastases ($p<0.05$). The mean values of PSA, SUV_{max}, and SUV_{mean} according to metastasis status are summarized in Table 2. Statistical comparisons were made according to the histopathological data such as extraprostatic extension (EPE), lymphovascular invasion (LVI), and perineural invasion (PNI) reported in the TRUS-bx results. When PSA level, SUV_{max}, SUV_{mean}, PSMA-TV, and TL-PSMA were compared with histopathological data, significant relationships were observed between all except PNI and TL-PSMA (Table 3). The SUV_{max}, PSMA-TV, and TL-PSMA cut-off values of 37 metastatic (ERLN, bone, or LM) patients were determined by ROC analysis. Area under the curve (AUC) was significant at 0.770 [95% confidence interval (CI): 0.66-0.87, $p\leq0.001$], and the SUV_{max} cut-off value was 10.85, yielding a sensitivity of 83.8% and a specificity of 63.4%. Furthermore, ROC analysis was performed for PSMA-TV and TL-PSMA, and statistically significant results were found (PSMA-TV cut-off: 33.05, AUC=0.796, 95% CI: 0.69-0.89, $p\leq0.001$, sensitivity 73%, specificity 75.6%) (TL-PSMA cut-off: 136.65, AUC=0.820, 95% CI: 0.72-0.91, $p\leq0.001$, sensitivity 75.7%, specificity 75.6%). In addition, we calculated correlation coefficients (r) for the variables we controlled. According to Table 4, the most correlated variables are observed as such; RLN-LVI (r: 0.658; $p<0.01$), ERLN-LVI (r: 0.566; $p<0.01$), and SUV_{max}-LVI (r: 0.543; $p<0.01$). The median follow-up time after ^{68}Ga-PSMA PET/CT was 45 months (interquartile range 34-52 months). The treatments that the patients received after staging are detailed in Table 5. There was no clinical, radiological, or biochemical evidence of progression in 46

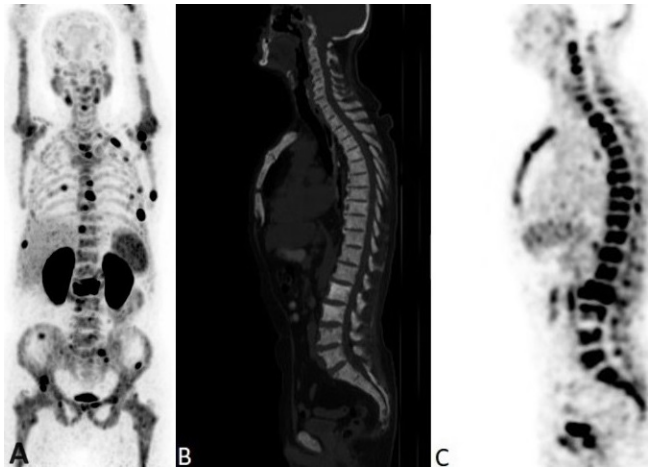

Figure 2. ^{68}Ga-PSMA PET/CT with maximum-intensity projection (A), sagittal CT (B), and sagittal PET (C) images of a 75-year-old patient with PCa (GS 5+5) with a PSA level of 64.0 ng/mL. ^{68}Ga-PSMA PET/CT images showed multiple sclerotic bone metastases

^{68}Ga-PSMA: ^{68}Ga-prostate-specific membrane antigen, PET/CT: Positron emission tomography/computed tomography, PCa: Prostate cancer, PSA: Prostate-specific antigen

Table 2. Mean values of PSA, SUV_{max}, and SUV_{mean} according to metastasis status

	Non-metastatic	Regional lymph node metastases	Extra-regional lymph node metastases	Lung metastases	Bone metastases	Total
PSA (mean ± SD)	19.3±31.8	63.6±66.6	82.9±69.3	101.9±93.4	77.2±72.8	45.2±56.9
SUV_{max} (mean ± SD)	11.3±7.4	28.2±19.5	32.3±17.9	21.6±16.2	27.2±20.5	20.5±17.2
SUV_{mean} (mean ± SD)	4.3±1.5	8.4±4.9	9.5±4.4	7.9±4.3	8.4±5.3	6.6±4.2
N (number)	29	42	23	7	29	78

PSA: Prostate-specific antigen, SUV_{max}: Maximum standardized uptake value, SUV_{mean}: Mean standardized uptake value

Table 3. Statistical results for PSA, SUV_{max}, SUV_{mean}, PSMA-TV, TL-PSMA, and histopathological features

	PSA	SUV_{max}	SUV_{mean}	PSMA-TV	TL-PSMA
EPE	p=0.003	p=0.000	p=0.000	p=0.005	p=0.028
LVI	p=0.000	p=0.000	p=0.000	p=0.004	p=0.021
PNI	p=0.002	p=0.000	p=0.000	p=0.018	**p=0.076***

PSA: Prostate-specific antigen, PSMA-TV: PSMA-derived tumor volume, TL-PSMA: Total lesion PSMA, EPE: Extraprostatic extension, LVI: Lymphovascular invasion, PNI: Perineural invasion
*p≥0.05

Table 4. Correlation coefficients of the study variables

Variables	PSA	SUV_{max}	PSMA-TV	TL-PSMA	RLN	ERLN	EPE	LVI	PNI
1. PSA	-	0.387 (0.00**)	0.408 (0.00**)	0.344 (0.00**)	0.352 (0.00**)	0.431 (0.00**)	0.393 (0.00**)	0.452 (0.00**)	0.345 (0.00**)
2. SUV_{max}	-	-	0.700 (0.00**)	0.630 (0.00**)	0.487 (0.00**)	0.448 (0.00**)	0.497 (0.00**)	0.543 (0.00**)	0.420 (0.00**)
3. PSMA-TV	-	-	-	0.962 (0.00**)	0.292 (0.01**)	0.192 (0.09)	0.322 (0.00**)	0.330 (0.00**)	0.271 (0.02*)
4. TL-PSMA	-	-	-	-	0.222 (0.05)	0.097 (0.39)	0.251 (0.03*)	0.264 (0.02*)	0.206 (0.07)
5. RLN	-	-	-	-	-	0.599 (0.00**)	0.525 (0.00**)	0.658 (0.00**)	0.404 (0.00**)
6. ERLN	-	-	-	-	-	-	0.434 (0.00**)	0.566 (0.00**)	0.440 (0.00**)
7. EPE	-	-	-	-	-	-	-	0.403 (0.00**)	0.303 (0.00**)
8. LVI	-	-	-	-	-	-	-	-	0.439 (0.00**)
9. PNI	-	-	-	-	-	-	-	-	-

*Denotes p<0.05 and **denotes p<0.01 significance levels. PSA: Prostate-specific antigen, SUV_{max}: Maximum standardized uptake value, PSMA-TV: PSMA-derived tumor volume, TL-PSMA: Total lesion PSMA, RLN: Regional lymph node, ERLN: Extra-regional lymph node, EPE: Extraprostatic extension, LVI: Lymphovascular invasion, PNI: Perineural invasion

Table 5. Initial treatments of the study group	
Initial management	**Number of patients**
RP (+/- lymph node dissection)	6
ADT + EBRT	20
EBRT	6
RP (+/- lymph node dissection) + EBRT	11
ADT	17
RP (+/- lymph node dissection) + EBRT + ADT	5
RP (+/- lymph node dissection) + ADT	8
ADT + chemotherapy	5

RP: Radical prostatectomy, EBRT: External beam radiotherapy, ADT: Androgen deprivation therapy

(59%) participants. Thirty-two (41%) patients progressed despite treatment, and four of these died during follow-up. Lesion SUV_{max}, PSMA-TV, TL-PSMA, and histopathological parameters were evaluated as predictive factors for progression. According to the logistic regression analysis results, PSMA-TV was determined to be a significant predictive factor for clinical, radiological, or biochemical progression ($p<0.05$). When histopathological parameters were evaluated, the coexistence of positive PNI and EPE was statistically predictive of progression.

Discussion

Numerous studies have highlighted the critical role of ^{68}Ga-PSMA PET/CT in restaging patients with biochemical recurrence. However, accurate initial staging is critical to improve prognosis and treatment strategies. Studies indicate that ^{68}Ga-PSMA PET/CT is superior to conventional imaging modalities in initial staging and altering the disease stage (14-17). The consensus from these investigations suggests adopting PSMA-PET as the primary modality for initially staging intermediate-high-risk PCa (18).

GS, PSA levels, and ^{68}Ga-PSMA PET/CT parameters are used to determine the risk status of newly diagnosed PCa patients (19). The combined evaluation of clinical and ^{68}Ga-PSMA PET/CT-derived parameters during initial staging would be more valuable in predicting risk status. Despite TRUS-bx being the standard method for obtaining pre-treatment GS, it potentially underestimates the true GS because of sample under-representation. However, our findings indicate a significant relationship between GS, PSA levels, and prostate lesion SUV_{max}. We also found significant relationships between the presence of lymph node metastases and SUV_{max} and PSA levels. In addition, SUV_{max} and PSA levels were significantly higher in patients with BM than in those without metastases. We also investigated the association between GS and the presence of lymph node, bone, and visceral organ metastases. The sum of GS was significantly increased in patients with metastases ($p<0.05$). Researchers assessed the correlations between SUV_{max}, GS, and PSA levels in newly diagnosed PCa patients, and similar to our results, they revealed significant relationships between PSA values, SUV_{max}, and GS (6,20). Uprimny et al. (6) also found that the PSA level and prostate lesion SUV_{max} of patients with lymph node metastases were statistically higher than those without lymph node metastases; however, they stated that, unlike the PSA level, SUV_{max} and the presence of BM were not statistically related. We believe that this is primarily due to the small number of patients with BM in their study.

PET/CT volumetric parameters have gained importance in predicting the prognosis and response to treatment in oncological patients in recent years. Investigations have shown that PSMA-TV and TL-PSMA demonstrated significant correlations with GS and PSA levels. They considered that PSMA-derived volumetric parameters could be better quantitative imaging biomarkers for whole-body tumor burden (12,13). In our study, we investigated volumetric measurements of primary prostate lesions regardless of metastatic status and found significant relationships between SUV_{max}, PSMA-TV, and TL-PSMA with PSA and GS. Karyagar et al. (21) found that metastatic patients had significantly higher primary prostate lesion PSMA-TV and TL-PSMA than the non-metastatic group. In our study, we categorized the metastatic status as RLN metastases, ERLN metastases, LM, and BM. We observed significant associations between prostate lesion SUV_{max} and all metastatic conditions, except LM. In addition, PSMA-TV and TL-PSMA of prostate lesions were statistically higher in patients with RLN metastases than in those without ($p<0.05$). The cut-off SUV_{max} value for prostate lesions in terms of the metastatic or high-risk patient group has also been the subject of investigations. Two studies investigating SUV_{max} cut-off values for high-risk patients identified these as 9.1 and 10.55, respectively (8,22). In our study, in 37 metastatic patients, ROC curve analysis was performed to identify the cut-off values for SUV_{max}, PSMA-TV, and TL-PSMA, which were determined to be 10.85, 33.05, and 136.65, respectively. Additionally, we compared the volumetric parameters and clinical data of the patients with pathological features (EPE, LVI, and PNI) in the TRUS-bx results. PSA, SUV_{max}, PSMA-TV, and TL-PSMA were compared with histopathological data, and significant correlations were observed between all except PNI and TL-PSMA. PNI and TL-PSMA discordance are not clinically relevant or important to consider as our main findings. Based on the correlation coefficients, the high

correlation between SUV_{max} and LVI stands out as one of the meaningful and valuable outcomes of our study.

Clinicians face the challenge of delaying PCa progression while avoiding overtreatment. Therefore, the predictive value of volumetric parameters in newly diagnosed PCa is of great interest. While existing studies predominantly focus on whole-body volumetric parameters, our research investigates whether primary prostate lesion volumetric parameters can predict treatment response. Retrospective analyses suggest ^{68}Ga-PSMA PET/CT as a valuable tool for assessing therapy response in metastatic PCa, highlighting changes in quantitative volumetric tumor parameters, particularly PSMA-TV, as potential predictive and prognostic indicators for overall survival, thereby aiding in personalized treatment approaches (23-25). The patients included in our study were followed up with different treatment protocols. As a result of the analysis on whether volumetric parameters (SUV_{max}, PSMA-TV, TL-PSMA) obtained from pretreatment ^{68}Ga-PSMA PET/CT can predict progression, we concluded that only PSMA-TV has a place in predicting progression. Similarly, Karyağar et al. (26) conducted a study to ascertain whether pretreatment ^{68}Ga-PSMA PET/CT parameters could serve as indicators for predicting PSA response in metastatic castration-resistant prostate cancer patients undergoing enzalutamide treatment. Their findings indicated that PSMA-TV values are predictive of PSA response. In addition to volumetric parameters, we evaluated whether any of the histopathological parameters detected at biopsy (EPE, LVI, and PNI) played a role in predicting treatment failure. We concluded that none of these parameters alone had a predictive value, but the coexistence of positive PNI and EPE was predictive of progression. In other words, the simultaneous presence of these two conditions (PNI and EPE) was considered a strong predictor of treatment failure. Studies have been conducted on the predictive roles of histopathologic features in PCa treatment success and prognosis. In these studies, EPE has been acknowledged as a negative prognostic indicator that impacts both cancer progression and patient survival (27). However, research on the prognostic value of PNI has yielded conflicting results. PNI is a commonly observed pathway for tumor spread and is significant in the clinical management of PCa. PNI refers to the process by which cancer cells spread along nerve pathways. This method of tumor dissemination is frequently observed in patients with PCa and holds significant importance in its clinical management. Several studies have suggested that the presence of PNI should not automatically lead to more aggressive treatment strategies, but it could be an indicator of a higher risk of progression (28). Some researchers have mentioned that PNI is a predictive factor for disease progression, whereas others have emphasized that it plays no such role (27). The studies mentioned that the prognostic value of PNI is more important in biopsy specimens as it could affect treatment management decisions and surgical techniques. Moreira et al. (29) found that PNI in biopsies was associated with an increased risk of progression. However, Lee et al. (30) reported that PNI in a prostatectomy specimen was significantly related to biologically aggressive tumor patterns but was not a prognostic factor for PSA recurrence or cancer-specific survival in patients with PCa.

Study Limitations

Our study has several limitations. First, the pathologic data were exclusively derived from TRUS-bx, which may limit the generalizability of our findings. Second, the retrospective nature of our analysis. Third, the study was conducted in a single center with a relatively small patient cohort. To overcome these limitations and enhance the robustness of our conclusions, future research should conduct prospective, multicenter studies involving larger patient populations in this field.

Conclusion

PCa is the second most common cancer in men globally, making research in this field crucial. All clinical, histopathological, and imaging-based parameters and their relations with each other should be clarified, and the effect of these parameters on the course of the disease should be well known. Because of its high diagnostic accuracy and superiority over conventional imaging methods, ^{68}Ga-PSMA PET/CT has become a milestone in the diagnosis and follow-up of PCa. Our research specifically targets the volumetric parameters of primary prostate lesions, thus addressing a gap in the existing literature. The relationships emphasized in our study underscore the potential of these parameters to synergistically contribute to a more comprehensive understanding of disease severity and progression. In conclusion, this retrospective analysis showed that ^{68}Ga-PSMA PET/CT retains its place as an invaluable imaging modality that should be considered first in PCa staging because of its superior compatibility with clinical and histopathological data. Our results indicate that the PSMA-TV value of a primary prostate lesion can predict treatment failure. This information is valuable for personalizing patient treatment, improving prognostic accuracy, and predicting clinical outcomes; therefore, we anticipate that ^{68}Ga-PSMA PET/CT will become a risk stratification tool in the management of this disease.

Ethics

Ethics Committee Approval: This study protocol was reviewed and approved by the Manisa Celal Bayar University Health Sciences Ethics Committee (decision no: 20.478.486/506, date: 19.08.2020). Informed consent was obtained from all subjects when they were enrolled.

Informed Consent: Written informed consent was obtained from all patients.

Authorship Contributions

Surgical and Medical Practices: G.M., C.S.A., Concept: G.M., Y.P., C.S.A., Design: G.M., E.S., Data Collection or Processing: G.M., Y.P., C.S.A., G.G., Analysis or Interpretation: G.M., Y.P., E.S., Literature Search: G.M., G.G., Writing: G.M., E.S.

Conflict of Interest: No conflict of interest was declared by the authors.

Financial Disclosure: The authors declared that this study has received no financial support.

References

1. Bray F, Ferlay J, Soerjomataram I, Siegel RL, Torre LA, Jemal A. Global cancer statistics 2018: GLOBOCAN estimates of incidence and mortality worldwide for 36 cancers in 185 countries. CA Cancer J Clin 2018;68:394-424.
2. Siegel RL, Miller KD, Jemal A. Cancer statistics, 2020. CA Cancer J Clin 2020;70:7-30.
3. Maurer T, Eiber M, Schwaiger M, Gschwend JE. Current use of PSMA-PET in prostate cancer management. Nat Rev Urol 2016;13:226-235.
4. Morigi JJ, Stricker PD, van Leeuwen PJ, Tang R, Ho B, Nguyen Q, Hruby G, Fogarty G, Jagavkar R, Kneebone A, Hickey A, Fanti S, Tarlinton L, Emmett L. Prospective Comparison of 18F-Fluoromethylcholine Versus 68Ga-PSMA PET/CT in Prostate Cancer Patients Who Have Rising PSA After Curative Treatment and Are Being Considered for Targeted Therapy. J Nucl Med 2015;56:1185-1190.
5. Franklin A, Yaxley WJ, Raveenthiran S, Coughlin G, Gianduzzo T, Kua B, McEwan L, Wong D, Delahunt B, Egevad L, Samaratunga H, Brown N, Parkinson R, Roberts MJ, Yaxley JW. Histological comparison between predictive value of preoperative 3-T multiparametric MRI and 68 Ga-PSMA PET/CT scan for pathological outcomes at radical prostatectomy and pelvic lymph node dissection for prostate cancer BJU Int 2021;127:71-79.
6. Uprimny C, Kroiss AS, Decristoforo C, Fritz J, von Guggenberg E, Kendler D, Scarpa L, di Santo G, Roig LG, Maffey-Steffan J, Horninger W, Virgolini IJ. 68Ga-PSMA-11 PET/CT in primary staging of prostate cancer: PSA and Gleason score predict the intensity of tracer accumulation in the primary tumour. Eur J Nucl Med Mol Imaging 2017;44:941-949.
7. D'Amico AV, Whittington R, Malkowicz SB, Schultz D, Blank K, Broderick GA, Tomaszewski JE, Renshaw AA, Kaplan I, Beard CJ, Wein A. Biochemical outcome after radical prostatectomy, external beam radiation therapy, or interstitial radiation therapy for clinically localized prostate cancer. JAMA 1998;280:969-974.
8. Demirci E, Kabasakal L, Şahin OE, Akgün E, Gültekin MH, Doğanca T, Tuna MB, Öbek C, Kiliç M, Esen T, Kural AR. Can SUVmax values of Ga-68-PSMA PET/CT scan predict the clinically significant prostate cancer? Nucl Med Commun 2019;40:86-91.
9. Wang H, Amiel T, Würnschimmel C, Langbein T, Steiger K, Rauscher I, Horn T, Maurer T, Weber W, Wester HJ, Knorr K, Eiber M. PSMA-ligand uptake can serve as a novel biomarker in primary prostate cancer to predict outcome after radical prostatectomy. EJNMMI Res 2021;11:76.
10. Ong S, Pascoe C, Kelly BD, Ballok Z, Webb D, Bolton D, Murphy D, Sengupta S, Bowden P, Lawrentschuk N. PSMA PET-CT Imaging Predicts Treatment Progression in Men with Biochemically Recurrent Prostate Cancer-A Prospective Study of Men with 3 Year Follow Up. Cancers (Basel) 2022;14:2717.
11. Emmett L, Tang R, Nandurkar R, Hruby G, Roach P, Watts JA, Cusick T, Kneebone A, Ho B, Chan L, van Leeuwen PJ, Scheltema MJ, Nguyen A, Yin C, Scott A, Tang C, McCarthy M, Fullard K, Roberts M, Francis R, Stricker P. 3-Year Freedom from Progression After 68Ga-PSMA PET/CT-Triaged Management in Men with Biochemical Recurrence After Radical Prostatectomy: Results of a Prospective Multicenter Trial. J Nucl Med 2020;61:866-872.
12. Schmuck S, von Klot CA, Henkenberens C, Sohns JM, Christiansen H, Wester HJ, Ross TL, Bengel FM, Derlin T. Initial Experience with Volumetric 68Ga-PSMA I&T PET/CT for Assessment of Whole-Body Tumor Burden as a Quantitative Imaging Biomarker in Patients with Prostate Cancer. J Nucl Med 2017;58:1962-1968.
13. Schmidkonz C, Cordes M, Goetz TI, Prante O, Kuwert T, Ritt P, Uder M, Wullich B, Goebell P, Bäuerle T. 68Ga-PSMA-11 PET/CT derived quantitative volumetric tumor parameters for classification and evaluation of therapeutic response of bone metastases in prostate cancer patients. Ann Nucl Med 2019;33:766-775.
14. Wong HS, Leung J, Bartholomeusz D, Sutherland P, Le H, Nottage M, Iankov I, Chang JH. Comparative study between 68 Ga-prostate-specific membrane antigen positron emission tomography and conventional imaging in the initial staging of prostate cancer. J Med Imaging Radiat Oncol 2018;62:816-822.
15. Spohn S, Jaegle C, Fassbender TF, Sprave T, Gkika E, Nicolay NH, Bock M, Ruf J, Benndorf M, Gratzke C, Grosu AL, Zamboglou C. Intraindividual comparison between 68Ga-PSMA-PET/CT and mpMRI for intraprostatic tumor delineation in patients with primary prostate cancer: a retrospective analysis in 101 patients. Eur J Nucl Med Mol Imaging 2020;47:2796-2803.
16. Tulsyan S, Das CJ, Tripathi M, Seth A, Kumar R, Bal C. Comparison of 68Ga-PSMA PET/CT and multiparametric MRI for staging of high-risk prostate cancer68Ga-PSMA PET and MRI in prostate cancer. Nucl Med Commun 2017;38:1094-1102.
17. Sonni I, Felker ER, Lenis AT, Sisk AE, Bahri S, Allen-Auerbach M, Armstrong WR, Suvannarerg V, Tubtawee T, Grogan T, Elashoff D, Eiber M, Raman SS, Czernin J, Reiter RE, Calais J. Head-to-Head Comparison of ^{68}Ga-PSMA-11 PET/CT and mpMRI with a Histopathology Gold Standard in the Detection, Intraprostatic Localization, and Determination of Local Extension of Primary Prostate Cancer: Results from a Prospective Single-Center Imaging Trial. J Nucl Med 2022;63:847-854.
18. Chow KM, So WZ, Lee HJ, Lee A, Yap DWT, Takwoingi Y, Tay KJ, Tuan J, Thang SP, Lam W, Yuen J, Lawrentschuk N, Hofman MS, Murphy DG, Chen K. Head-to-head Comparison of the Diagnostic Accuracy of Prostate-specific Membrane Antigen Positron Emission Tomography and Conventional Imaging Modalities for Initial Staging of Intermediate- to High-risk Prostate Cancer: A Systematic Review and Meta-analysis. Eur Urol 2023;84:36-48.
19. Liu C, Liu T, Zhang N, Liu Y, Li N, Du P, Yang Y, Liu M, Gong K, Yang X, Zhu H, Yan K, Yang Z. 68Ga-PSMA-617 PET/CT: a promising new technique for predicting risk stratification and metastatic risk of prostate cancer patients. Eur J Nucl Med Mol Imaging 2018;45:1852-1861.
20. Koerber SA, Utzinger MT, Kratochwil C, Kesch C, Haefner MF, Katayama S, Mier W, Iagaru AH, Herfarth K, Haberkorn U, Debus J, Giesel FL. 68Ga-PSMA-11 PET/CT in Newly Diagnosed Carcinoma of the Prostate:

Correlation of Intraprostatic PSMA Uptake with Several Clinical Parameters. J Nucl Med 2017;58:1943-1948.

21. Karyagar SS, Karyagar S, Guven O. Correlations of the 68Ga-PSMA PET/CT derived primary prostate tumor PSMA expression parameters and metastatic patterns in patients with Gleason Score >7 prostate cancer. Hell J Nucl Med 2020;23:120-124.
22. Erdoğan M, Özkan EE, Öztürk SA, Yıldız M, Şengül SS. The Role of Ga-68 PSMA PET/CT Scan on Differentiating of Oligometastatic and High Risk Prostate Cancer. Mol Imaging Radionucl Ther 2020;29:98-104.
23. Shagera QA, Artigas C, Karfis I, Critchi G, Chanza NM, Sideris S, Peltier A, Paesmans M, Gil T, Flamen P. 68Ga-PSMA PET/CT for Response Assessment and Outcome Prediction in Metastatic Prostate Cancer Patients Treated with Taxane-Based Chemotherapy. J Nucl Med 2022;63:1191-1198.
24. Oruç Z, Güzel Y, Ebinç S, Kömek H, Küçüköner M, Kaplan MA, Oruç İ, Urakçi Z, Işikdoğan A. Efficacy of 68Ga-PSMA PET/CT-derived whole-body volumetric parameters in predicting response to second-generation androgen receptor axis-targeted therapy, and the prognosis in metastatic hormone-refractory prostate cancer patients. Nucl Med Commun 2021;42:1336-1346.
25. Can C, Gündoğan C, Yildirim OA, Poyraz K, Güzel Y, Kömek H. Role of 68Ga-PSMA PET/CT parameters in treatment evaluation and survival prediction in prostate cancer patients compared with biochemical response assessment. Hell J Nucl Med 2021;24:25-35.
26. Karyağar S, Güven O, Karyağar SS, Arici S, Selvi O, Geredeli Ç, Özülker F. Can 68Ga-PSMA PET/CT-derived prostate-specific membrane antigen expression parameters predict prostate-specific antigen response to enzalutamide treatment? Nucl Med Commun 2021;42:1011-1016.
27. Egevad L, Delahunt B, Kristiansen G, Samaratunga H, Varma M. Contemporary prognostic indicators for prostate cancer incorporating International Society of Urological Pathology recommendations. Pathology 2018;50:60-73.
28. Niu Y, Förster S, Muders M. The Role of Perineural Invasion in Prostate Cancer and Its Prognostic Significance. Cancers (Basel) 2022;14:4065.
29. Moreira DM, Fleshner NE, Freedland SJ. Baseline Perineural Invasion is Associated with Shorter Time to Progression in Men with Prostate Cancer Undergoing Active Surveillance: Results from the REDEEM Study. J Urol 2015;194:1258-1263.
30. Lee JT, Lee S, Yun CJ, Jeon BJ, Kim JM, Ha HK, Lee W, Chung MK. Prediction of perineural invasion and its prognostic value in patients with prostate cancer. Korean J Urol 2010;51:745-751.

Original Article

Mol Imaging Radionucl Ther 2024;33:77-89 *DOI:10.4274/mirt.galenos.2024.99705*

Diagnostic Performance of FAPI PET/CT vs. ^{18}F-FDG PET/CT in Evaluation of Liver Tumors: A Systematic Review and Meta-analysis

Karaciğer Tümörlerinin Değerlendirilmesinde FAPI PET/BT ve ^{18}F-FDG PET/BT'nin Tanısal Performanslarının Karşılaştırılması: Sistematik Bir Derleme ve Meta-analiz

Parneet Singh, Tejasvini Singhal, Girish Kumar Parida, Ashique Rahman, Kanhaiyalal Agrawal

All India Institute of Medical Sciences, Department of Nuclear Medicine, Bhubaneswar, India

Abstract

Objectives: Primary liver tumors constitute one of the most common tumors. These are aggressive tumors with poor survival. Fluorodeoxyglucose (FDG) positron emission tomography/computed tomography (PET/CT), most commonly used functional imaging, shows limited tracer retention and poor tumor to background ratios (TBR). Novel ^{68}Ga-fibroblast-activation-protein inhibitor (FAPI) PET/CT has shown better tracer uptake and detection efficacy in liver tumors. However, most of the available literature is limited to single center studies with limited number of patients. So, we tried to review and analyze the head-to-head comparison of ^{18}F-FDG PET/CT and ^{68}Ga-FAPI PET/CT in evaluation of liver tumors.

Methods: Literature available on head to head comparison of diagnostic accuracy of ^{18}F-FDG PET/CT and ^{68}Ga-FAPI PET/CT was searched in databases like PubMed, SCOPUS, EMBASE and Google Scholar for published original studies till April 2023. The relevant studies were selected and assessed using the Revised Tool for the Quality Assessment of Diagnostic Accuracy Studies-2 checklist. A random-effect model was used for calculating pooled sensitivity and specificity. They were represented with 95% confidence intervals (95% CI) and demonstrated in Forest plots. I-square statistic was used to assess heterogeneity in the studies.

Results: Pooled sensitivity and specificity of FAPI PET/CT and ^{18}F-FDG PET/CT for detection of primary liver tumors was 94.3% (95% CI: 90.6-96.8%); 89.3% (95% CI: 71.8-97.7%) and 56.1% (95% CI: 49.7-62.5%); 96.4% (95% CI: 81.7-99.9%) respectively. Pooled sensitivity for detection of extrahepatic metastatic disease was 92.2% (range: 88.1-100%; 95% CI: 87.8-95.4%) and 72.4% (range: 69.8-76.5; 95% CI: 65.9-78.2%) respectively. Also, the maximum standardized uptake value (SUV_{max}) and TBR were higher for FAPI PET/CT than ^{18}F-FDG PET/CT in the included studies.

Conclusion: Overall, FAPI PET/CT showed higher sensitivity for detection of liver tumors with better SUV_{max} and TBR than ^{18}F-FDG PET/CT.

Keywords: Positron emission tomography/computed tomography, ^{18}F-fluorodeoxyglucose, fibroblast-activation-protein inhibitors, liver cancers, hepatocellular cancer, cholangiocarcinoma

Öz

Amaç: Primer karaciğer tümörleri en sık görülen tümörlerdendir. Bunlar hayatta kalma oranı düşük olan agresif tümörlerdir. En sık kullanılan fonksiyonel görüntüleme olan florodeoksiglukoz (FDG) pozitron emisyon tomografisi/bilgisayarlı tomografi (PET/BT), sınırlı radyofarmasötik tutulumu ve zayıf tümör/arka plan oranları (TBR) gösterir. Yeni ^{68}Ga-fibroblast aktivasyon protein inhibitörü (FAPI) PET/BT, karaciğer tümörlerinde daha iyi radyofarmasötik tutulumu ve tespit etkinliği göstermiştir. Ancak mevcut literatürün çoğu, sınırlı hasta sayısıyla yapılan tek merkezli çalışmalarla sınırlıdır. Bu nedenle, karaciğer tümörlerinin değerlendirilmesinde ^{18}F-FDG PET/BT ve ^{68}Ga-FAPI PET/BT'nin birebir karşılaştırmasını gözden geçirip analiz etmeye çalıştık.

Address for Correspondence: Girish Kumar Parida, Asst. Prof., All India Institute of Medical Sciences, Department of Nuclear Medicine, Bhubaneswar, India
Phone: +9968856817 **E-mail:** grissh135@gmail.com ORCID ID: orcid.org/0000-0003-2533-4608
Received: 30.08.2023 **Accepted:** 03.03.2024 **Epub:** 16.04.2024

Yöntem: ^{18}F-FDG PET/BT ve ^{68}Ga-FAPI PET/BT'nin tanısal doğruluğunun birebir karşılaştırılması konusunda mevcut literatür, Nisan 2023'e kadar yayınlanmış araştırma makaleleri için PubMed, SCOPUS, EMBASE ve Google Scholar gibi veritabanlarında tarandı. İlgili çalışmalar Tanısal Doğruluk Çalışmalarının Kalite Değerlendirmesi için Gözden Geçirilmiş Araç-2 kontrol listesi kullanılarak seçilmiş ve değerlendirilmiştir. Birleştirilmiş duyarlılığı ve özgüllüğü hesaplamak için rastgele etki modeli kullanıldı. Bunlar %95 güven aralıklarıyla (%95 GA) temsil edildi ve Orman grafiklerinde gösterildi. Çalışmalardaki heterojenliği değerlendirmek için I-kare istatistiği kullanıldı.

Bulgular: Primer karaciğer tümörlerinin tespiti için FAPI PET/BT'nin havuzlanmış duyarlılığı ve özgüllüğü sırasıyla %94,3 (%95 GA: %90,6-96,8) ve %89,3 (%95 GA: %71,8-97,7); ^{18}F-FDG PET/BT'nin havuzlanmış duyarlılığı ve özgüllüğü sırasıyla %56,1 (%95 GA: %49,7-62,5) ve %96,4 (%95 GA: %81,7-99,9) idi. Ekstrahepatik metastatik hastalığın saptanması için havuzlanmış duyarlılık FAPI PET/BT ve ^{18}F-FDG PET/BT için sırasıyla %92,2 (aralık: %88,1-100; %95 GA: %87,8-95,4) ve %72,4 (aralık: 69,8-76,5; %95 GA: %65,9-78,2) idi. Ayrıca, dahil edilen çalışmalarda FAPI PET/BT için maksimum standardize tutulum değeri (SUV_{maks}) ve TBR, ^{18}F-FDG PET/BT'den daha yüksekti.

Sonuç: Genel olarak, FAPI PET/BT, karaciğer tümörlerinin tespitinde ^{18}F-FDG PET/BT'ye göre daha iyi SUV_{maks} ve TBR ile daha yüksek duyarlılık gösterdi.

Anahtar kelimeler: Pozitron emisyon tomografisi/bilgisayarlı tomografi, ^{18}F-florodeoksiglukoz, fibroblast aktivasyon protein inhibitörleri, karaciğer kanserleri, hepatoselüler kanser, kolanjiokarsinom

Introduction

Primary liver tumor comprises of two major histological types of cancers i.e., hepatocellular carcinoma (HCC) and cholangiocarcinoma (CC). HCC arises from the hepatocytes and is the most common type, comprising of ~75% of all liver tumors. While CC arises from biliary tree with in the liver and is the second most common liver cancer (~12-15% of all liver cancer). Overall, Liver tumors are fairly common and constitutes the 6th most commonly diagnosed cancer worldwide with an incidence of 4.7%. These are aggressive with 5-year survival as low as 18%. Liver cancer is the 4th most common cause of cancer-associated mortality worldwide (1,2).

Liver tumors are usually diagnosed late, especially in countries like India where liver tumor screening is not common with only 13.6-23.7% of cases presenting at stages where curative treatment could be offered (3,4).

Imaging plays a very important role in the evaluation of liver tumors. Unlike other malignancies, liver tumors, especially HCC can be diagnosed non-invasively without biopsy without histopathological confirmation. Diagnostic imaging modalities used in the staging and workup of liver tumors include ultrasonography, contrast-enhanced computed tomography (CECT), magnetic resonance imaging (MRI), and functional/hybrid (functional + anatomical) imaging modalities like ^{18}F-fluorodeoxyglucose positron emission tomography/computed tomography (PET/CT) and recently introduced ^{68}Ga-fibroblast-activation-protein inhibitor (FAPI) PET/CT (5).

Functional imaging targets physiological functions which are hyper-represented in tumors compared to normal tissues. FDG targets glucose metabolism and enters the cell via GLUT transporters but is not metabolized like glucose and remains trapped in cells while FAPI is an inhibitor of FAP highly expressed on cancer-associated fibroblasts which constitute as high as 90% of gross tumor mass in some malignancies (6,7).

^{18}F-FDG PET/CT is the most commonly used functional imaging and has established its central role in a wide variety of malignant and non-malignant conditions. However, its role in liver tumors is limited mainly due to the presence of glucose-6-phosphatase, high expression of P-glycoprotein, lower expression of GLUT1 or GLUT2 especially in well to moderately-differentiated HCC and high background activity in the liver, thus limiting the FDG avidity of these tumors. Glucose-6-phosphatase present in high concentration in hepatocytes, can dephosphorylate glucose-6-phosphate and FDG-6-phosphate and this FDG then can exit from the cell. These reduces the tumor to background ratios (TBR) for liver tumors (8,9). Liver tumors have high amount of stromal component and desmoplastic reaction and thus, FAPI avidity. This high FAPI avidity together with the low liver background results in better TBRs and sensitivity (6). Recent literature suggests a higher sensitivity of FAPI ~87-100% compared to 65-92% for ^{18}F-FDG PET/CT (10). However, the limited literature available that compared the diagnostic performance of FDG vs. FAPI is mainly from single-center studies with a limited number of patients. Thus, we tried to meta-analyse these studies to highlight the diagnostic performance of ^{18}F-FDG PET/CT vs ^{68}Ga-FAPI PET/CT.

Materials and Methods

We did this meta-analysis by following the "Preferred Reporting Items for Systematic Reviews and Meta-Analyses" (PRISMA) statement which describes an evidence-based minimum set of items for reporting in systematic reviews and meta-analyses (9). Ethical approval has been taken from the All India Institute of Medical Sciences Bhubaneswar Ethics Committee with approval number T/IM-NF/Nucl. Med/23/19 (date: 15.05.2023). As this is a meta-analysis of the already published articles and no patient is directly involved, so taking consent is no applicable.

Literature Search Strategy

A comprehensive literature search of PubMed, SCOPUS, Embase and Google Scholar databases was carried out to find relevant published articles performing head-to-head comparison of diagnostic accuracy of ^{18}F-FDG PET/CT and ^{68}Ga-FAPI PET/CT in evaluation of hepatic tumors. We used a search string made of following keywords: (1) "^{18}F-FDG PET/CT" or "fluorodeoxyglucose PET" (2) "^{68}Ga-FAPI PET/CT" or "fibroblast activating protein inhibitor" (3) "HCC" or "hepatic tumors" or "hepatocellular carcinoma" or "cholangiocarcinoma" or "liver tumors".

The literature was searched with an upper time bracket up to 26th April 2023 with no lower time bracket or language restriction. Also, relevant references from the retrieved studies were screened for additional articles.

Selection Criteria

Studies fulfilling the following inclusion criteria were included: (a) original studies where both ^{68}Ga-FAPI PET/CT and ^{18}F-FDG PET/CT were performed in patients with hepatic tumors; (b) sufficient data to reassess sensitivity and specificity of both ^{68}Ga-FAPI PET/CT and ^{18}F-FDG PET/CT in patients with hepatic tumors; (c) appropriate reference standard was used (viz histopathological assessment and/or follow up); (d) the time interval between the ^{68}Ga-FAPI PET/CT and ^{18}F-FDG PET/CT ≤10 days.

The exclusion criteria were: a) articles not within the field of interest of this review; b) articles without head-to-head comparison of ^{68}Ga-FAPI PET/CT and ^{18}F-FDG PET/CT; c) the time interval between the ^{68}Ga-FAPI PET/CT and ^{18}F-FDG PET/CT >10 days; d) review articles, letters or editorials, comments, abstracts presented at conference; e) case reports or small case series (<5 patients), f) data overlap.

Quality Assessment and Data Extraction

The methodological quality of the selected studies was assessed by two investigators independently. Any disagreements were resolved through consultation or intervention by the third reviewer.

Quality of studies was assessed using the Quality Assessment of Diagnostic Accuracy Studies-2 (QUADAS-2) tool which primarily evaluates the risk of bias in patient selection, index test, reference standard, and the timing and flow of reference test (11).

For each study, following details were extracted: Basic details like first author, year of publication, country of origin, study design (retrospective, prospective); characteristics of study population like gender and age, sample size, and technical aspects (injected activity of ^{18}F-FDG and ^{68}Ga-FAPI, time between injections and image acquisition); reference standard, clinical results or other diagnostic methods used (CT and MRI).

For each study, we tried to extract the number of True Positive, True Negative, False Positive, and False Negative findings for ^{18}F-FDG PET/CT and ^{68}Ga-FAPI PET/CT in the staging of hepatic tumors.

Statistical Analysis

We tried to obtain the sensitivity, specificity, from individual studies on a per-patient and per-lesion based analysis. Pooled data was presented with 95% confidence intervals (95% CI) and displayed using forest plots. Heterogeneity was estimated using the I-square index (I^2). The area under the summary receiver operating characteristics curve was calculated to measure the accuracy of these methods.

Results

Literature Search

The primary electronic search of PubMed, SCOPUS, Embase and Google Scholar resulted in 175 relevant articles. Of these, 38 were duplicates. The titles of 137 articles were reviewed, out of which 112 were excluded due to following reasons: (i) not related to the topic (106); (ii) case report (3); (iii) review articles (3). Remaining 25 articles were selected, abstracts of which were reviewed by two reviewers PS and TS. Twenty-five full-text articles were selected for review. After screening the 25 full-text articles, we excluded 16 articles for the following reasons: (i) no head to head comparison was available; (ii) studies which included different types of tumors but data for liver cancer patients was not provided separately; (iii) studies included only patients with tumors negative on ^{18}F-FDG PET/CT; (iv) the time interval between the ^{68}Ga-FAPI PET/CT and ^{18}F-FDG PET/CT >10 days. Finally, 9 eligible studies were included in this review. The process of selection of studies in the meta-analysis is depicted in PRISMA flowchart (Figure 1).

Study Characteristics

The basic characteristics of the studies included in the final analysis are summarized in Table 1. A total of 9 studies were analysed, of these 7 studies were prospective while 2 were retrospective. Among the included studies, 3 studies compared the utility of FAPI PET/CT and FDG PET/CT in multiple malignancies. Chen et al. (12) included 75 patients, of which 11 were liver tumors and were included in the meta-analysis. Similarly, Pang et al. (13) included 64 patients with 15 types of malignancies, of which only 12 were liver tumors. While Lan et al. (14) evaluated 123 patients (102 oncologic and 21 non-oncologic), of which only 16 were liver tumors. The prospective pilot study for dedicated primary HCC was conducted by Shi et al. (15). This study

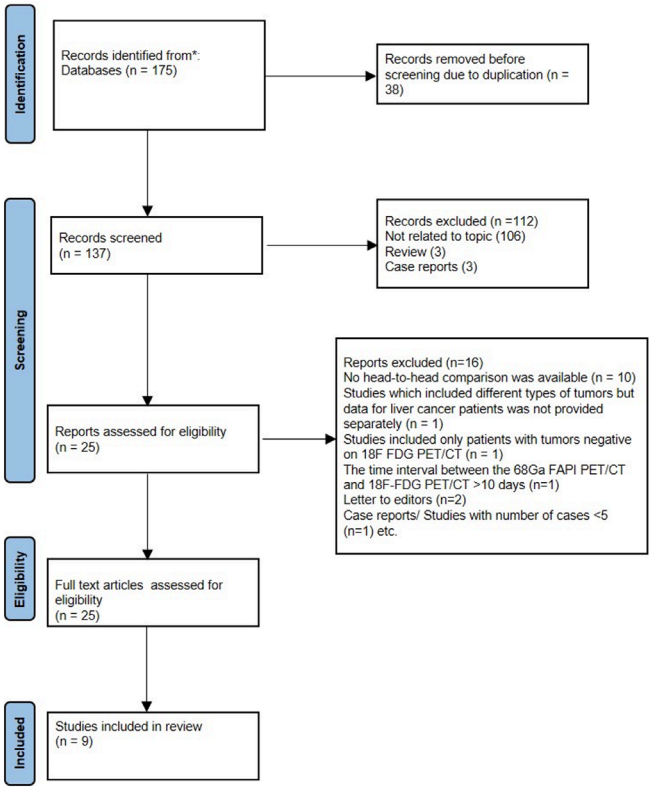

Figure 1. PRISMA flow chart depicting the search for studies on head to head comparison of ^{68}Ga-FAPI and ^{18}F-FDG PET/CT in patients of with liver tumors. Nine studies were selected for final the current meta-analysis FAPI: Fibroblast-activation-protein inhibitors, ^{18}F-FDG: Fluorine-18-fluorodeoxyglucose, PET/CT: Positron emission tomography/computed tomography, PRISMA: Preferred Reporting Items for Systematic Reviews and Meta-Analyses

included 20 patients with primary HCC. Following this, Wang et al. (16) and Siripongsatian et al. (17) evaluated the utility of FAPI PET/CT in 25 and 27 liver tumor patients, respectively. Jinghua et al. (18) evaluated 47 patients with biliary tract tumors, of which 9 were excluded from the meta-analysis (5 benign and 4 gallbladder carcinoma) and the remaining 11 were included. Rajaraman et al. (19) evaluated 41 patients with suspected liver tumors, of which 7 had a final diagnosis of non-hepatic malignancies (6 gallbladder carcinoma and 1 peri-ampullary carcinoma) and the remaining 34 were included in the meta-analysis. Similarly, in study by Guo et al. (20) including 34 patients, 2 were benign while 9 had no histological proof, thus only 23 patients were included in the meta-analysis.

All studies used ^{68}Ga-FAPI PET/CT and ^{18}F-FDG PET/CT. The technical details of the included studies are given in Table 2. All the included studies performed both qualitative (visual analysis) and semi-quantitative analysis. Semi-quantitative parameters of the included studies are given in Table 3.

Quality Assessment

The quality assessment of the included studies was performed using QUADAS-2 (11). The quality of the included studies is demonstrated in Table 4 and Figure 2, respectively.

Quantitative Analysis (Meta-analysis)

A total of 9 studies were included for the systematic review, however, complete data for quantitative analysis was not available for the included studies. The sensitivity and specificity for primary tumor detection was analysed on per-patient and per lesion basis as well as in terms of different

Table 1. Basic characteristics of the studies included in the systematic review

Authors	Year	Country	Study design	No. of patients	Imaging purpose	Blinding	Imaging analysis	Mean age (year)	Diagnostic criteria
Chen et al. (12)	2020	China	P	11	Initial staging, relapsed	yes	V+Q	Median =61.5	Histopathology
Guo et al. (20)	2021	China	P	23	Initial staging	Yes	V+Q	Mean-60.6	Histopathology
Shi et al. (15)	2021	China	P	20	Initial staging	NR	V+Q	Mean-58	Histopathology/ follow-up
Siripongsatian et al. (17)	2022	Thailand	R	27	Initial staging, relapsed	Yes	V+Q	Median =61.5	Follow-up/MRI
Wang et al. (16)	2021	China	R	25	Initial staging	Yes	V+Q	Mean-59.4	Histopathology
Pang et al. (13)	2022	China	P	12	Initial staging, relapsed	No	V+Q	Median =57.5	Histopathology/ follow up
Lan et al. (14)	2021	China	P	16	Initial staging, relapsed	Yes	V+Q	Mean-56.1	CECT/MRI/ follow up
Rajaraman et al. (19)	2023	India	P	34	Initial staging	NR	V+Q	NR	Histopathology/ MRI
Jinghua et al. (18)	2023	China	P	38	Initial staging, relapsed	Yes	V+Q	Mean-59.09	Histopathology/ follow up

FAPI: Fibroblast-activation-protein inhibitors, 18F-FDG: Fluorine-18-fluorodeoxyglucose, PET: Positron emission tomography, CT: Computed tomography, NR: Not reported

Table 2. For technical characteristics of the studies included in the systematic review

Author	PET scanner	^{68}Ga-FAPI mean injected dose (MBq)	^{18}F-FDG mean injected dose (MBq)	Time interval between two scans	Scanning scope
Chen et al. (12)	Discovery MI, GE Healthcare	^{68}Ga-FAPI-04 (1.8-2.2 MBq)	^{18}F-FDG (3.7 MBq/kg)	Within 1 week	From the head to the upper thighs
Guo et al. (20)	Discovery MI, GE Healthcare	^{68}Ga-FAPI-04 (148-259 MBq)	^{18}F-FDG (3.7 MBq/kg)	Within 1 week	From the head to the upper thighs
Shi et al. (15)	PoleStar m660, Sinounion Healthcare	68Ga-FAPI-04 (3.59±0.47 MBq/kg)	^{18}F-FDG (3.7 MBq/kg)	Within 3 days	NG
Siripongsatian et al. (17)	64-slice Siemens Biograph vision scanner	^{68}Ga-FAPI-46 (2.59 MBq/kg)	^{18}F-FDG (2.59 MBq/kg)	Within 1 week	NG
Wang et al. (16)	FAPI: mMI510, Union imaging FDG: Biograph mCT Flow scanner, Siemens	^{68}Ga-FAPI-04 (185 MBq)	^{18}F-FDG (NG)	Within 1 day	NG
Pang et al. (13)	Discovery MI, GE Healthcare	Ga-FAP-2286 (1.8-2.2 MBq/kg) Ga-FAP-2286 (dose NG)	288.1±28.4 MBq (227.5-332.4	Within 1 week	NG
Lan et al. (14)	uMI780, United Imaging Healthcare	^{68}Ga-FAPI-04 (1.85 MBq/kg)	^{18}F-FDG (3.7 MBq/kg)	Within 3 days	Skull base to upper thigh + separate head scan
Rajaraman et al. (19)	Discovery DR, GE Healthcare	^{68}Ga-FAPI-04 (185- 370 MBq)	^{18}F-FDG (3.7 MBq/kg)	Within 1 week	NG
Jinghua et al. (18)	NG	^{68}Ga-FAPI-04 (2.04 ± 0.22 MBq/kg)	^{18}F-FDG (3.7±0.19 MBq/kg)	Within 1 week	From the head to the upper thighs

FAPI: Fibroblast-activation-protein inhibitors, ^{18}F-FDG: Fluorine-18-fluorodeoxyglucose, PET: Positron emission tomography, CT: Computed tomography, MRI: Magnetic resonance imaging, NG: Not given

Table 3. Semi-quantitative parameters of FAPI PET/CT and 18F FDG PET/CT for the studies included in the systematic review

Study	Tumor	No. of patients	SUV_{max} mean/median		TBR mean/median	
			FAPI	FDG	FAPI	FDG
Chen et al. (12)	HCC + CC	11	Median: 16.18 (7.24-25.97)	3.34 (2.08-10.7)	NR	NR
Guo et al. (20)	HCC	16	Median: 11.47 (4.66-21.03)	4.28 (3.25-10.81)	4.97 (1.05-10.49)	1.16 (0.96-4.21)
	CC	7	Median: 16.51 (8.34-23.21)	4.22 (2.63-11.26)	6.95 (2.15-10.62)	1.49 (0.89-4.41)
Shi et al. (15)	HCC	14	Mean: 8.47±4.06	4.86±3.58	7.13±5.5	2.39±2.21
	CC	3	Mean: 14.14±2.2	9.19±3.6	26.46±4.94	4.42±1.94
Siripongsatian et al. (17)	HCC	7	Median: 9.65 (4.98-18.89)	5.53 (3.37-23.23)	7.9 (2.03-13.54)	1.96 (1.25-6.95)
	CC	12	Median: 19.82 (5.27-30.25)	4.89 (3.38-23.23)	21.08 (3.59- 35.18)	1.47 (0.98-7.74)
Wang et al. (16)	HCC only	25	Mean: 6.96±5.01	5.89±3.38	11.9±8.35	3.14±1.59
Pang et al. (13)	HCC + CC	11	Median: 11.3 (2.5-28.9)	4.8 (3.1-9.7)	5.2 (1.5-9.4)	1.5 (1-3.5)
Lan et al. (14)	HCC + CC	16	Mean: 10.22±5.32	6.16±5.07	NR	NR
Rajaraman et al. (19)	HCC	6	Median: 11.47 (10.8-12.07)	13.4 (8.68-18.12)	2.15 (2.04-2.27)	4.72 (3.53-5.92)
	CC	18	Median: 17.7 (6.54-20.53)	7.26 (4.42-16.3)	7.15 (1.53-21.14)	3.01 (1.86-5.66)
Jinghua et al. (18)	HCC	38	17.25±6.72	10.80±5.22	NR	NR

FAPI: Fibroblast-activation-protein inhibitors, ^{18}F-FDG: Fluorine-18-fluorodeoxyglucose, PET: Positron emission tomography, CT: Computed tomography, MRI: Magnetic resonance imaging, NR: Not reported, HCC: Hepatocellular carcinoma, CC: Cholangiocarcinoma, SUV_{max}: Maximum standardized uptake value

histotypes i.e., HCC and intrahepatic cholangiocellular carcinoma separately. Diagnostic accuracy of FAPI PET/CT and ^{18}F-FDG PET/CT in individual studies is given in Table 5.

For primary liver tumors (staging as well as recurrent tumors), per lesion analysis was performed in 9 studies and overall pooled sensitivity for FAPI PET/CT vs ^{18}F-FDG PET/CT was 94.3% (range: 85.4-100%; 95% CI: 90.6-96.8%; I^2: 62%) and 56.1 (range: 39.0-84.2%; 95% CI: 49.7-62.5%; I^2: 65.8%) respectively (Figure 3). While data for calculation of pooled specificity was available for 5 studies only and revealed a pooled specificity of 89.3% (range: 75-100%, 95% CI: 71.8-97.7%) for FAPI PET/CT and 96.4% (range 87.5-100%; 95% CI: 81.7-99.9%; I^2: 0%) for ^{18}F-FDG PET/CT (Figure 4). The area under the curve (AUC) of ^{68}Ga-FAPI was 0.956 while for ^{18}F-FDG PET/CT was 0.682.

Per patient analysis for pooled sensitivity and specificity could be performed only in 8 and 4 studies, respectively. Sensitivity and specificity for FAPI PET/CT were 98.1% (range: 95.7-100%; 95% CI: 94.6-99.6%; I^2: 0%) and 86.4% (range: 75-100%; 95% CI: 65.1-97.1%; I^2: 0%) (Figure 5A, 5B, 6A, 6B) while for ^{18}F-FDG PET/CT these were 62.9% (range: 45.5-84.2%; 95% CI: 54.9-70.4%; I^2: 56.6%) and 95.5% (range: 87.5-100%; 95% CI: 77.2-99.9%; I^2: 0%) respectively (Figure 5C, 5D, 6C, 6D). The AUC of ^{68}Ga-FAPI was 0.989 while for ^{18}F-FDG PET/CT was 0.702 (Figure 7). The mean difference in the pooled sensitivity was statistically significant (p=0.02).

For evaluation of individual histotypes, only 6 studies provided required information. For HCC patient-based analysis revealed a pooled sensitivity of 98.5% (range: 93.8-100%; 95% CI: 91.7%-100%; I^2: 0%) for FAPI PET/CT and 60.9% (range: 40-75%; 95% CI: 47.9-72.9%; I^2: 0%) for FDG PET/CT (Figure 8). For CC, pooled Sn was 97.6% (range: 94.4-100%; 95% CI: 91.6-99.7%; I^2: 0%) for FAPI PET/CT and 67.5% (range: 40-100%; 95% CI: 56.3-77.4%; I^2: 63.5%) for FDG PET/CT (Figure 9). The per-lesion analysis for the same is given in Figure 10 and 11.

For detection of recurrent tumors, FAPI PET/CT showed much higher pooled sensitivity than ^{18}F-FDG PET/CT. Pooled Sn for FAPI PET/CT was 100% (95% CI: 82.4-100%; I^2: 0%), compared to 32% (95% CI: 13-57%; I^2: 65.2%) for ^{18}F-FDG PET/CT (Figure 12). For primary tumor staging, FAPI PET/CT revealed pooled Sn of 97.7% (range: 95.7-100%; 95% CI: 91.9-99.7%; I^2: 0%) while ^{18}F-FDG PET/CT had pooled

Table 4. Quality Assessment of Diagnostic Accuracy Studies-2

Study, year	Risk of bias				Applicability concerns		
	Patient selection	Index test	Reference standard	Flow and timing	Patient selection	Index test	Reference standard
Chen et al. (12)	Low	Low	Low	Low	Low	Low	Low
Guo et al. (20)	Low	Low	Low	Low	Low	Low	Low
Shi et al. (15)	Low	Unclear	Low	Low	Low	Unclear	Low
Siripongsatian et al. (17)	Low	Low	Low	Low	Low	Low	Low
Wang et al. (16)	Low	Low	Low	Low	Low	Low	Low
Pang et al. (13)	Low	High	Low	Low	Low	Unclear	Low
Lan et al. (14)	Low	Low	Low	Unclear	Low	Low	Low
Rajaraman et al. (19)	Low	Unclear	Low	Low	Low	Unclear	Low
Jinghua et al. (18)	Low	Low	Low	Low	Low	Low	Low

FAPI: Fibroblast-activation-protein inhibitors, ^{18}F-FDG: Fluorine-18-fluorodeoxyglucose, PET: Positron emission tomography, CT: Computed tomography, MRI: Magnetic resonance imaging, NR: Not reported

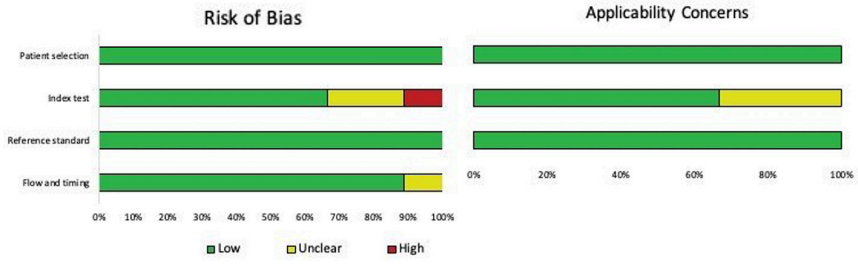

Figure 2. Summary of quality of the studies, risk of bias and applicability concerns of the included studies as per the QUADAS-2

QUADAS-2: Quality Assessment of Diagnostic Accuracy Studies-2

Table 5. Diagnostic performance of FAPI PET/CT and ^{18}F-FDG PET/CT in for evaluation of liver tumors									
Author	No. of patients	FAPI PET/CT				^{18}F-FDG PET/CT			
		Sensitivity (%)		Specificity (%)		Sensitivity (%)		Specificity (%)	
		Value	95% CI	Value	95% CI	Value	95% CI	Value	95% CI
Chen et al. (12)	11	100	71.5-100	NR	NR	45.5	16.7-76.6	NR	NR
Guo et al. (20)	23	95.7	78.1-99.9	NR	NR	65.2	42.7-83.6	NR	NR
Shi et al. (15)	20	100	80.5-100	100	29.2-100	58.8	32.9-81.6	100	29.2-100
Siripongsatian et al. (17)	27	100	82.4-100	75	34.9-96.8	52.6	28.9-75.6	87.5	47.3-99.7
Pang et al. (13)	12	100	71.5-100	100	25-100	45.5	16.7-17.6	100	25-100
Lan et al. (14)	16	100	79.4-100	NR	NR	75	47.6-92.7	NR	NR
Rajaraman et al. (19)	34	95.8	78.9-99.9	90	55.5-99.7	45.8	25.6-67.2	100	69.2-100
Jinghua et al. (18)	38	97.4	86.2-99.9	NR	NR	84.2	68.7-94	NR	NR
FAPI: Fibroblast-activation-protein inhibitors, ^{18}F-FDG: Fluorine-18-fluorodeoxyglucose, PET: Positron emission tomography, CT: Computed tomography, CI: Confidence interval									

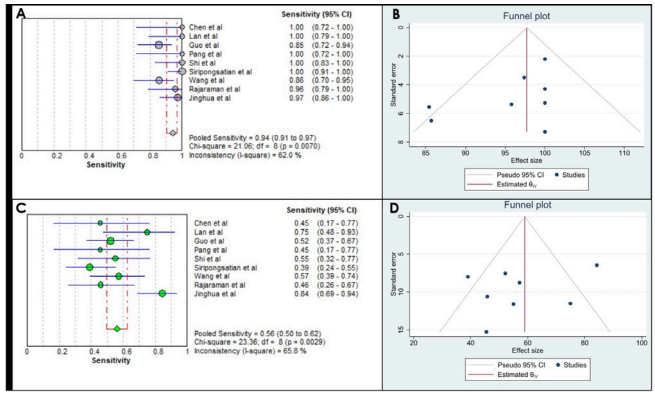

Figure 3. Forest and funnel plots showing pooled sensitivity of FAPI PET/CT (A, B) vs. ^{18}F-FDG PET/CT (C, D) in detection of liver malignancies on per lesion analysis

FAPI: Fibroblast-activation-protein inhibitors, ^{18}F-FDG: Fluorine-18-fluorodeoxyglucose, PET/CT: Positron emission tomography/computed tomography, CI: Confidence interval

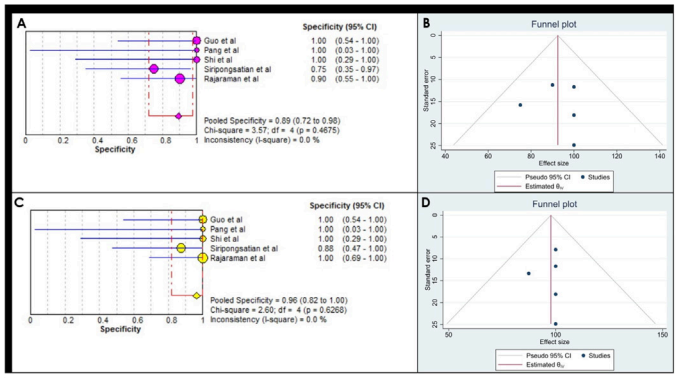

Figure 4. Forest and funnel plots showing pooled specificity of FAPI PET/CT (A, B) vs. ^{18}F-FDG PET/CT (C, D) in detection of liver malignancies on per lesion analysis

FAPI: Fibroblast-activation-protein inhibitors, ^{18}F-FDG: Fluorine-18-fluorodeoxyglucose, PET/CT: Positron emission tomography/computed tomography, CI: Confidence interval

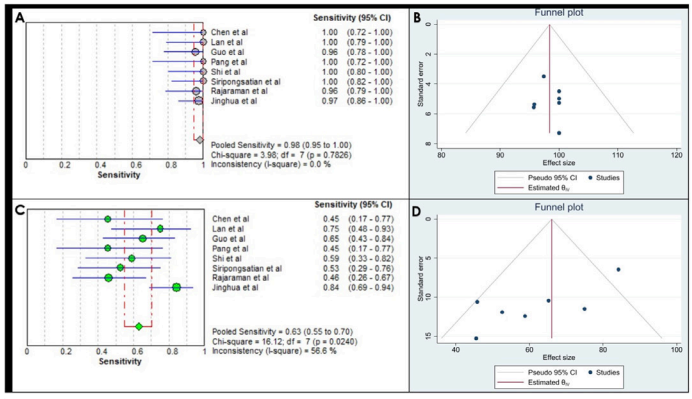

Figure 5. Forest and funnel plots showing pooled sensitivity of FAPI PET/CT (A, B) vs. ^{18}F-FDG PET/CT (C, D) in detection of liver malignancies on per patient analysis

FAPI: Fibroblast-activation-protein inhibitors, ^{18}F-FDG: Fluorine-18-fluorodeoxyglucose, PET/CT: Positron emission tomography/computed tomography, CI: Confidence interval

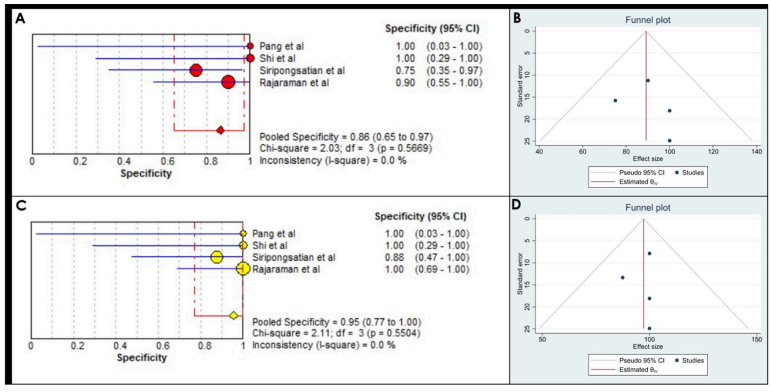

Figure 6. Forest and funnel plots showing pooled specificity of FAPI PET/CT (A, B) vs. ^{18}F-FDG PET/CT (C, D) in detection of liver malignancies on per patient analysis

FAPI: Fibroblast-activation-protein inhibitors, ^{18}F-FDG: Fluorine-18-fluorodeoxyglucose, PET/CT: Positron emission tomography/computed tomography, CI: Confidence interval

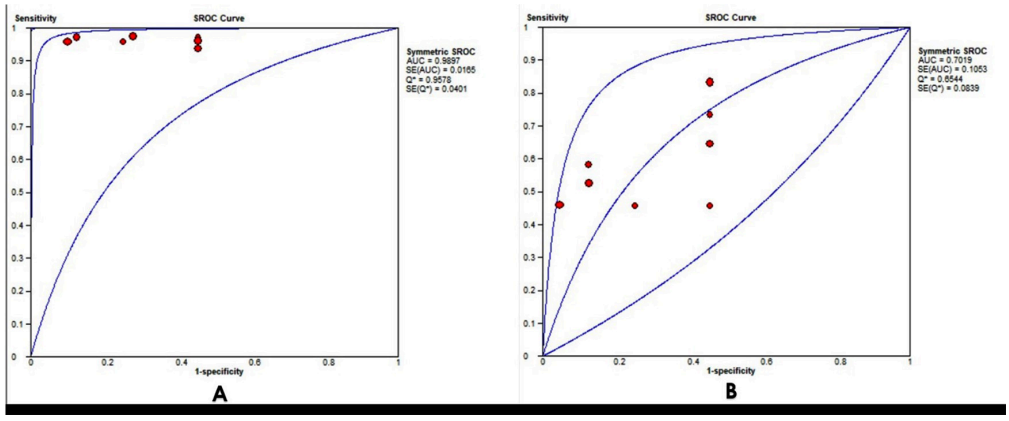

Figure 7. Summary receiver operating characteristics for ^{18}F-FDG (A) and FAPI (B)

FAPI: Fibroblast-activation-protein inhibitors, ^{18}F-FDG: Fluorine-18-fluorodeoxyglucose, ROC: Receiver operating characteristic, AUC: Area under the curve

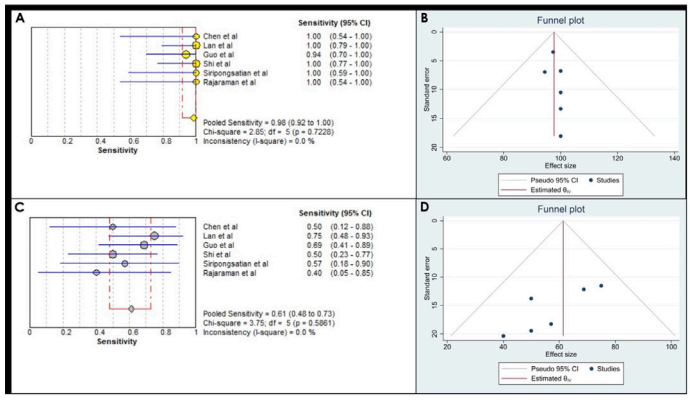

Figure 8. Forest and funnel plots showing pooled sensitivity of FAPI PET/CT (A, B) vs. ^{18}F-FDG PET/CT (C, D) in detection of hepatocellular carcinoma on per patient analysis

FAPI: Fibroblast-activation-protein inhibitors, ^{18}F-FDG: Fluorine-18-fluorodeoxyglucose, PET/CT: Positron emission tomography/computed tomography, CI: Confidence interval

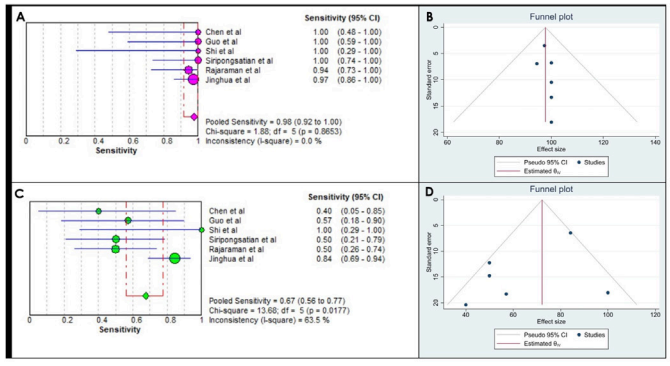

Figure 9. Forest and funnel plots showing pooled sensitivity of FAPI PET/CT (A, B) vs. ^{18}F-FDG PET/CT (C, D) in detection of cholangiocarcinoma on per patient analysis

FAPI: Fibroblast-activation-protein inhibitors, ^{18}F-FDG: Fluorine-18-fluorodeoxyglucose, PET/CT: Positron emission tomography/computed tomography, CI: Confidence interval

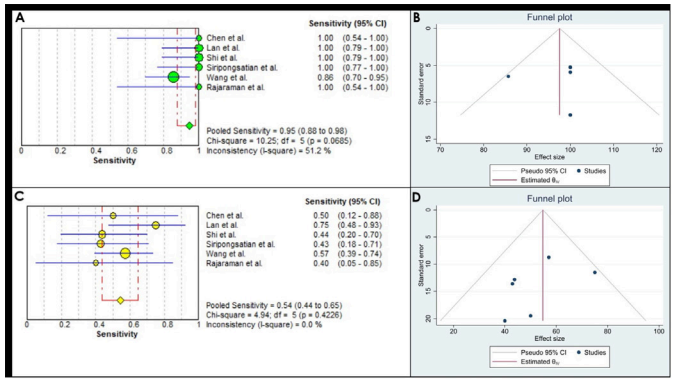

Figure 10. Forest and funnel plots showing pooled sensitivity of FAPI PET/CT (A, B) vs. ^{18}F-FDG PET/CT (C, D) in detection of hepatocellular carcinoma on per lesion analysis

FAPI: Fibroblast-activation-protein inhibitors, ^{18}F-FDG: Fluorine-18-fluorodeoxyglucose, PET/CT: Positron emission tomography/computed tomography, CI: Confidence interval

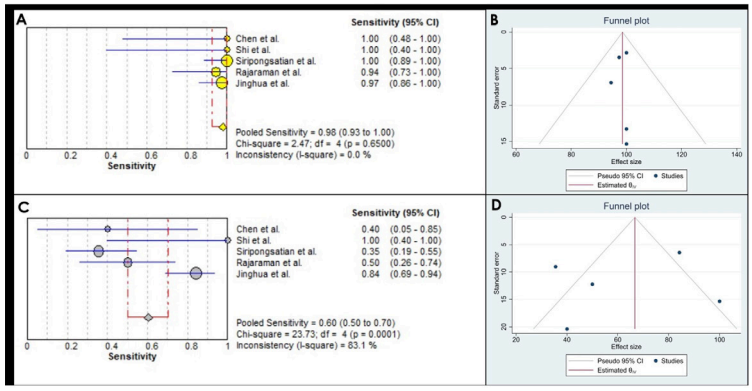

Figure 11. Forest and funnel plots showing pooled sensitivity of FAPI PET/CT (A, B) vs. ^{18}F-FDG PET/CT (C, D) in detection of cholangiocarcinoma on per lesion analysis

FAPI: Fibroblast-activation-protein inhibitors, ^{18}F-FDG: Fluorine-18-fluorodeoxyglucose, PET/CT: Positron emission tomography/computed tomography, CI: Confidence interval

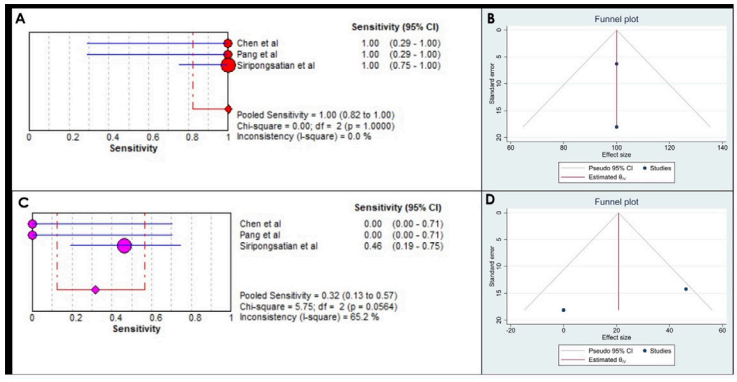

Figure 12. Forest and funnel plots showing pooled sensitivity of FAPI PET/CT (A, B) vs. ^{18}F-FDG PET/CT (C, D) in detection of recurrent liver tumors on per patient analysis

FAPI: Fibroblast-activation-protein inhibitors, ^{18}F-FDG: Fluorine-18-fluorodeoxyglucose, PET/CT: Positron emission tomography/computed tomography, CI: Confidence interval

Sn of 58.1% (range: 45.8-66.7%; 95% CI: 47.0-68.7%; I^2: 0%) (Figure 13) (Table 6). For detection of extrahepatic metastatic disease, pooled sensitivity could be evaluated only in 3 studies (Table 7). FAPI PET/CT had a pooled Sn of 92.2% (range: 88.1-100%; 95% CI: 87.8-95.4%; I^2: 77.4%) while for FDG PET/CT pooled Sn was 72.4% (range: 69.8-76.5%; 95% CI: 65.9-78.2%; I^2: 0%) (Figure 14).

All the studies included in the meta-analyses have compared the maximum standardized uptake value (SUV_{max}) and/or TBR values of ^{68}Ga-FAPI PET/CT and ^{18}F-FDG PET/CT in primary liver tumors. Overall, mean/median SUV_{max} was found to be higher in ^{68}Ga-FAPI PET/CT compared to ^{18}F-FDG PET/CT. However, in study by Rajaraman et al. (19) SUV_{max} when compared among different histotypes, SUV_{max} of HCC was higher for FDG PET/CT than FAPI PET/CT which was in contrast to the rest of the studies. No adverse event to FAPI or FDG PET/CT was reported in any of the included studies. No pharmacological or physiological effects occurred in responses to FAPI administration. None of the articles had declared any conflicts of interest.

Discussion

Liver malignancies represent one of the most common malignancies worldwide. Liver cancers are generally associated with poor prognosis. HCC, the most common liver tumor, carries a 5-year survival and disease-free survival as low as 15.6 and 21.5% respectively (21). The survival depends on the stage at diagnosis with median survival of early, intermediate and advanced stages with preserved hepatic function being ~36, ~16 and ~6 months, respectively (1). Some recent studies have reported improved survival reaching as high as 70% in early stages where curative

treatment options are feasible, thereby making early diagnosis and accurate staging utmost important (21).

FDG PET/CT is most common function modality used for oncological imaging. However, it has limited role in detection of primary liver tumors, especially in HCC where sensitivity is 40-68% compared to 68% for CECT (16,22). Similarly, in CC, FDG PET/CT fails to offer any significant advantage over conventional imaging for primary tumor

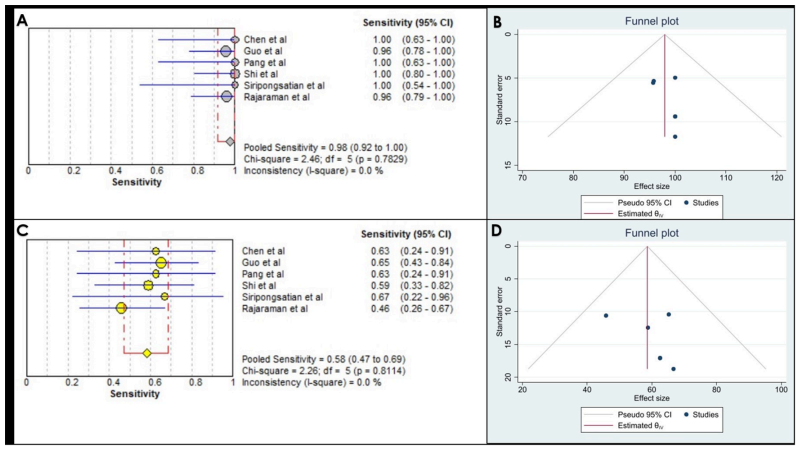

Figure 13. Forest and funnel plots showing pooled sensitivity of FAPI PET/CT (A, B) vs. ^{18}F-FDG PET/CT (C, D) in staging liver malignancies on per patient analysis

FAPI: Fibroblast-activation-protein inhibitors, ^{18}F-FDG: Fluorine-18-fluorodeoxyglucose, PET/CT: Positron emission tomography/computed tomography, CI: Confidence interval

Table 6. Pooled diagnostic sensitivity and specificity of the analysed data

		No. of studies	FAPI PET/CT	95%CI	^{18}F-FDG PET/CT	95% CI
Per patient analysis	Pooled Sn	8	98.1%	94.6-99.6	62.9%	54.9-70.4
	Pooled Sp	4	86.4%	65.1-97.1	95.5%	77.2-99.9
Per lesion analysis	Pooled Sn	9	94.3%	90.6-96.8	56.1%	49.7-62.5
	Pooled Sp	5	89.3%	71.8-97.7	96.4%	81.7-99.9
Staging	Pooled Sn	6	97.7%	91.9-99.7	58.1%	47-68.7
Recurrent disease	Pooled Sn	3	100%	82.4-100	32%	13-57
HCC per patient	Pooled Sn	6	98.5%	91.7-100	60.9%	47.9-72.9
HCC per lesion	Pooled Sn	6	95%	88.0-98.0	54%	44.0-65.0
CC per patient	Pooled Sn	6	97.6%	91.6-99.7	67.5%	56.3-77.4
CC per lesion	Pooled Sn	5	98%	93.0-100	60%	50.0-70.0
For extrahepatic metastasis	Pooled Sn	3	92.2%	87.8-95.4	72.4%	65.9-78.2

FAPI: Fibroblast-activation-protein inhibitors, ^{18}F-FDG: Fluorine-18-fluorodeoxyglucose, PET: Positron emission tomography, CT: Computed tomography, Sn: Sensitivity, Sp: Specificity, CI: Confidence interval, HCC: Hepatocellular carcinoma, CC: Cholangiocarcinoma

Table 7. Diagnostic performance of FAPI PET/CT and ^{18}F-FDG PET/CT in for evaluation of extrahepatic metastasis

Author	No. of extrahepatic lesions	FAPI PET/CT Sensitivity (%)		^{18}F- FDG PET/CT Sensitivity (%)	
		Value	95% CI	Value	95% CI
Guo et al. (20)	126	88.1	81.1-93.2	69.8	61-77.7
Shi et al. (15)	17	100	80.5-100	76.5	50.1-93.2
Siripongsatian et al. (17)	74	97.3	90.6-99.7	75.7	64.3-84.9

FAPI: Fibroblast-activation-protein inhibitors, ^{18}F-FDG: Fluorine-^{18}-fluorodeoxyglucose, PET: Positron emission tomography, CT: Computed tomography, CI: Confidence interval

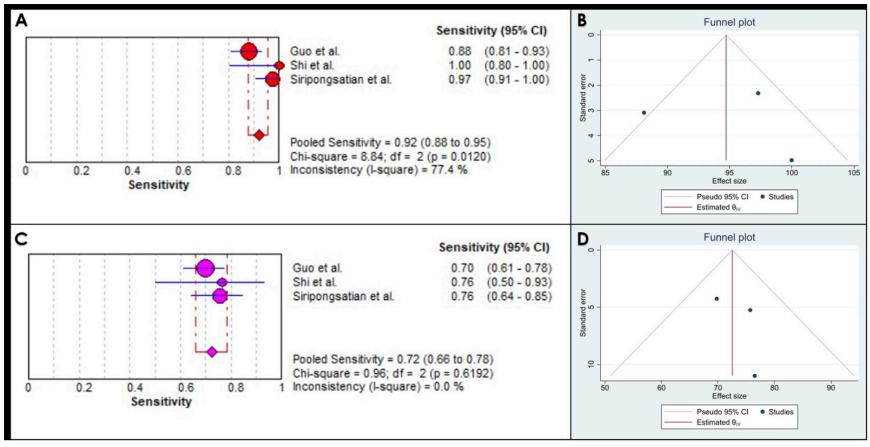

Figure 14. Forest and funnel plots showing pooled sensitivity of FAPI PET/CT (A, B) vs. ^{18}F-FDG PET/CT (C, D) in detection of extrahepatic metastatic disease on per lesion analysis

FAPI: Fibroblast-activation-protein inhibitors, ^{18}F-FDG: Fluorine-18-fluorodeoxyglucose, PET/CT: Positron emission tomography/computed tomography, CI: Confidence interval

detection. FDG PET/CT is found advantageous mainly in detection of extra-hepatic metastatic disease where it has sensitivity of 77-100% compared to 51.3% for conventional imaging (23). Current meta-analysis revealed a pooled sensitivity of 60.9% (95% CI: 47.9-72.9) for primary HCC and 67.5% (95% CI: 56.3-77.4) for primary CC with an overall sensitivity of 62.9% (95% CI: 54.9-70.4) for all primary liver tumors (12-20). For extrahepatic metastasis, our meta-analysis revealed a sensitivity of 72.4% (95% CI: 65.9-78.2) (12-20). Recent National Comprehensive Cancer Network guideline for hepatobiliary malignancies do not routinely recommend FDG PET/CT owing to its limited sensitivity, however, it is recommended in cases with equivocal findings due to its high specificity and predictive value (24). To overcome these limitations of functional imaging, various strategies have been adopted including use of diagnostic CECT with FDG PET (^{18}F-FDG PET/CECT) and use of novel radiotracers like ^{11}C-acetate, ^{68}Ga-FAPI, ^{8}F-fluorocholine, ^{11}C-choline, ^{68}Ga-labeled asparagine-glycine-arginine etc.

FAPI targets the fibroblast activating protein, a type II transmembrane serine protease, present on cancer associated fibroblasts. These are overexpressed in majority of epithelial tumours as well as in tumors with prominent desmoplastic response like CC. The high expression of FAPs in liver tumors combined with low background liver activity improves the detection rate of liver cancer. FAPI PET/CT has shown sensitivity as high as 100% for detection of primary liver tumors as well as extrahepatic metastasis in some studies (6). In our study, we found a pooled sensitivity of 98.5% (95% CI: 91.7-100) for primary HCC and 97.6% (95% CI: 91.6-99.7) for primary CC with an overall sensitivity of 98.1% (95% CI: 94.6-99.6) for all primary liver tumors. For extrahepatic metastasis, our meta-analysis revealed a sensitivity of 92.2% (95% CI: 87.7-95.4) (12-20).

Recently, Liu et al. (10) performed a meta-analysis comparing the diagnostic performance of FAPI PET/CT and ^{18}F-FDG PET/CT in abdominopelvic malignancies. The authors also found higher primary lesion detection rate of 0.98 (95% CI: 0.95-1.00; I^2 =22.58%, p=0.23) with FAPI PET/CT compared to 0.76 (95% CI: 0.63-0.87; I^2 =82.48%, p=0.00) for FDG PET/CT. Similar to our study, the author found higher sensitivity for detection of metastatic disease with FAPI PET/CT [Sn-0.918 (95% CI: 0.900-0.933; I^2 =98.2%)] compared to FDG PET/CT [Sn-0.714 (95% CI: 0.686-0.741; I^2 =95.1%)] (10). In the current meta-analysis, we also performed per lesion analysis of the pooled sensitivity and specificity for detection of hepatic lesions which revealed a sensitivity of 56.1% (95% CI: 49.7-62.5) for FDG vs. 94.3% (95% CI: 90.6-96.8) for FAPI PET/CT. These findings were in line with the previously published studies.

There are few short-comings associated with this meta-analysis like heterogeneity among the studies, the publication bias and small number of studies available for the subgroup analysis.

Conclusion

Overall, in the present meta-analysis we found a superior sensitivity of FAPI PET/CT compared to FDG PET/CT in both per patient and per lesion analysis of primary liver tumor detection. Also, sub-group analysis revealed superior sensitivity of FAPI PET/CT for detection of both HCC and CC as well as primary staging, recurrence detection and extrahepatic metastatic disease. Thus, ^{68}Ga-FAPI appears

promising and can replace FDG PET/CT for staging and work-up of liver tumors. However, FAPI is still in its naive stages and these results need to be further confirmed by larger, multicentric and prospective studies.

Ethics

Ethics Committee Approval: Ethical approval has been taken from the All India Institute of Medical Sciences Bhubaneswar Ethics Committee with approval number T/IM-NF/Nucl. Med/23/19 (date: 15.05.2023).

Informed Consent: As this is a meta-analysis of the already published articles and no patient is directly involved, so taking consent is no applicable.

Authorship Contributions

Concept: P.S., G.K.P., K.A., Design: P.S., G.K.P., Analysis or Interpretation: T.S., G.K.P., K.A., Literature Search: P.S., A.R., Writing: P.S., T.S.

Conflict of Interest: No conflict of interest was declared by the authors.

Financial Disclosure: The authors declared that this study has received no financial support.

References

1. Dasgupta P, Henshaw C, Youlden DR, Clark PJ, Aitken JF, Baade PD. Global Trends in Incidence Rates of Primary Adult Liver Cancers: A Systematic Review and Meta-Analysis. Front Oncol 2020;10:171.
2. Sung H, Ferlay J, Siegel RL, Laversanne M, Soerjomataram I, Jemal A, Bray F. Global Cancer Statistics 2020: GLOBOCAN Estimates of Incidence and Mortality Worldwide for 36 Cancers in 185 Countries. CA Cancer J Clin 2021;71:209-249.
3. Shetty VV, Kellarai A. Comprehensive Review of Hepatocellular Carcinoma in India: Current Challenges and Future Directions. JCO Glob Oncol 2022;8:e2200118.
4. Musunuri B, Shetty S, Bhat G, Udupa K, Pai A. Profile of patients with hepatocellular carcinoma: An experience from a tertiary care center in India. Indian J Gastroenterol 2022;41:127-134..
5. Singal AG, Parikh ND, Rich NE, John BV, Pillai A. Hepatocellular Carcinoma Surveillance and Staging. 2019 Aug 6. In: Hoshida Y, editor. Hepatocellular Carcinoma: Translational Precision Medicine Approaches. Cham (CH): Humana Press; 2019.
6. Mori Y, Dendl K, Cardinale J, Kratochwil C, Giesel FL, Haberkorn U. FAPI PET: Fibroblast Activation Protein Inhibitor Use in Oncologic and Nononcologic Disease. Radiology 2023;306:e220749.
7. Cho KJ, Choi NK, Shin MH, Chong AR. Clinical usefulness of FDG-PET in patients with hepatocellular carcinoma undergoing surgical resection. Ann Hepatobiliary Pancreat Surg 2017;21:194-198.
8. Lu RC, She B, Gao WT, Ji YH, Xu DD, Wang QS, Wang SB. Positron-emission tomography for hepatocellular carcinoma: Current status and future prospects. World J Gastroenterol 2019;25:4682-4695.
9. Parida GK, Panda RA, Agrawal K. Impact of fluorine-18-fluorodeoxyglucose PET/computed tomography in staging of patients with gallbladder cancer: a systematic review and meta-analysis. Nucl Med Commun 2021;42:846-854.
10. Liu X, Liu H, Gao C, Zeng W. Comparison of 68Ga-FAPI and 18F-FDG PET/CT for the diagnosis of primary and metastatic lesions in abdominal and pelvic malignancies: A systematic review and meta-analysis. Front Oncol 2023;13:1093861.
11. Whiting PF, Rutjes AW, Westwood ME, Mallett S, Deeks JJ, Reitsma JB, Leeflang MM, Sterne JA, Bossuyt PM; QUADAS-2 Group. QUADAS-2: a revised tool for the quality assessment of diagnostic accuracy studies. Ann Intern Med 2011;155:529-536.
12. Chen H, Pang Y, Wu J, Zhao L, Hao B, Wu J, Wei J, Wu S, Zhao L, Luo Z, Lin X, Xie C, Sun L, Lin Q, Wu H. Comparison of [68Ga]Ga-DOTA-FAPI-04 and [18F] FDG PET/CT for the diagnosis of primary and metastatic lesions in patients with various types of cancer. Eur J Nucl Med Mol Imaging 2020;47:1820-1832.
13. Pang Y, Zhao L, Meng T, Xu W, Lin Q, Wu H, Zhang J, Chen X, Sun L, Chen H. PET Imaging of Fibroblast Activation Protein in Various Types of Cancer Using 68Ga-FAP-2286: Comparison with 18F-FDG and 68Ga-FAPI-46 in a Single-Center, Prospective Study. J Nucl Med 2023;64:386-394.
14. Lan L, Liu H, Wang Y, Deng J, Peng D, Feng Y, Wang L, Chen Y, Qiu L. The potential utility of [68 Ga]Ga-DOTA-FAPI-04 as a novel broad-spectrum oncological and non-oncological imaging agent-comparison with [18F] FDG. Eur J Nucl Med Mol Imaging 2022;49:963-979.
15. Shi X, Xing H, Yang X, Li F, Yao S, Zhang H, Zhao H, Hacker M, Huo L, Li X. Fibroblast imaging of hepatic carcinoma with 68Ga-FAPI-04 PET/CT: a pilot study in patients with suspected hepatic nodules. Eur J Nucl Med Mol Imaging 2021;48:196-203.
16. Wang H, Zhu W, Ren S, Kong Y, Huang Q, Zhao J, Guan Y, Jia H, Chen J, Lu L, Xie F, Qin L. 68Ga-FAPI-04 Versus 18F-FDG PET/CT in the Detection of Hepatocellular Carcinoma. Front Oncol 2021;11:693640.
17. Siripongsatian D, Promteangtrong C, Kunawudhi A, Kiatkittikul P, Boonkawin N, Chinnanthachai C, Jantarato A, Chotipanich C. Comparisons of Quantitative Parameters of Ga-68-Labelled Fibroblast Activating Protein Inhibitor (FAPI) PET/CT and [18F]F-FDG PET/CT in Patients with Liver Malignancies. Mol Imaging Biol 2022;24:818-829.
18. Jinghua L, Kui X, Deliang G, Bo L, Qian Z, Haitao W, Yaqun J, Dongde W, Xigang X, Ping J, Shengli T, Zhiyong Y, Yueming H, Zhonglin Z, Yong H, Yufeng Y. Clinical prospective study of Gallium 68 (68Ga)-labeled fibroblast-activation protein inhibitor PET/CT in the diagnosis of biliary tract carcinoma. Eur J Nucl Med Mol Imaging 2023;50:2152-2166.
19. Rajaraman V, Meenakshi LA, Selvaraj AJ, Pottakkat B, Halanaik D. Role of 68 Ga-FAPI PET/CT in Assessing Hepatobiliary Malignancies : A Prospective Pilot Study. Clinical Nuclear Medicine 2023;48:e281-e288.
20. Guo W, Pang Y, Yao L, Zhao L, Fan C, Ke J, Guo P, Hao B, Fu H, Xie C, Lin Q, Wu H, Sun L, Chen H. Imaging fibroblast activation protein in liver cancer: a single-center post hoc retrospective analysis to compare [68Ga]Ga-FAPI-04 PET/CT versus MRI and [18F]-FDG PET/CT. Eur J Nucl Med Mol Imaging 2021;48:1604-1617.
21. Ding J, Wen Z. Survival improvement and prognosis for hepatocellular carcinoma: analysis of the SEER database. BMC Cancer 2021;21:1157.
22. Colli A, Fraquelli M, Casazza G, Massironi S, Colucci A, Conte D, Duca P. Accuracy of ultrasonography, spiral CT, magnetic resonance, and alpha-fetoprotein in diagnosing hepatocellular carcinoma: a systematic review. Am J Gastroenterol 2006;101:513-523.
23. Lee SM, Kim HS, Lee S, Lee JW. Emerging role of 18F-fluorodeoxyglucose positron emission tomography for guiding management of hepatocellular carcinoma. World J Gastroenterol 2019;25:1289-1306.
24. Benson AB 3rd, Abrams TA, Ben-Josef E, Bloomston PM, Botha JF, Clary BM, Covey A, Curley SA, D'Angelica MI, Davila R, Ensminger WD, Gibbs JF, Laheru D, Malafa MP, Marrero J, Meranze SG, Mulvihill SJ, Park JO, Posey JA, Sachdev J, Salem R, Sigurdson ER, Sofocleous C, Vauthey JN, Venook AP, Goff LW, Yen Y, Zhu AX. NCCN clinical practice guidelines in oncology: hepatobiliary cancers. J Natl Compr Canc Netw 2009;7:350-391.

Original Article

Mol Imaging Radionucl Ther 2024;33:90-93 *DOI:10.4274/mirt.galenos.2024.48254*

Can Pantoprazole be Used for Premedication in Meckel Scintigraphy?

Pantoprazol Meckel Sintigrafisinde Premedikasyon Amacıyla Kullanılabilir mi?

Aziz Gültekin, Tarık Şengöz, Samiye Demirezen, Doğangün Yüksel

Pamukkale University Faculty of Medicine, Department of Nuclear Medicine, Denizli, Türkiye

Abstract

Objectives: Meckel scintigraphy is used to diagnose Meckel's diverticulum. Previously, premedication with ranitidine was the most frequently used method to increase the accuracy of scintigraphy. However, ranitidine can no longer be used because it is banned by the Food and Drug Administration. The aim of this study was to investigate the usability of pantoprazole as a premedication instead of ranitidine in Meckel scintigraphy.

Methods: Twelve New Zealand rabbits were used in this experimental study. Rabbits were divided into two groups: pantoprazole and control. Six rabbits were premedicated with pantoprazole for three days. Meckel scintigraphy was performed on all rabbits. Counts were made and compared by drawing regions of interest from the stomach walls.

Results: According to the findings of this experimental study, pantoprazole significantly increased Tc-99m-pertechnetate uptake in the stomach of rabbits on both visual and quantitative evaluation.

Conclusion: Pantoprazole increases the gastric wall uptake of Tc-99m-pertechnetate in rabbits and is a potential drug for premedication in Meckel scintigraphy.

Keywords: Meckel's diverticulum, Meckel scintigraphy, preclinical imaging, pantoprazole, premedication for Meckel scan

Öz

Amaç: Meckel divertikülü tanısında Meckel sintigrafisi kullanılmaktadır. Önceleri sintigrafi doğruluğunu artırmak amacıyla ranitidin ile premedikasyon en sık kullanılan yöntemdi. Ancak Gıda ve İlaç Dairesi tarafından yasaklandığı için artık kullanılamamaktadır. Bu çalışmanın amacı Meckel sintigrafisinde ranitidin yerine pantoprazolün premedikasyon amacıyla kullanılabilirliğini araştırmaktır.

Yöntem: Bu deneysel çalışmada 12 Yeni Zelanda tavşanı kullanıldı. Tavşanlar pantoprazol ve kontrol grubu olmak üzere iki gruba ayrıldı. Altı tavşana üç gün boyunca pantoprazol ile premedikasyon uygulandı. Hem kontrol grubu hem de pantoprazole grubu tüm tavşanlara Meckel sintigrafisi yapıldı. Mide duvarından ilgi alanları çizilerek sayımlar yapıldı ve karşılaştırıldı.

Bulgular: Bu deneysel çalışmadan elde ettiğimiz bulgulara göre pantoprazol, görsel ve kantitatif değerlendirme sonucunda tavşan midesinde Tc-99m-perteknetat alımını önemli ölçüde artırmaktadır.

Sonuç: Pantoprazol tavşanlarda Tc-99m-perteknetatın mide duvarına alımını artırır ve Meckel sintigrafisinde premedikasyon için kullanılabilecek potansiyel bir ilaçtır.

Anahtar kelimeler: Meckel divertikülü, Meckel sintigrafisi, klinik öncesi görüntüleme, pantoprazol, Meckel sintigrafisinde premedikasyon

Address for Correspondence: Aziz Gültekin Assoc. Prof., Pamukkale University Faculty of Medicine, Department of Nuclear Medicine, Denizli, Türkiye
Phone: +90 258 296 53 06 **E-mail:** agultekin@pau.edu.tr ORCID ID: orcid.org/0000-0002-0311-8077
Received: 15.12.2023 **Accepted:** 03.03.2024 **Epub:** 04.04.2024

Introduction

Only 30-60% of Meckel's diverticulum contains ectopic gastric mucosa. Meckel's diverticulum, which contains ectopic gastric mucosa, can be detected by Meckel scintigraphy. Tc-99m-pertechnetate is used as a radiopharmaceutical in Meckel scintigraphy (1,2,3). Tc-99m-pertechnetate is taken up by the cells of the gastric mucosa, which produce mucin and are then secreted into the intestine. Meckel scintigraphy with Tc-99m-pertechnetate is used to identify ectopic gastric mucosa in Meckel's diverticulum (4,5). This examination is widely used in diagnosis and has a wide accuracy range (6,7). Various premedication methods have been used to increase the accuracy of Meckel scintigraphy. The most commonly used preparations for this purpose are H2 receptor blockers (famotidine, cimetidine, and ranitidine), pentagastrin, and glucagon. Pentagastrin and glucagon are not suitable for use because of side effects (8,9,10,11). Ranitidine was the most frequently used preparation previously. The use of ranitidine has been banned by the Food and Drug Administration (FDA) because of its N-nitrosodimethylamine (NDMA) content. NDMA has been proven to cause lung, liver, and bladder cancer in animals (12,13). For the same reason, ranitidine preparations have been withdrawn from medical markets worldwide.

The primary purpose of premedication in Meckel scintigraphy is to reduce the secretion of Tc-99m-pertechnetate into the gastric lumen. Thus, Tc-99m-pertechnetate, which is taken up by the gastric mucosa, cannot pass into the small intestine, and small ectopic gastric mucosa collections within the intestine can be visualized more easily. Second, to maintain any activity within the ectopic gastric mucosa and reduce its dispersion distally. However, there is a debate about the major benefit and mode of action (8). Pantoprazole belongs to the group of proton pump inhibitors (PPIs). The effects of PPIs on the gastric mucosa are similar to those of ranitidine (14). However, there is no evidence that PPIs can be used for premedication in Meckel scintigraphy.

Our aim in this preclinical study was to measure Tc-99m-pertechnetate uptake in the stomach after pantoprazole premedication to investigate the potential of pantoprazole as premedication in Meckel scintigraphy.

Materials and Methods

This preclinical study was approved by the Pamukkale University Animal Experimentation Ethics Committee (no: PAUHDEK-2021/48, date: 24.02.2022). National and international directives on animal experiments were followed. Animal gender was not considered a factor in the experimental design. All rabbits were housed in separate cages and fed ad libitum with 12-h day and night cycles at 25 °C during all procedures. Twelve New Zealand rabbits (Oryctolagus cuniculus) weighing 2150-2500 g were divided into two groups as Pantoprazole (n=6) and control (n=6). Pantoprazole group rabbits were injected with 1 mg/kg of Pantoprazole (Pulcet, Nobel İlaç, İstanbul) through the ear vein for three days. All rabbits were fasted for 4 h before scintigraphic imaging. Ketamine 35 mg/kg (Keta-control 25 mL, Doğa İlaç, İstanbul) and Xylazine 5 mg/kg (Control 100 mL, Doğa İlaç, İstanbul) were injected intramuscularly to provide general anesthesia before scintigraphic imaging. Ear vascular access was established in the pantoprazole group rabbits. 37 mBq/kg Tc-99m-pertechnetate was intravenously injected 1 h after pantoprazole injection. Scintigraphic imaging was performed using a dual-detector hybrid gamma camera (2.5 mA, 120 kVp; Philips Brightview XBT). Dynamic planar imaging was performed for 1 hour (5 min/frame; total 6 frame). After anesthesia application to the control group rabbits, an auricular vascular access was established and 37 MBq/kg Tc-99m-pertechnetate was injected and imaged in the same manner. A flow chart of the rabbit experiment is shown in Figure 1.

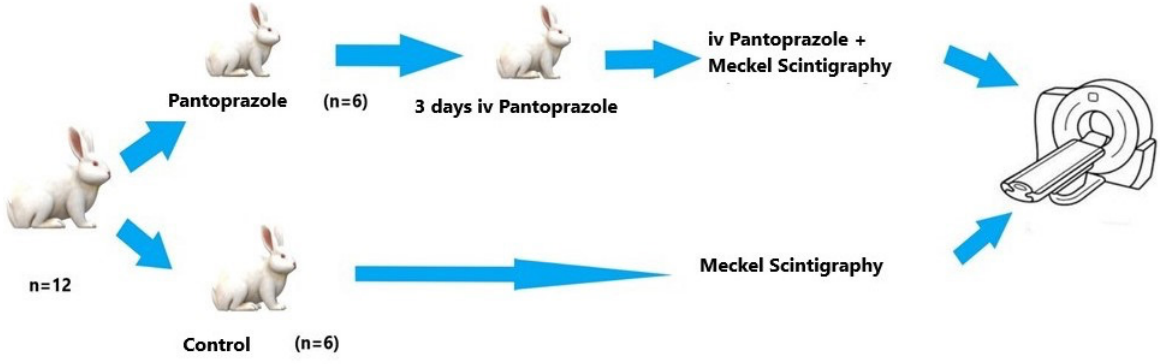

Figure 1. The flow chart of the rabbit experiment

All images were visually and quantitatively evaluated by an experienced nuclear medicine specialist. For quantitative analysis, regions of interest (ROI) were drawn from the stomach walls of all rabbits, and total counts were recorded. ROI areas obtained from the gastric wall were equal, and background correction was performed.

Statistical Analysis

Data were analyzed using SPSS 24.0 package software (IBM, Armonk, NY, USA). Continuous variables are given as mean ± standard deviation, and categorical variables are given as frequency and percentage. Because the groups did not follow a normal distribution, for independent group comparisons, we used the Mann-Whitney U test. A p-value of 0.05 was considered significant.

Results

In the visual evaluation, increased Tc-99m-pertechnetate uptake was observed in the stomach wall of rabbits premedicated with pantoprazole compared with the control group rabbits. In the control group, the accumulation of Tc-99m-pertechnetate secreted from the stomach to the intestines was observed (Figure 2).

In the quantitative evaluation, when the gastric wall counts of the rabbits premedicated with pantoprazole for 3 days were compared with the control group rabbits, Tc-99m-pertechnetate uptake was found to be significantly higher in the stomach of premedicated rabbits (p=0.006).

Discussion

A New Zealand rabbit was selected for this experimental study. Histological, structural, and experimental studies on the stomach have reported that the gastric mucosa of rabbits and humans are generally similar, but there may be differences in the number and regional distribution of cell types (15). According to the findings of this experimental study, as a result of visual and quantitative evaluation, pantoprazole significantly increases Tc-99m-pertechnetate uptake in the stomach. There is no similar study in the literature. H2 receptor blockers increase the sensitivity of Meckel scintigraphy. They reduce peptic secretion although the exact mechanism has not been elucidated. They delay the secretion of pertechnetate from parietal cells and mucus cells into the lumen. Therefore, H2 receptor blockers increase the sensitivity of the Meckel scintigraphy study by causing higher radionuclide concentrations in the stomach and Meckel's diverticulum (5,9,10,11,16,17).

Pantoprazole is an irreversible proton pump (H^+/K^+-ATPase) inhibitor that reduces acid secretion from gastric parietal cells. Pantoprazole is believed to increase pertechnetate uptake in the gastric mucosa by the same mechanism as H2 receptor blockers (18). In our study, we used pantoprazole for 3 days as premedication. We performed imaging 1 h after pantoprazole injection on the fourth day. PPIs have a long half-life. The half-life of pantoprazole is 46 h. Not all proton pumps are inactivated by the first dose of the drug; three days of treatment is needed to reach the full acid inhibition potential (19).

Study Limitations

Our study has a limitation. Because of their short half-lives, H2 receptor blockers are more suitable as premedications for Meckel scintigraphy than PPIs. However, there is currently no parenteral or pediatric syrup form of any H2 receptor blocker preparation. Therefore, the parenteral form of pantoprazole was preferred in our study.

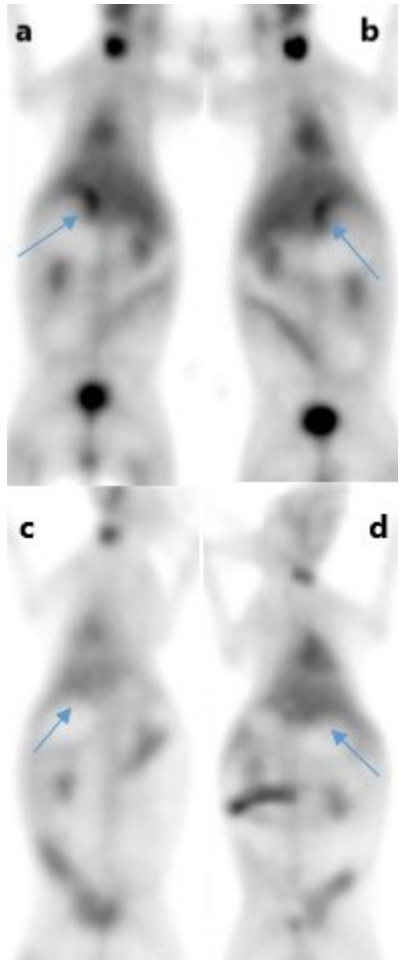

Figure 2. Tc-99m-pertechnetate uptake in the stomach wall of the rabbits premedicated with i.v. pantoprazole in Tc-99m-pertechnetate scintigraphy (a,b; blue arrows), physiological Tc-99m-pertechnetate uptake is observed in the gastric wall of the control group rabbits (c,d; blue arrows)

Table 1. Counts from the stomach wall rabbits premedicated with intravenous pantoprazole and control group			
	Pantoprazole (mean ± SD)	**Control (mean ± SD)**	**p-value**
Stomach	347719±58539	183514±55385	*0.006
SD: Standard deviation			

Conclusion

As a result, with the prohibition of ranitidine by the FDA, the need for new drugs that can be used as premedication for Meckel's diverticulum scintigraphy has emerged. Pantoprazole increases the gastric wall uptake of pertechnetate after three days of premedication and is a potential drug that can be used for premedication in Meckel scintigraphy. The results need to be confirmed by clinical studies.

Ethics

Ethics Committee Approval: This preclinical study was approved by the Pamukkale University Animal Experimentation Ethics Committee (no: PAUHDEK-2021/48, date: 24.02.2022). All national and international directives were complied with during the experiments.

Informed Consent: Animal experimental study.

Authorship Contributions

Surgical and Medical Practices: A.G., S.D., Concept: A.G., Design: A.G., T.Ş., Data Collection or Processing: A.G., S.D., Analysis or Interpretation: T.Ş., D.Y., Literature Search: A.G., Writing: A.G., D.Y.

Conflict of Interest: No conflict of interest was declared by the authors.

Financial Disclosure: The authors declared that this study has received no financial support.

References

1. Park JJ, Wolff BG, Tollefson MK, Walsh EE, Larson DR. Meckel diverticulum: the Mayo Clinic experience with 1476 patients (1950-2002). Ann Surg 2005;241:529-533.
2. Brown RL, Azizkhan RG. Gastrointestinal bleeding in infants and children: Meckel's diverticulum and intestinal duplication. Semin Pediatr Surg 1999;8:202-209.
3. Samain J, Maeyaert S, Geusens E, Mussen E. Sonographic findings of Meckel's diverticulitis. JBR-BTR 2012;95:103.
4. Datz FL, Christian PE, Hutson WR, Moore JG, Morton KA. Physiological and pharmacological interventions in radionuclide imaging of the tubular gastrointestinal tract. Semin Nucl Med 1991;21:140-152.
5. Hosseinnezhad T, Shariati F, Treglia G, Kakhki VR, Sadri K, Kianifar HR, Sadeghi R. 99mTc-Pertechnetate imaging for detection of ectopic gastric mucosa: a systematic review and meta-analysis of the pertinent literature. Acta Gastroenterol Belg 2014;77:318-327.
6. Sfakianakis GN, Conway JJ. Detection of ectopic gastric mucosa in Meckel's diverticulum and in other aberrations by scintigraphy: ii. indications and methods–a 10-year experience. J Nucl Med 1981;22:732-738.
7. Jain TP, Sharma R, Chava SP, Das CJ. Pre-operative diagnosis of Meckel's diverticulum: report of a case and review of literature. Trop Gastroenterol 2005;26:99-101.
8. Saremi F, Jadvar H, Siegel ME. Pharmacologic interventions in nuclear radiology: indications, imaging protocols, and clinical results. Radiographics 2002;22:477-490.
9. Spottswood SE, Pfluger T, Bartold SP, Brandon D, Burchell N, Delbeke D, Fink-Bennett DM, Hodges PK, Jolles PR, Lassmann M, Maurer AH, Seabold JE, Stabin MG, Treves ST, Vlajkovic M; Society of Nuclear Medicine and Molecular Imaging; European Association of Nuclear Medicine. SNMMI and EANM practice guideline for meckel diverticulum scintigraphy 2.0. J Nucl Med Technol 2014;42:163-169. Erratum in: J Nucl Med Technol 2016;44:51.
10. Wu H, Zhao X, Li Y, Zhao R. Reconsideration of the primary and secondary diagnostic criteria of Meckel's diverticulum scintigraphy. A study of 93 confirmed cases. Hell J Nucl Med 2017;20:11-16.
11. Vali R, Daneman A, McQuattie S, Shammas A. The value of repeat scintigraphy in patients with a high clinical suspicion for Meckel diverticulum after a negative or equivocal first Meckel scan. Pediatr Radiol 2015;45:1506-1514.
12. White CM, Hernandez AV. Ranitidine and Risk of N-Nitrosodimethylamine (NDMA) Formation. JAMA 2021;326:225-227.
13. White CM, Hernandez AV. Risk of N-Nitrosodimethylamine (NMDA) Formation With Ranitidine-Reply. JAMA 2021;326:2077-2078.
14. Cheer SM, Prakash A, Faulds D, Lamb HM. Pantoprazole: an update of its pharmacological properties and therapeutic use in the management of acid-related disorders. Drugs 2003;63:101-133.
15. Yaman M, Girgin A. Electron Microscopic Investigations of Rabbit Stomach Fundic Mucosa on the Prenatal and Postnatal Periods. F.Ü.Sağ. Bil.Vet.Derg 2005;19;37-42.
16. Kiratli PO, Aksoy T, Bozkurt MF, Orhan D. Detection of ectopic gastric mucosa using 99mTc pertechnetate: review of the literature. Ann Nucl Med 2009;23:97-105.
17. Diamond RH, Rothstein RD, Alavi A. The role of cimetidine-enhanced technetium-99m-pertechnetate imaging for visualizing Meckel's diverticulum. J Nucl Med 1991;32:1422-1424.
18. Sagar VV, Piccone JM. The effect of cimetidine on blood clearance, gastric uptake, and secretion of 99mTc-pertechnetate in dogs. Radiology 1981;139:729-731.
19. Shin JM, Munson K, Vagin O, Sachs G. The gastric HK-ATPase: structure, function, and inhibition. Pflugers Arch 2009;457:609-622. Erratum in: Pflugers Arch 2011;461:399.

Original Article

Mol Imaging Radionucl Ther 2024;33:94-105 *DOI:10.4274/mirt.galenos.2024.34711*

Quantitative Performance Evaluation of Commonly Used Colormaps for Image Display in Myocardial Perfusion Imaging: Analysis based on Perceptual Metrics

Miyokardiyal Perfüzyon Görüntülemede Görüntü Ekranı için Yaygın Olarak Kullanılan Renk Haritalarının Kantitatif Performans Değerlendirmesi: Algısal Metriklere Dayalı Analiz

Mohsen Qutbi

Shahid Beheshti University of Medical Sciences, School of Medicine, Department of Nuclear Medicine, Tehran, Iran

Abstract

Objectives: To quantitatively evaluate the performance of the most used colormaps in image display using perceptual metrics and to what extent these measures are congruent with the true intensity or uptake of pixels at different levels of defect severity in simulated cardiac images.

Methods: Six colormaps, labeled "Gray", "Thermal", "Cool", "CEqual", "Siemens" and "S Pet" extracted from FIJI ImageJ software are included. Colormap data are converted from the red, green, blue color space to CIELAB. Perceptual metrics for measuring "color difference" were calculated, including difference (ΔE^{76}) and "speed". The pairwise color difference in every two levels or entries is visualized in a 2-dimensional "heatmap distance matrix" for each colormap. Curves are plotted for each colormap and compared. In addition, to apply this technique to clinical images, simulated short-axis cardiac slices with incremental defect severity (10% grading) were employed. The circumferential profile curves of true pixel intensity, lightness or luminance, and color difference are plotted simultaneously for each defect severity to visualize the concordance of the three curves in various colormaps.

Results: In 0% defect, all the curves are at the highest level, except for "s pet", in that the lightness is not at its maximum value. In the phantom with 10% defect (or 90% of maximum value), discrepancies among curves appear. In "Siemens", the ΔE^{76} drops sharply. In "Siemens" colormap, the ΔE^{76} drops sharply. In 80% defect, ΔE^{76} curve, in "gray" colormap drops more slowly than other curves of other colormaps. In "s pet", lightness curve rises paradoxically, although the count intensity and ΔE^{76} curve match. In 70% defect, again, the curves are in good agreement in "thermal", "Siemens" and "cequal". However, a consistent lag exists in "gray". Up to 50% defect, curves maintain their expected pattern, but in defects more severe than 40%, lightness and ΔE^{76} curves in "cool" and "cequal" rise paradoxically, and in "thermal", they start to slow down in descent. In "Siemens", falling pattern of the three curves continues. For "s pet" colormap, an erratic pattern of lightness and ΔE^{76} curves exists.

Conclusion: Of 6 colormaps investigated for estimating defect severity, "grayscale" is less favorable than others and "thermal" performs slightly better. "S pet" or rainbow, which is used traditionally by many practitioners, is strongly discouraged. The "Siemens" colormap suffers from decreased discriminating power in the range of mild to moderate/severe. In contrast, the "cool" and "cequal" colormaps outperform the other colormaps employed in this study to some extent, although they have some shortcomings.

Keywords: Colormap, look-up table, performance, perceptual metric, image display, quantitative analysis

Address for Correspondence: Mohsen Qutbi Asst. Prof., Shahid Beheshti University of Medical Sciences, Faculty of Medicine, Department of Nuclear Medicine, Tehran, Iran

Phone: +0982123031250 **E-mail:** mohsen.qutbi@gmail.com, mohsen.qutbi@sbmu.ac.ir ORCID ID: orcid.org/0000-0002-8347-605X

Received: 23.09.2023 **Accepted:** 21.01.2024 **Epub:** 09.02.2024

Öz

Amaç: Görüntü ekranında en çok kullanılan renk haritalarının performansını algısal ölçümler kullanarak niceliksel olarak değerlendirmek ve bu ölçümlerin, simüle edilmiş kardiyak görüntülerdeki farklı defekt şiddeti seviyelerindeki piksellerin gerçek yoğunluğu veya alımıyla ne ölçüde uyumlu olduğunu değerlendirmektir.

Yöntem: Çalışmaya FIJI ImageJ yazılımından çıkarılan "Gri", "Termal", "Soğuk", "CEqual", "Siemens" ve "S Pet" etiketli altı renk haritası dahil edilmiştir. Renk haritası verileri RGB renk uzayından CIELAB'a dönüştürülür. "Renk farkını" ölçmek için "fark" (ΔE^{76}) ve "hız" dahil algısal ölçümler hesaplandı. Her iki seviyedeki veya girişlerdeki ikili renk farkı, her renk haritası için 2 boyutlu bir "ısı haritası uzaklık matrisinde" görselleştirilir. Her renk haritası için eğriler çizilir ve karşılaştırılır. Ek olarak, bu tekniği klinik görüntülere uygulamak için, artan defekt şiddetine (%10 derecelendirme) sahip simüle edilmiş kısa eksenli kalp kesitleri kullanıldı. Gerçek piksel yoğunluğunun, açıklığın veya parlaklığın ve renk farkının çevresel profil eğrileri, çeşitli renk haritalarında üç eğrinin uyumunu görselleştirmek amacıyla her defekt şiddeti için eşzamanlı olarak çizildi.

Bulgular: %0 defektte "s pet" dışında tüm eğriler en yüksek seviyede olup açıklık maksimum değerde değildir. %10 defektli (veya maksimum değerin %90'ı) fantomda eğriler arasında tutarsızlıklar görünür. "Siemens"te ΔE^{76} keskin bir şekilde düşüyor. "Siemens" renk haritasında ΔE^{76} keskin bir şekilde düşüyor. %80 defektte, ΔE^{76} eğrisi, "gri" renk haritasında diğer renk haritalarının diğer eğrilerine göre daha yavaş düşer. "S pet"te, sayım yoğunluğu ve ΔE^{76} eğrisi eşleşse de açıklık eğrisi paradoksal olarak artar. %70 defektte ise yine "termal", "Siemens" ve "cequal" eğriler iyi bir uyum içindedir. Ancak "gri" renkte tutarlı bir gecikme mevcuttur. %50'ye kadar defektte, eğriler beklenen şeklini korur, ancak %40'tan daha şiddetli defektlerde, açıklık ve ΔE^{76} eğrileri "soğuk" ve "cequal"de paradoksal olarak yükselir ve "termal"de alçalırken yavaşlamaya başlar. "Siemens"te üç eğrinin düşme paterni devam eder. "S pet" renk haritası için düzensiz bir açıklık modeli ve ΔE^{76} eğrileri mevcuttur.

Sonuç: Defekt şiddetini tahmin etmek için incelenen 6 renk haritasından "gri tonlamalı" diğerlerine göre daha az avantajlıdır ve "termal" biraz daha iyi performans göstermektedir. Birçok uygulayıcı tarafından geleneksel olarak kullanılan "s pet" veya gökkuşağı kesinlikle önerilmez. "Siemens" renk haritası, hafif ile orta/şiddetli aralığında ayırt edici gücün azalmasından muzdariptir. Buna karşılık "cool" ve "cequal" renk haritaları, bazı eksiklikleri olsa da, bu çalışmada kullanılan diğer renk haritalarından bir dereceye kadar daha iyi performans göstermektedir.

Anahtar kelimeler: Renk haritası, arama tablosu, performans, algısal metrik, görüntü ekranı, niceliksel analiz

Introduction

Image display or visualization is one of the key steps in medical image interpretation after necessary image processing and analysis. In most circumstances, readers apply various combinations of colors to gray-intensity images for various reasons, known as image pseudo-coloring. Visualization is generally enhanced and optimized depending on the purpose and application. Lesion-finding tasks and estimating the level of intensity (for example severity of defects in myocardial perfusion imaging) require the use of different colormaps. The former requires enhancing contrast and maximizing the conspicuity of the area of interest (or lesions), and the latter is based on the input-output relationship between the original data and the displayed image (1,2,3,4). The input-output relationship is related to the intensity transformation of images and is defined as linear or other simple nonlinear mathematical functions (logarithmic or exponential) relating input to output. Except for the direct input-output relationship in the gray colormap, this relationship is non-linear for other colormaps and therefore compromises the estimation of relative intensity. This non-linearity between input and output frequently occurs with multiple-hue colormaps (5,6,7,8). Furthermore, display in two- or three-dimensional modes using different methods of shading and rendering and fusing of images also affects one's judgment (1,9,10). However, based on the application, particular colormaps may be preferred. Furthermore, colormaps that consist of different hues, saturation, and intensity may have a strong effect on the reader's or interpreter's perception. In most cases, medical imaging practitioners use commercially available colormaps embedded in the software by a vendor and it is used because one is accustomed to using it in their interpretation or based on their own prior experience, preference, or convention. Despite this fact, domain-specific colormaps are widely used across various disciplines (3).

Frequently, colormaps are compared subjectively. Therefore, interpretation is subject to biased estimation because of the different interobserver perceptual impacts of colors. Because of the complex multi-faceted nature of the phenomenon of color perception, quantification and measurement are inherently difficult tasks, and the results may not satisfactorily reflect the true psychological consequences (9,11,12,13,14,15,16,17). Owing to the reasons mentioned and difficulties in quantifying the characteristics, specifications, and behavior of different colormaps, few studies have investigated the properties of various colormaps and, more importantly, their implications in clinical settings such as nuclear medicine imaging. Evaluation of colormaps with more quantitative measures facilitates comparison and enables one to choose the right one. In addition, except for grayscale, colors in other colormaps are perceived differently in humans. This issue complicates the problem because using perceptual metrics and assessing colors in various available color spaces are not straightforward. Employing mathematical modeling for the psychophysical and physiological aspects

of different colors and their association in a sequential pattern may be beneficial to some extent. Of the various color spaces available, CIELAB (L*a*b*) and CIELUV are more compliant with human perception of colors with slight differences. In the CIELAB color space, the dominant feature is the perceptually uniform distances between colors. Therefore, the colors in the red, green, blue (RGB) color space can be converted to corresponding ones in the L*a*b* color space to examine the distance of colors in a sequential colormap (2,3,4,18,19). Thus, the evaluation of the compatibility of its pattern with the raw data values of pixels (or counts) in images is feasible. Then, according to the application, one can find the agreement and correlation between them.

The present study aims to quantitatively evaluate the performance of mostly used colormaps in image display and visualization by measures that are considered perceptual metrics. In addition, to examine the extent to which these measures are congruent with the true intensity or uptake of pixels over various values, i.e., different levels of defect severity in simulated cardiac single photon emission computed tomography (SPECT) or positron emission tomography (PET) images.

Materials and Methods

Mathematical Representation and Quantitative Metrics

Mathematically, a colormap is a discrete-valued function that relates the values as input to the corresponding values as output. Discretized input values, because of spatial sampling and quantization, are sorted and then "mapped" to another set of discrete values. For an 8-bit or 256-level colormap function, this process can be expressed mathematically as follows:

$$\begin{cases} F: p_i \rightarrow c_i \\ i \in [1,256]; \end{cases}$$

In this case, index *i* represents the *i* th bin of the image histogram and the one-to-one function, *F*, maps p_i to c_i as elements of domains and codomains. By this means, a distinct color or shade of gray is assigned. For colormaps consisting of a range of color hues, each level or entry is formed by a triple component as channels (R, G, and B representing red, green, and blue). Therefore, c_i equals [c_i (R), c_i(G), c_i(B)]. In gray shades, in contrast, all the values in each triplet are equal (4). To demonstrate the overall characteristics and major features of each colormap, a gray transformation is applied using the following formula (20):

$$g(x,y) = \alpha f(x,y,R) + \beta f(x,y,G) + \gamma f(x,y,B)$$

Where the coefficients, α = 0.2989, β = 0.5870, and γ = 0.1140 are weights according to the perceptual impacts of different wavelengths in humans. *f* is the original image and *g* is the gray-transformed image. The resulting gray intensity is graphed and compared.

Next, for each colormap, a conversion is implemented from the RGB color space to the CIE L*a*b* or CIELAB color space. First, the colormap in RGB space is converted to the corresponding one in XYZ color space, and the XYZ/ L*a*b* transformation is conducted. To accomplish this transformation, a MATLAB built-in algorithm is employed. L* denotes the luminance or lightness and ranges from 0 to 100. Values of 0 and 100 specify black and white in the image. a* and b* indicate the perpendicular coordinate axes in the chromaticity plane. The a* axis determines the amount of red and green hues (in positive and negative directions, respectively). Likewise, the b* axis determines the number of yellow and blue hues (in positive and negative directions, respectively). For graphing, L* is demonstrated as a straight or curved line ranging from 0 to 100 as the target line, and the order of the color components in the colormap is depicted as a path (multiple segmented curved lines) in the a*b* plane.

To compare the impact of colors in neighboring or distant levels in the colormap the pairwise "color difference" is computed by a distance metric in the Euclidean space as follows:

$$\Delta E_{i,j}^{76} = \sqrt{\left(\left(\mathrm{L_j^*} - \mathrm{L_i^*}\right)^2 + \left(\mathrm{a_j^*} - \mathrm{a_i^*}\right)^2 + \left(\mathrm{b_j^*} - \mathrm{b_i^*}\right)^2\right)}$$

$$i, j \in [1,256], i \neq j;$$

In that, ΔE^{76} represents the distance between two colors in CIELAB color space (version 1976). This metric is computed between each possible pair in the colormap. For an 8-bit colormap (256 levels or entries and a range of values from 0 to 255 in each level), a heatmap distance matrix with a size of 256×256 is computed, and the value of ΔE^{76} is visualized as gray intensity at the intersection of the row and column of interest. The higher the value of that element in the matrix (pixel), the brighter the intensity of that pixel. Furthermore, the "speed" of color change between two arbitrary levels in the colormap (levels i and j for example) is calculated using equations (4,21):

$$V_{i,j} = \frac{\Delta E_{i,j}^{76}}{l_i - l_j}$$

$V_{i,j}$ is the speed between two arbitrary levels (I_i and I_j). Therefore, for "local speed" between two successive levels (I_j and I_{j-1}), the equation is as follows:

$$V_{j,j-1} = \Delta E^{76}_{j,j-1}$$

Then, the average, standard deviation, maximum speed, and minimum speed are calculated (4).

Colormaps

In the present study, 15 colormaps were categorized into four groups according to general similarity in hues included (i.e., the sequential pattern of hues and the gray intensity curves), as shown in Figure 1. Six colormaps that are frequently used for applications of medical visualization were enrolled and analyzed. To perform this task, the original files for generating colormaps were extracted from FIJI ImageJ software, which is a Java-based framework for biomedical image processing and analysis developed by the National Institutes of Health (22). The 6 selected colormaps under investigation in this study are "Gray", "Thermal", "Cool", CEqual", "Siemens" and "S Pet". As can be seen in the figure, in the upper panel, the colormaps are presented from the lower bound at the leftmost and the upper bound at the rightmost side of each color bar. The gray intensity values of each colormap are plotted as shown in the lower panel. In category 1, the gray intensity curves of "gray" and "thermal" are fitted to the target line nearly perfectly. There is a consistent linear pattern over the entire spectrum. In category 2, "cool", "cequal", "ge" and "mmc" are present, and the patterns of the gray intensity curves are roughly similar. There is a linear pattern from the mid-range to the upper bound with a steeper than the target line. In the lower half, no consistent relationship exists "cequal" reaches a plateau near the upper bound. In category 3, "Siemens", "hot iron", "warm metal and "fire" are selected. There is an approximately linear pattern from the lower to upper bounds with some irregular fluctuations. Finally, in category 4, "s pet", "rain bow", "a squared", "physics" and "prism" are included. There are wide fluctuations over the entire range of colormaps, which are far from the target line.

These labels are the standard names that are well known by researchers and practitioners in biomedical disciplines, although some differences exist, particularly in non-medical contexts. The files in the format of .lut files are converted to .csv text files and are then imported into MATLAB software for processing and analysis. The file consisted of the values of RGB triples for 256 levels or entries. In each entry, values are in the range [0,255] as integers that indicate the 8-bit format of colormaps. For visualization and analysis, necessary reformatting, transformation, and conversion from RGB to other color spaces are implemented. The scale is preserved as linear in the original data (no logarithmic, exponential, or other custom-function-based transformation is applied).

Cardiac Phantom

A simplistic model of the short axis of the left ventricle (LV) is designed in a 128×128 matrix. Gaussian blurring is then imposed (with σ = 8 pixels). To simulate a perfusion defect, the short-axis phantom is divided into four sectors, including anterior, septal, lateral, and inferior, each 90°. The defect is placed in the anterior sector with a graded

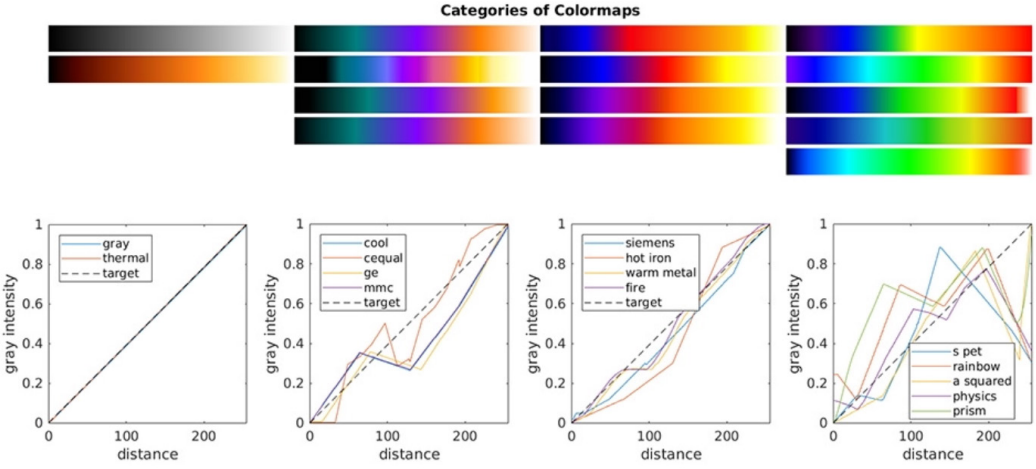

Figure 1. Colormaps are visually presented (upper panel) and the plots of gray intensity (lower panel). In the upper panel, the colormaps are presented from lower bound at the leftmost and the upper bound at the rightmost side of each color bar. The gray intensity values of each colormap are plotted as demonstrated

10-percent increment from no defect (100% of maximal myocardial uptake) to absent uptake (0% of maximal myocardial uptake). In total, 9 phantoms with various levels of defect severity were obtained. This simplistic model is employed because, in cardiac images, the field is limited to the organ of interest (LV).

Tomographic Reconstruction

All phantoms are entered one by one during the process of tomographic reconstruction. Iterative maximum likelihood expectation maximization (MLEM) is used. An acquisition arc of 360° and angular sampling of 3° were set. Collectively, 120 projections were generated during the Radon transform. Then, the generated sinograms are back-projected (inverse Radon transform) to create the tomographic slices. This procedure is repeated 10 times (number of iterations: 10), and in each step, the tomographic slice is updated by dot multiplication of the tomographic slice of the previous iteration to the error image resulting from the element-by-element division of the measured and estimated sinograms. The initial (guess) image is considered to be a uniform one-valued image of the same size as the phantom.

Image Analysis and Plotting

For the analysis of tomographic images, maximum normalization is applied. Thus, the maximum value in each tomographic slice is set to one. This process is performed to ensure the comparability of images and curves and to avoid possible normalization errors. To visually assess the tomographic images and defects, they are displayed side-by-side using 6 colormaps introduced previously. Each slice with a known perfusion defect in the anterior sector (or wall) is profiled by a vertical line crossing the anterior and inferior walls. The intensity profile is then plotted. To plot the circumferential intensity profile of the myocardium, 16 samples (non-uniformly dispersed spatially in the left and right half of the LV) were selected. Hence, the radial profile of the walls is fitted to a Gaussian curve, and the sample points are chosen such that they reside in the maximum or peak of the radial profile. Then, the real count or intensity profile curve is drawn. In addition, for each colormap and each defect severity, the lightness of the luminance curve and the ΔE^{76} curve (as discussed before) are plotted for those sample points.

Implementation and Coding

Codes for designing phantoms, image acquisition, iterative tomographic reconstruction, and image analysis are written in the MATLAB programing language and run in MATLAB software (The MathWorks Inc., version 2021b). The colormap files (or lookup tables as .lut text file formats) are extracted from FIJI ImageJ software.

Results

In Figure 2, the heatmap Euclidean distance matrix is visualized for 6 colormaps selected for more in-depth analysis. The entire range of the colormap is displayed at

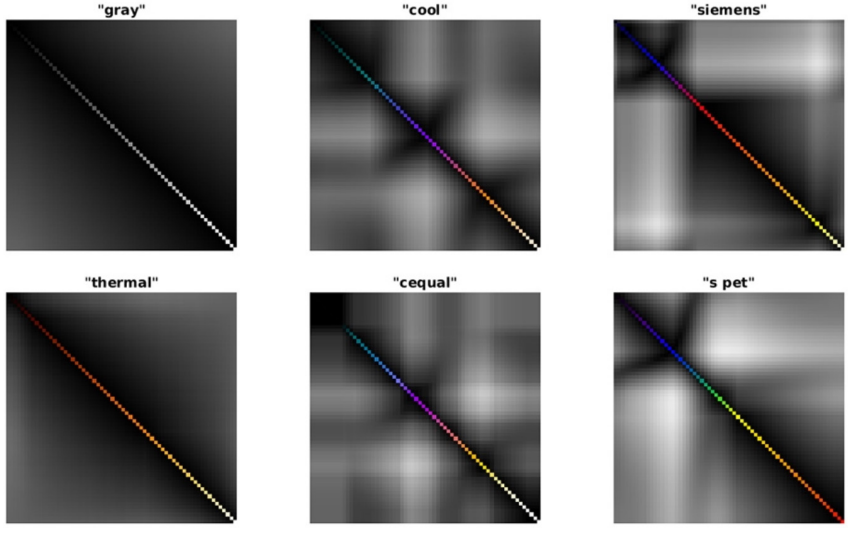

Figure 2. Heatmap Euclidean distance matrices for 6 colormaps are presented. Each panel corresponds to a colormap (here, 6 colormaps). The colormap is displayed in the main diagonal of the matrix, from lower to upper bounds of colormap starting from the left top corner of the matrix to the right bottom corner respectively. The distance between each two pairs of levels or entries (i.e., color hue or shades of gray) is displayed as a shade of gray. The more the distance between two arbitrary pairs on the main diagonal of the matrix, the higher the intensity of the corresponding pixel (which is located at the intersection of the row and column of those pairs)

the main diagonal of the matrix, and the distance between each pair of levels or entries (i.e., color hue or shades of gray) is displayed as a shade of gray. The greater the distance between two arbitrary pairs on the main diagonal of the matrix, the higher the intensity of the corresponding pixel (which is located at the intersection of the row and column of those pairs). As can be seen in the "gray" colormap, the maximum distance is between the lower and upper bounds, as expected. The distance between neighboring pairs (that are close to each other) is too small to be recognized (barely distinguishable) by the human eye. In addition, there is a consistent pattern of distance over the entire range. In "thermal" colormap, an almost similar pattern exists with the exception that the distance between the lower and upper bounds is more prominent than "gray" colormap. In other words, the distance between each pair is augmented in "thermal" compared to "gray". In other colormaps, "cool", "Siemens", "cequal" and "s pet", no regular pattern is visible. In "cool" colormap, the highest distance between pairs is in the mid-range of the map. The largest distance is between the orange and blue pixels. In the upper third of the spectrum, the distance is minimal. An almost similar pattern is evident in "cequal". In "Siemens", the lower third (blue pixels) is remarkably distant from the upper two-thirds (red-orange-yellow pixels), but the pixels in the upper two-thirds of the spectrum are minimally distant. In "s pet" the greatest distance is between the lower and middle thirds (blue pixels and green-yellow pixels).

The curves of lightness or L* in the CIELAB color space and ΔE^{76} for 6 colormaps are provided in Figure 3 and Figure 4, respectively. As demonstrated in Figure 3, the y-axis and x-axis denote the absolute value of lightness in the CLELAB color space and the levels or entries from 1 to 256. The mid-value (50% of myocardial uptake) is indicated by a vertical green line in bold and splits the graph into two parts (lower half and upper half). The curves of "gray" and "thermal" are straight lines almost fitted to the target line. The curve of "Siemens" follows the target line to a high extent. The curve of "s pet" is far deviated from the target line. In the upper half (myocardial uptake in the defect 50% to 100% of maximal myocardial uptake), the curves of "cool" and "cequal" rise almost linearly, but in the lower half, an irregular pattern is evident. In the upper half of the graph (>50%), the steepest line is for "cool" but for "gray", "thermal" and "Siemens", the slope is lower and equals that of the target line. The curve for "s pet" is reversed. In Figure 4, the y-axis and x-axis denote the absolute value of the color difference in the CLELAB color space and the levels or entries from 1 to 256. The mid-value (50% of myocardial uptake) is indicated by a vertical green line in bold and splits the graph into two parts (lower half and upper half). Here, the ΔE^{76} is the difference between the color in the uppermost bound and the color of an arbitrary level so that the value in the rightmost part of the x-axis ends in 0. For "gray" spectrum, the ΔE^{76} curve is a straight line starting from max at level 1 to 0 at level 256. In "thermal" colormap, the curve plateaus in the first half (<50%) and gradually falls in the upper half (>50%). The curves of "cool" and "cequal" colormaps are similar in pattern, but the output range is wider compared to "thermal" (0-100 for "thermal and 0-140 for "cool" and "cequal"). In the upper half, the curves are almost a straight line with a notch in the mid-way (about 75% of maximal uptake or 25% defect severity). The ΔE^{76} curve for "Siemens" shows an irregular pattern in the lower half and remains steady in the upper half before a sharp decline at the end of the

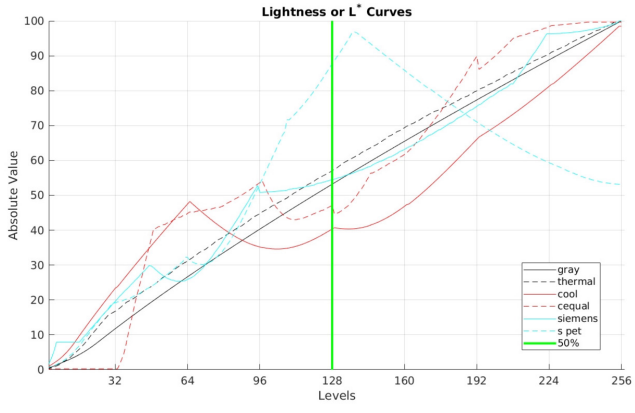

Figure 3. Lightness or L* curves. The y-axis and x-axis denote the absolute value of lightness in CLELAB color space and the levels or entries from 1 to 256. The mid-value (50% of myocardial uptake) is indicated by a vertical green line in bold and splits the graph into two parts (lower half and upper half)

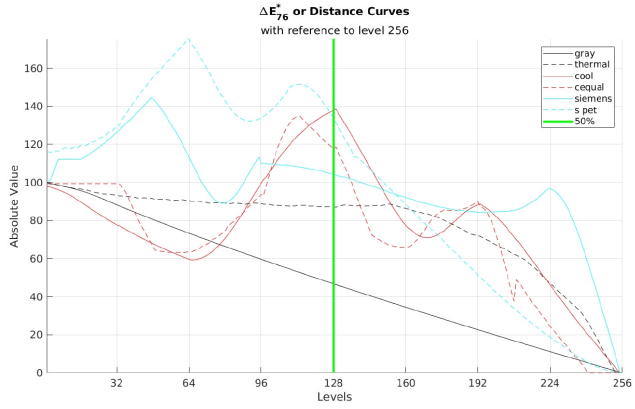

Figure 4. ΔE^{76} curves for the 6 colormaps. The y-axis and x-axis denote the absolute value of color difference in CLELAB color space and the levels or entries from 1 to 256. The mid-value (50% of myocardial uptake) is indicated by a vertical green line in bold and splits the graph into two parts (lower half and upper half)

range. The curve is plateau at a wide range in the middle. A similar scenario is for "s pet" in the lower half but falls in a linear pattern in the upper half.

The local speed and its statistical measures for each colormap are shown in Figures 5, 6. In Figure 5, the blue line indicates the original data, and the red curve in bold indicates the smoothed data. For "gray", the speed is high in the leftmost part of the range but uniformly decreases then. In absolute terms, the changes in speed are profoundly low compared with those of other colormaps. In "thermal", the speed is remarkably high in the rightmost and leftmost parts of the range. For "cool" and "cequal" colormaps, the speed is minimum in the upper and lower zones of the range, but in the middle, it demonstrates several peaks. For "Siemens", the speed curve is irregular over its entire range. Finally, the speed is uniform in the upper half and peaks sharply.

The tomographic slices reconstructed using the iterative MLEM method with graded defect severity are displayed in Figure 7. Each row is dedicated to one colormap. The incremental defect severity of the anterior wall was calculated as the percentage of maximal myocardial uptake (100% means no defect and 0% means no uptake). Here, the defects based on the color that appears to the

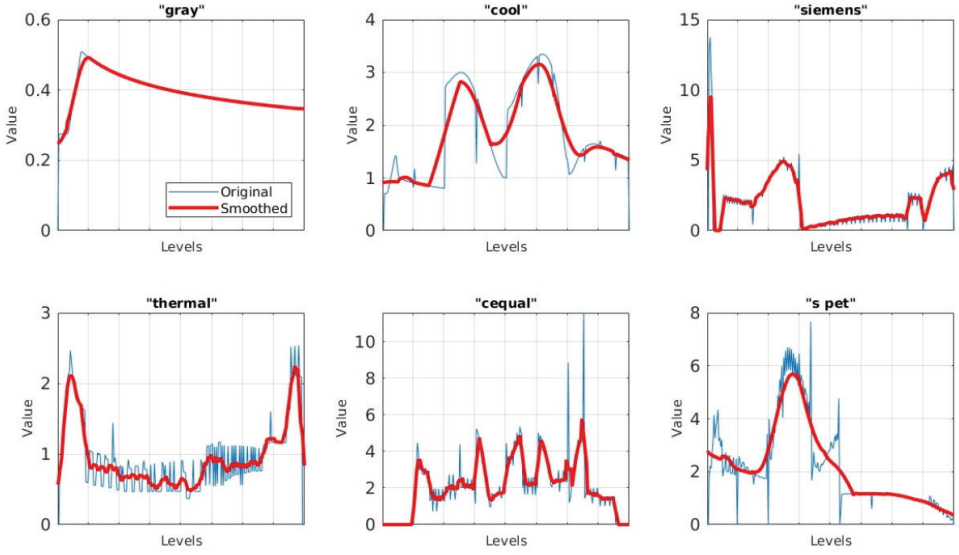

Figure 5. The local speed is displayed for each colormap. The blue line indicates the original data and the red curve in bold in the smoothed data

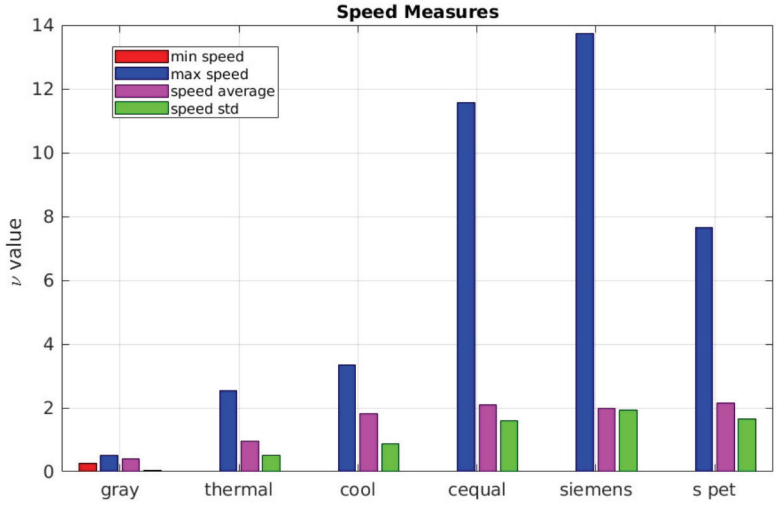

Figure 6. The statistical measures of speed including maximum and minimum values as well as the mean (average) and standard deviation is plotted in the bar chart. As can be seen, those measures are small for "gray" and "thermal", but, for other colormaps, the variation in the speed is remarkable

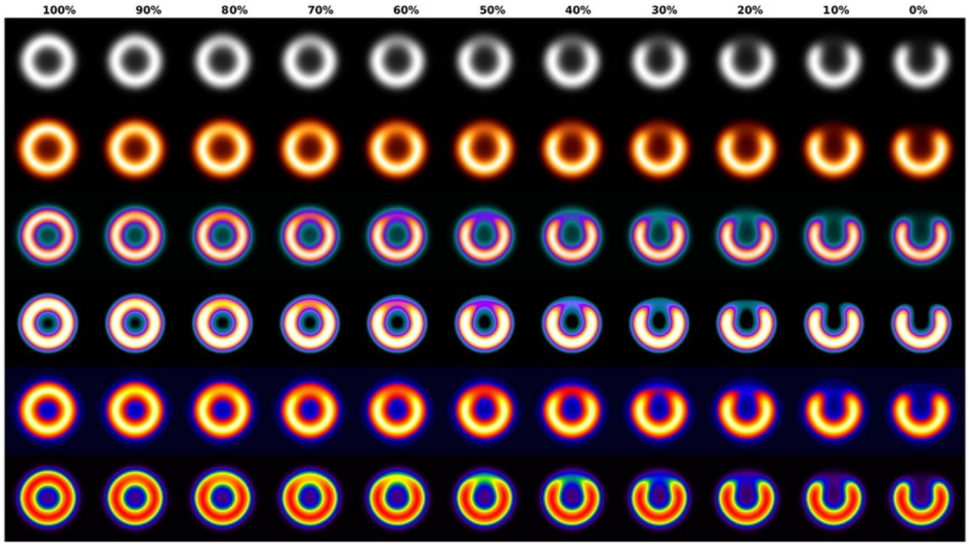

Figure 7. The tomographic slices reconstructed by iterative MLEM method with graded defect severity (100% to 0% myocardial activity). In each row, the images are visualized with one of 6 colormaps. The defect is located on the anterior wall

MLEM: Maximum likelihood expectation maximization

reader's eye are to a high extent subjective, and readers, based on their own experience and perception, decide to estimate the severity of the defect. Although this way of interpretation constitutes the main part of decision making in clinical settings, it seems that approximately noticeable differences exist among different colormaps. In "gray" and "thermal" colormaps, defects seem to the reader's eye to change more slowly than other colormaps, "cool", "cequal" and "s pet" in particular. In other words, the perceptual impact of changes is dramatic, in close agreement with the results shown in Figures 2, 4.

To make the results more objective, the colormaps were analyzed with more quantitative metrics. For this task, certain sample points are selected on the tomographic slice of the cardiac phantom (Figure 8), and the values of those pixels are analyzed in terms of relative count or intensity, lightness or luminance and the ΔE^{76}. Figure 9A, B, C, D, E, F consists of 6 parts according to defect severity from 100% uptake (or no defect) to 50% of maximal uptake. The circumferential profiles of intensity or count, lightness and ΔE^{76} curve are plotted for various levels of defect severity. Thus, the three curves are comparable for each defect severity. In each part, the upper panel displays the tomographic image with its specific defect severity in six colormaps, and in the lower panel, the curves of count, lightness and ΔE^{76} are plotted. In each plot, the profile starts from the inferior wall and then through the septum reaches the anterior wall (which is defective). Subsequently, by passing through the lateral wall reaches a similar point in the inferior wall. Thus, the defect is in the mid-profile. Each plot has three curves. The black curve denotes the true value of the sample points (or counts), and the red and cyan curves indicate lightness (L*) and ΔE^{76}. When there is

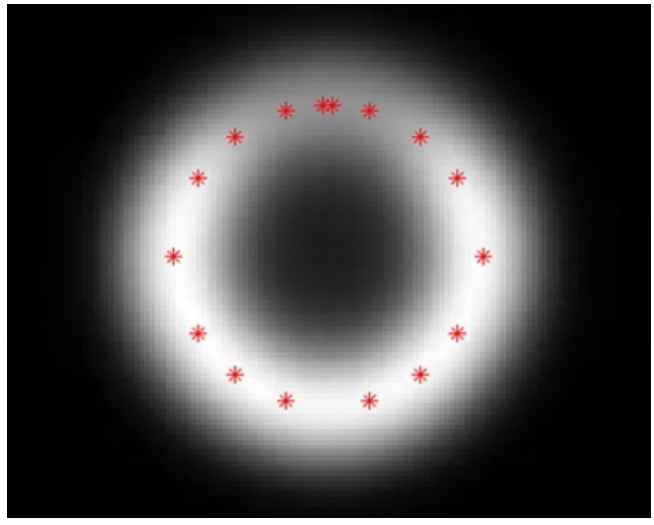

Figure 8. A tomographic slice with a defect on the anterior wall. The sample points are placed on the peak myocardial uptake radially. Sample points are dispersed symmetrically, closer to the anterior wall. It starts from inferior wall going through the septum, then anterior wall (the defect) and through lateral wall it ends in inferior wall to plot the circumferential profile of the short axis slice of the LV

LV: Left ventricle

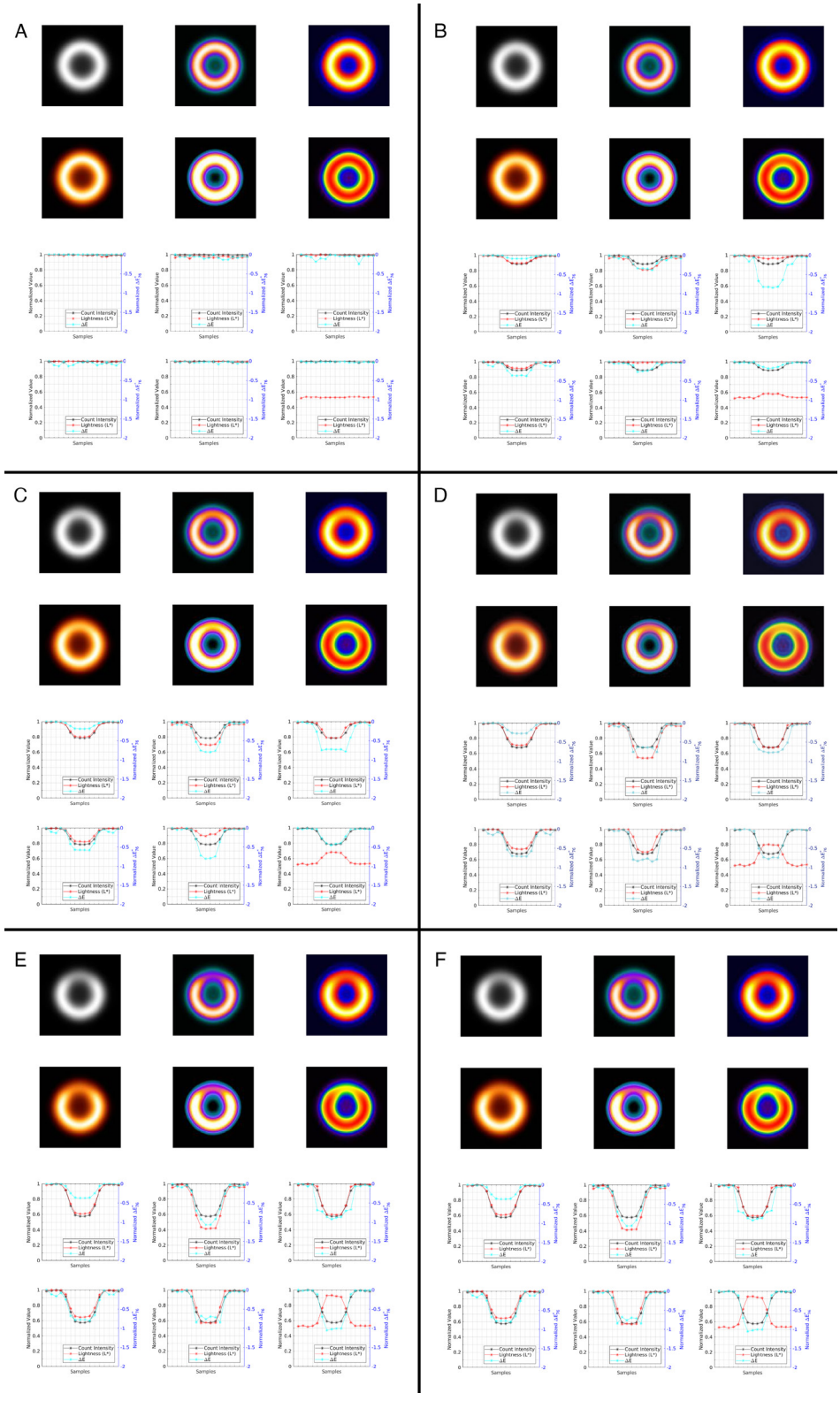

Figure 9. Tomographic slices and circumferential profiles of intensity or count, lightness, and ΔE^{76} are plotted for various levels of defect severity as 0% (A), 10% (B), 20% (C), 30% (D), 40% (E) and 50% (F)

no defect, all the curves are at the highest level (equals 1 or 100%), except for "s pet", in that the lightness is not at its maximum value. In the phantom with 10% defect (or 90% of maximum value), discrepancies among curves appear. In "Siemens" colormap, the ΔE^{76} drops sharply. This pattern is concordant with the way it appears to the eye. In 80% defect, ΔE^{76} curve, in "gray" colormap drops more slowly than other curves of other colormaps. Instead, the defect is more noticeable in "cool", "Siemens" and "cequal". In "s pet" colormap, the lightness curve rises paradoxically although the count intensity and ΔE^{76} curves are matching. In 70% defect, again, the curves are in good agreement in "thermal", "Siemens" and "cequal". However, a consistent lag exists in "gray" colormap. Up to 50% defects, the curves maintain their expected pattern, but in defects more severe than 40%, lightness and ΔE^{76} curves in "cool" and "cequal" rise paradoxically, and in "thermal" they start to slow down in descent. In "Siemens", the falling pattern of the three curves continues. For "s pet" colormap, an erratic pattern of lightness and ΔE^{76} curves exists.

Discussion

Colormaps have long been used for color coding of inherently gray-intensity images. Broadly speaking, they are generally employed for scientific data visualization. The process of pseudo-coloring, apart from its aesthetical purposes, seeks ways to facilitate the conveyance of information qualitatively and semi-quantitatively (1,2,3,4). For this reason, many colormaps have been designed, some of which are frequently used in medical imaging. In nuclear medicine, in particular, a few colormaps including "grayscale", "inverted gray", "thermal", "cool", "Siemens", and traditionally, "rainbow" or "s pet" are of high interest among practitioners in this field (23,24,25). In other words, these colormaps are specific to this particular domain and are mostly used based on convention, convenience, accessibility, etc. Few studies have investigated the effect of using colormaps in clinical images. As mentioned before, the inherently complex and multi-aspect nature of the assessment of colors and the difficulty in devising accurate methods for quantification and modeling preclude much investigation on this topic.

Colors are mathematically modeled using several color spaces and particular measures. Of the several color models, CIELAB, developed by the Commission Internationale de l'Eclairage, is considered the most perceptually uniform. The model comprises a pyramidal geometry. The vertical axis indicates lightness, and the horizontal plane includes a coordinate system with a- and b-axes. The a-axis ranges the colors between red and green on the positive and negative sides, respectively. The b-axis includes colors between blue and yellow on the negative and positive sides. The colors of points that reside in the origin or on the lightness axis are a shade of gray between black and white. Distances between two colors (or points) are calculated in Euclidean space, as mentioned in the methods section. The main application of this color space is to create perceptually uniform colormaps. However, the related measures are employed as perceptual metrics. ΔE^{76} is the first ever metric introduced in 1976 (4,20,21). This study was intended as a preliminary investigation for characterizing and specifying various colormaps and demonstrating their advantages and pitfalls. In cardiac SPECT and PET images, the colormaps are generally used to categorize the level of uptake or defect severity as well as the changes from one image to another corresponding image (for example, in comparing stress and rest images, termed as reversibility, or in serial imaging) (9,24,26). Therefore, the performance of colormaps in each of these applications can impact the process of decision making. Since there is not much knowledge and understanding about the precise performance of each image, it is expected that the interpretation of such images is highly subject to errors. More prevalently, readers are not fully aware of the advantages and disadvantages and of where to use each one based on the application. Considering all these facts, we intended to analyze their performance quantitatively as much as possible. This warrant consistent objectivity in our comparative evaluation.

There are no perfect colormaps that are applicable to various purposes. Therefore, according to the basic characteristics and specifications of a colormap, the selection should be made. The performance of colormaps is assessed using several metrics, including distance, speed, linearity, uniformity, discriminative power, order, and smoothness (4,20,21). Unfortunately, there is no unanimously accepted nomenclature for these attributes and measures. This issue creates some ambiguities when comparing the colormaps. Despite this fact, we tried to use measures that are more clarified in definition, such as distance and speed. Heatmap Euclidean distance matrix is an easy-to-use method for visualizing pairwise distance between every two colors in the colormap at a glance. Because the distance is based on its perceptual impact, colormaps with softer fluctuations or variations are more desirable. This fact defines the property of uniformity and smoothness measured by local speed (the speed between the colors of two neighboring levels in colormap. Uniformity can be evaluated on the basis of statistical parameters, including standard deviation. According to our findings in Figure 3, "gray" and "thermal" colormaps are perfectly linear. After that, "Siemens", "cool" and "cequal" come. In this respect, "s pet" colormap is far

from a linear property. Now, the question that arises here is which one is important, whole-range or partial-range linearity. The answer, to the best of our knowledge, lies in the application. Since in cardiac SPECT and PET images, the defects with a severity from 0% to 50% are much more of interest, the upper half of the range of the colormaps are of greatest importance (levels from 128 to 256). In semi-quantitative analysis, the grading of defect severity is as follows: mild 10%-25%, moderate 25%-50%, and severe >50% reduction in count compared with maximal myocardial uptake or equivalent semi-quantitative scores of 1, 2, and 3, respectively (26,27). Thus, mild, moderate, and severe lesions are distinguishable. Although "gray", "thermal" and "Siemens" as well as "cool" and "cequal" are all linear in the upper half, the slope of the curves of "cool" and "cequal" is steeper. This leads to higher and more accentuated discrimination or power. In technical terms, "cool" and "cequal" colormaps inherently have an effect similar to that of an exponential function during intensity transformation or a wider dynamic range. This can result in more distinguishing ability. In summary, the whole-range linearity of "gray" and "thermal" does not seem to be an advantage for the analysis of cardiac SPECT and PET images, in contrast to the common belief. It may be of more benefit in other applications because of maintaining whole-range linearity. In the figures, the upper and lower halves are separated by a green vertical line, which indicates 50% of the maximal myocardial uptake. For a more in-depth analysis, the distance is computed using the perceptual metric, ΔE^{76}. The distance, as shown in Figure 4, is calculated based on the color of the maximal value or level 256 in the colormap as a reference. Therefore, the distance between all other levels with level 256 is plotted. Likewise, the output of the upper half in "gray" colormap ranges from 0 to 50 compared to "thermal" colormap, which ranges from 0 to 100, and is steeper in the uppermost sub-range. This finding also provides a more distinguishing ability or discriminative power to categorize lesions as mild or moderate. The results are even better for "cool" and "cequal". In "Siemens", the distance curve is remarkably steep at the rightmost sub-range, enabling the distinction of mild lesions from normal uptake. The findings presented in Figure 5 confirm these results. The speed in "gray" is too low (in the range of 0.2 to 0.5) to distinguish levels from each other. Considering this property, "cool", "cequal" and "thermal" are more favorable compared to other colormaps.

In the next section of this project, the above analysis is performed on simulated cardiac images, which are displayed using the six colormaps. To accomplish this goal, a cardiac phantom with various graded levels of defect severity in the anterior wall was designed, and the respective color differences between normal walls with defects were qualitatively or visually analyzed (Figure 7). This graded defect severity with its color appearance in various colormaps enables readers to make a consistent qualitative assessment. In addition, the circumferential profile of the myocardial walls in the short-axis section is plotted for true pixel intensity or count, changes in the lightness of colors, and color distance as the main perceptual metric. The profile is drawn from samples with the highest myocardial intensity in the radial direction. The order for plotting is from inferior, septal, anterior, lateral, and then inferior walls, so that, at the defect region, the three curves may overlap or separate from each other congruently or incongruently. Thus, one can evaluate the effect of each colormap in the perception and estimation of defect severity. As expected, some underestimate the defects, which means that the curves for lightness and color difference (ΔE^{76}) may fall behind the intensity or uptake curve. It is worth noting that this lag occurs at different levels as the grade of defect severity increases. In contrast, others may overestimate the defects, which can be interpretable as the curves for lightness and color difference ΔE^{76} rush into the lead or get ahead. As an example (Figure 9), in "gray" colormap, the curve for ΔE^{76} always lags the other two curves. Therefore, there is a consistent underestimation, but the pattern is uniform over the entire range of defect severity. In "thermal" colormap, the curves of ΔE^{76} and lightness and uptake run at the same pace. This pattern is more favorable than that of "gray", but the output intensity accentuation is less than that of other colormaps, which means that it lacks enhanced discrimination between mild, moderate, and severe defects. The "cool" and "cequal" colormaps have a favorable effect on readers. However, in "cequal" colormap, the distinction between normal and mild defects is so small that the curve of lightness reaches a plateau. In "Siemens" colormap, the defect is markedly overestimated at first (a large gap between ΔE^{76} and uptake curve) but remains steady after that. It is interpretable as the distinction between mild and moderate/severe defects becomes vague. Finally, for "s pet" color map, the curves for ΔE^{76} and lightness change irregularly, which hampers the accurate estimation of defect severity. Therefore, its use in the interpretation of cardiac SPECT and PET images is strongly discouraged.

This project focuses on a particular technical aspect of color perception, namely color difference, with quantitative metrics. The process of perception itself is much more complicated and involves neurophysiological and psychophysical aspects. Despite the quantifications based on these methods, human perceptions are different

among individuals. In parallel, the issue can be investigated by observer performance models using receiver operating characteristic curve analysis among different readers or observers. However, all these methods are complementary for modeling and quantitative evaluation of human perception of colors and lesion detection (15,16,28).

Conclusion

There certainly is not a perfect colormap for various purposes of image visualization. Selection depends on the application. Of the 6 colormaps investigated in this study for estimating defect severity, "grayscale" is less favorable than others, and "thermal" performs slightly better. The "s pet" or rainbow, which is traditionally used by many practitioners, is strongly discouraged. The "Siemens" colormap suffers from decreased discriminating power in the range of mild to moderate/severe defects. In contrast, the "cool" and "cequal" colormaps outperform the other colormaps employed in this study to some extent, although they have some shortcomings.

Ethics

Ethics Committee Approval: Not necessary.

Informed Consent: Not necessary.

Financial Disclosure: The author declared that this study received no financial support.

References

1. Silva S, Sousa Santos B, Madeira J. Using color in visualization: A survey. Comput Graph 2011;35:320-333.
2. Stone MC. Representing colors as three numbers. IEEE Comput Graph Appl 2005;25:78-85.
3. Zhou L, Hansen CD. A Survey of Colormaps in Visualization. IEEE Trans Vis Comput Graph 2016;22:2051-2069.
4. Bujack R, Turton TL, Samsel F, Ware C, Rogers DH, Ahrens J. The Good, the Bad, and the Ugly: A Theoretical Framework for the Assessment of Continuous Colormaps. IEEE Trans Vis Comput Graph 2018;24:923-933.
5. Rogowitz BE, Treinish LA. How not to lie with visualization. Comput Phys 1996;10:268-273.
6. Candell-Riera J, Santana-Boado C, Bermejo B, Armadans L, Castell J, Casáns I, Jurado J, Magriñá J, de la Rosa JN. Interhospital observer agreement in interpretation of exercise myocardial Tc-99m tetrofosmin SPECT studies. J Nucl Cardiol 2001;8:49-57.
7. Hansen CL. Digital image processing for clinicians, part I: Basics of image formation. J Nucl Cardiol 2002;9:343-349.
8. Siennicki J, Kuśmierek J, Kovacevic-Kuśmierek K, Bieńkiewicz M, Chiżyński K, Płachcińska A. The effect of image translation table on diagnostic efficacy of myocardial perfusion SPECT studies. Nucl Med Rev Cent East Eur 2010;13:64-69.
9. Cooke CD, Vansant JP, Krawczynska EG, Faber TL, Garcia EV. Clinical validation of three-dimensional color-modulated displays of myocardial perfusion. J Nucl Cardiol 1997;4:108-116.
10. Kamei R, Watanabe Y, Sagiyama K, Isoda T, Togao O, Honda H. Optimal monochromatic color combinations for fusion imaging of FDG-PET and diffusion-weighted MR images. Ann Nucl Med 2018;32:437-445.
11. Kimpe T, Tuytschaever T. Increasing the number of gray shades in medical display systems–how much is enough? J Digit Imaging 2007;20:422-432.
12. Geissbuehler M, Lasser T. How to display data by color schemes compatible with red-green color perception deficiencies. Opt Express 2013;21:9862-9874.
13. Race AM, Bunch J. Optimisation of colour schemes to accurately display mass spectrometry imaging data based on human colour perception. Anal Bioanal Chem 2015;407:2047-2054.
14. Uemura M, Asai Y, Yamaguchi M, Fujita H, Shintani Y, Sanada S. Psychophysical evaluation of calibration curve for diagnostic LCD monitor. Radiat Med 2006;24:653-658.
15. Krupinski EA. The role of perception in imaging: past and future. Semin Nucl Med 2011;41:392-400.
16. Burgess AE. Visual perception studies and observer models in medical imaging. Semin Nucl Med 2011;41:419-436.
17. Emery KJ, Volbrecht VJ, Peterzell DH, Webster MA. Variations in normal color vision. VI. Factors underlying individual differences in hue scaling and their implications for models of color appearance. Vision Res 2017;141:51-65.
18. Sharma G. Digital color imaging handbook 2017;6:1-797.
19. MacDonald LW. Using color effectively in computer graphics. IEEE Comput Graph Appl 1999;19:20-35.
20. Representation. In: Solomon C, Breckon T. Fundamentals of digital image processing: a practical approach with examples in matlab. Oxford: John Wiley & Sons, Ltd 2011;12.
21. Color image processing. In: Gonzalez RC, Woods RE. Digital image processing. 3rd Ed. New Jersey: Pearson Education, Inc. 2008;394-460.
22. Schneider CA, Rasband WS, Eliceiri KW. NIH Image to ImageJ: 25 years of image analysis. Nat Methods 2012;9:671-675.
23. Travin MI. Pitfalls and Limitations of Radionuclide and Hybrid Cardiac Imaging. Semin Nucl Med 2015;45:392-410.
24. Hansen CL. The role of the translation table in cardiac image display. J Nucl Cardiol 2006;13:571-575.
25. Peace RA, Lloyd JJ. Comment on "The role of the translation table in cardiac image display". J Nucl Cardiol 2007;14:134; author reply 134-135.
26. Dorbala S, Ananthasubramaniam K, Armstrong IS, Chareonthaitawee P, DePuey EG, Einstein AJ, Gropler RJ, Holly TA, Mahmarian JJ, Park MA, Polk DM, Russell R 3rd, Slomka PJ, Thompson RC, Wells RG. Single Photon Emission Computed Tomography (SPECT) Myocardial Perfusion Imaging Guidelines: Instrumentation, Acquisition, Processing, and Interpretation. J Nucl Cardiol 2018;25:1784-1846.
27. Tilkemeier PL, Bourque J, Doukky R, Sanghani R, Weinberg RL. ASNC imaging guidelines for nuclear cardiology procedures: Standardized reporting of nuclear cardiology procedures. J Nucl Cardiol 2017;24:2064-2128.
28. Chakraborty DP. New developments in observer performance methodology in medical imaging. Semin Nucl Med 2011;41:401-418.

Interesting Image

Mol Imaging Radionucl Ther 2024;33:106-108 *DOI:10.4274/mirt.galenos.2023.58224*

Unusual Soft Tissue Uptake of Tc-99m MDP in Radiation-induced Sarcoma: Diagnostic Conundrum

Radyasyona Bağlı Sarkomda Yumuşak Dokuda Beklenmedik Tc-99m MDP Tutulumu: Tanısal İkilem

Sharjeel Usmani[1], Anjali Jain[1], Khulood Al Riyami[1], Zahida Niaz[2], Subhash Kheruka[1], Vipin V Jayakrishnan[1]

[1]Sultan Qaboos Comprehensive Cancer Care and Research Center, Department of Radiology and Nuclear Medicine, Muscat, Oman
[2]Sultan Qaboos Comprehensive Cancer Care and Research Center, Department of Pathology, Muscat, Oman

Abstract

Tc-99m methylene diphosphonate (MDP) is a bone imaging agent used for skeletal staging, but it can also be localized in extraosseous calcifying lesions. We report a case of an 84-year-old woman with breast carcinoma who underwent surgery followed by radiotherapy 10 years ago and now presented with a right axillary mass referred for Tc-99m MDP to exclude bone metastasis. Tc-99m MDP shows intense tracer uptake in the right thoracic region corresponding to the site of calcified soft tissue mass in the right lateral chest wall. Subsequent ultrasonography revealed an ill-defined lesion containing coarse calcifications. Biopsy showed radiation-induced sarcoma. Extra osseous Tc-99m MDP uptake may provide important diagnostic information that may alter patient management.

Keywords: Tc-99m MDP bone scan, extraosseous uptake, radiation-induced sarcoma, breast cancer

Öz

Tc-99m metilen difosfonat (MDP), iskelet evrelemesi için kullanılan bir kemik görüntüleme ajanıdır, ancak aynı zamanda kemik dışı kalsifiye lezyonlarda da lokalize edilebilir. Bu olgu sunumunda, sağ koltuk altı kitlesi ile başvuran ve kemik metastazını dışlamak için Tc-99m MDP'ye yönlendirilen, 10 yıl önce ameliyat olan ve ardından radyoterapi gören 84 yaşında meme karsinomlu bir kadın hastayı sunuyoruz. Tc-99m MDP, sağ yan göğüs duvarındaki kalsifiye yumuşak doku kitlesinin bulunduğu bölgeye karşılık gelen sağ torasik bölgede yoğun izleyici tutulumunu göstermektedir. Daha sonraki ultrasonografide kaba kalsifikasyonlar içeren, iyi tanımlanamayan bir lezyon saptanmıştır. Biyopsi radyasyonun neden olduğu sarkomu göstermiştir. Ekstra kemik Tc-99m MDP tutulumu, hasta yönetimini değiştirebilecek önemli tanısal bilgiler sağlayabilir.

Anahtar kelimeler: Tc-99m MDP kemik taraması, kemik dışı tutulum, radyasyona bağlı sarkom, meme kanseri

Address for Correspondence: Sharjeel Usmani MD, Sultan Qaboos Comprehensive Cancer Care and Research Center, Department of Radiology and Nuclear Medicine, Muscat, Oman
Phone: +96893219764 **E-mail:** dr_shajji@yahoo.com ORCID ID: orcid.org/0000-0001-9274-7571
Received: 07.08.2023 **Accepted:** 05.11.2023 **Epub:** 19.02.2024

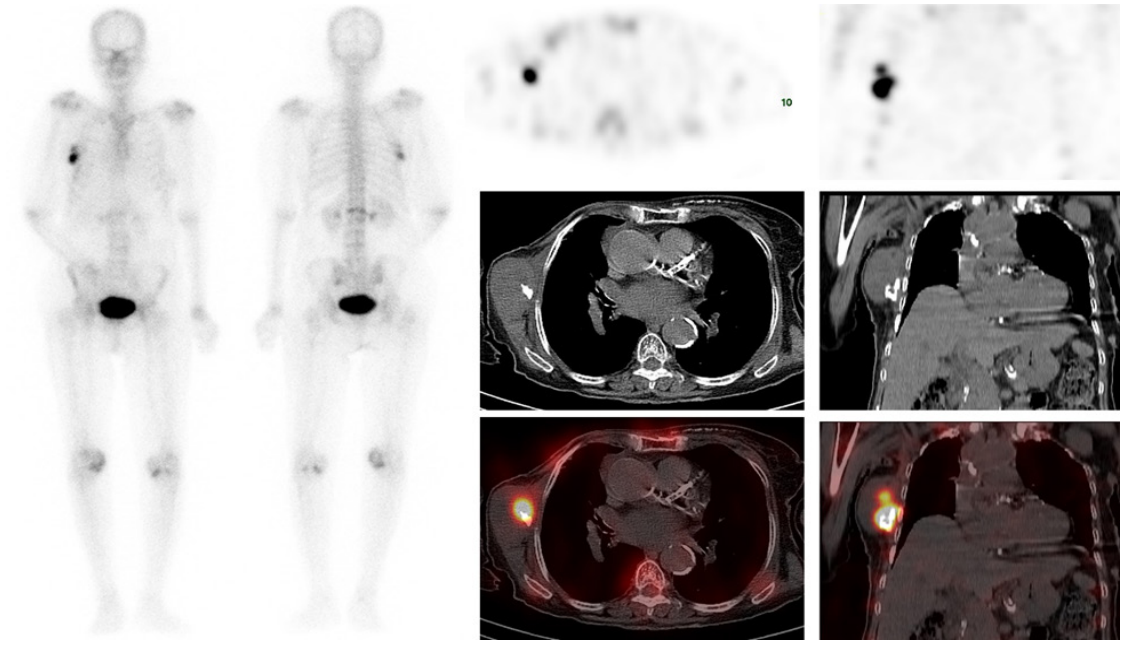

Figure 1. An 84-year-old female with a known case of right breast cancer who underwent surgery followed by radiotherapy 10 years ago and now presented with a right axillary mass. The patient was referred for Tc-99m methylene diphosphonate (MDP) bone scan to rule out bone metastasis. The bone scan shows intense tracer uptake in the right thoracic region corresponding to the site of the calcified soft tissue mass in the right chest wall. Linearly increased tracer uptake is also seen in the L1 vertebra at the site of partial collapse. No evidence of bone secondaries. Ultrasonography showing a solid mass along the right lateral chest wall with ill-defined borders containing coarse calcifications and internal vascularity.

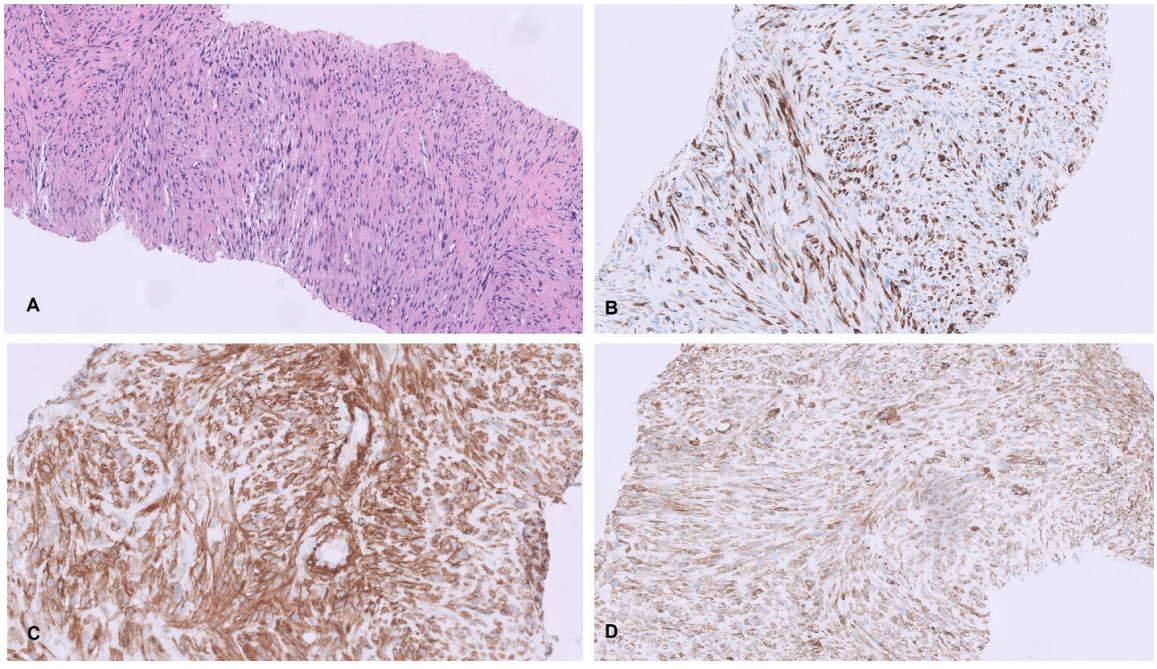

Figure 2. Biopsy of the calcified soft tissue mass showing malignant spindle cell tumor with hyperchromatic nuclei on H&E (A). (B-D) Immunostains demonstrate that the tumor cells are immunoreactive with smooth muscle cell differentiation antibodies desmin (B), smooth muscle actin (C), and H-caldesmon (D). Given the localization of the tumor not in the breast parenchyma and the fact that the patient received radiotherapy at the site of the tumor almost 10 years ago and no history of malignant phyllodes and metaplastic carcinoma, the histological features and the immunoprofile conform to radiotherapy-induced leiomyosarcoma in clinical settings.

Radiation-induced sarcoma (RIS) is a rare type of cancer that develops in the radiation field of a previous radiation therapy treatment. It is a long-term complication of radiation therapy that typically occurs years after the initial treatment (1). The exact mechanisms underlying the development of RISs are not fully understood. However, radiation exposure can cause genetic mutations or damage to DNA within normal cells, leading to the development of cancerous cells over time. The incidence rates of RISs in breast cancer patients typically range from 0.03% to 0.3% (3 to 30 cases per 10,000 patients) over a period of 10 to 20 years following radiation therapy (2). One study reported a cumulative incidence of 0.07% 5 years after irradiation, 0.27% at 10 years, and 0.48% at 15 years; the 5-year survival rate was 36% (3).

Tc-99m MDP is a bone imaging agent used for skeletal staging, but it can also be localized in extraosseous calcifying lesions. The reported mechanisms include (a) local tissue necrosis or damage leading to increased calcium deposition in the tissue, (b) hyperemia, (c) altered capillary permeability, (d) adsorption onto tissue calcium, (e) presence of iron deposits, and (f) binding to enzyme receptors or denatured proteins (4,5). Significantly increased MDP uptake by extraosseous soft tissue tumors is associated with poor differentiation in both children and adults (6). Extra-osseous tracer uptake is common on Tc-99m MDP, and these non-osseous findings may occasionally alter diagnosis and subsequent management. In hybrid imaging, anatomical localization with computed tomography often improves both the specificity of assessment of the bone lesion and soft tissue uptake. Clinical history and familiarity with typical imaging appearances are crucial for distinguishing soft tissue masses.

Ethics

Informed Consent: Informed consent was obtained from the patient.

Authorship Contributions

Surgical and Medical Practices: S.U., A.J., K.A.R., Z.N., S.K., V.V.J., Concept: S.U., A.J., K.A.R., Design: S.U., Data Collection or Processing: S.U., S.K., V.V.J, Analysis or Interpretation: S.U., A.J., Z.N., Literature Search: S.U., Writing: S.U., A.J., K.A.R.

Conflict of Interest: No conflicts of interest were declared by the authors.

Financial Disclosure: The authors declare that this study has received no financial support.

References

1. Hall EJ, Wuu CS. Radiation-induced second cancers: the impact of 3D-CRT and IMRT. Int J Radiat Oncol Biol Phys 2003;56:83-88.
2. Di Lalla V, Tolba M, Khosrow-Khavar F, Baig A, Freeman C, Panet-Raymond V. Radiation-induced sarcomas of the breast: a review of a 20-year single-center experience. Cureus 2023;15:e38096.
3. Kirova YM, Vilcoq JR, Asselain B, Sastre-Garau X, Fourquet A. Radiation-induced sarcomas after radiotherapy for breast carcinoma: a large-scale single-institution review. Cancer 2005;104:856-863.
4. Usmani S, Ahmed N, Muzaffar S, Al Kandari F. Extensive extramedullary hematopoiesis in thalassemia: soft tissue uptake on 99mTc-MDP SPECT/CT. Clin Nucl Med 2020;45:e459-e460.
5. Usmani S, Gnanasegaran G, Marafi F, Esmail A, Ahmed N, Van den Wyngaert T. The clinical significance of incidental soft tissue uptake on whole body 18F-sodium fluoride bone PET-CT. Clin Radiol 2019;74:95-110.
6. Liu S, Xie J, Yu F, Cai H, Wu F, Zheng H, Ma C, Lv Z, Wang H. 99mTc-methylene diphosphonate uptake in soft tissue tumors on bone scintigraphy differs between pediatric and adult patients and is correlated with tumor differentiation. Cancer Manag Res 2020;12:2449-2457.

Interesting Image

Mol Imaging Radionucl Ther 2024;33:109-111 *DOI:10.4274/mirt.galenos.2023.80958*

Diagnosis and Evaluation of Treatment Response in Relapsing Polychondritis Using ^{18}F-FDG PET/CT

Tekrarlayan Polikondrit Tanısında ve Tedavi Yanıt Değerlendirmesinde ^{18}F-FDG PET/BT

Caner Civan[1], Emine Göknur Işık[1], Duygu Has Şimşek[1], Mustafa Altınkaynak[2], Serkan Kuyumcu[1]

[1]*İstanbul University, İstanbul Faculty of Medicine, Department of Nuclear Medicine, İstanbul, Türkiye*
[2]*İstanbul University, İstanbul Faculty of Medicine, Department of Internal Medicine, İstanbul, Türkiye*

Abstract

A 58-year-old man presenting with dyspnea, weight loss, and night sweating underwent ^{18}F-fluorodeoxyglucose positron emission tomography/computed tomography (^{18}F-FDG PET/CT) because of a suspicion of malignancy. ^{18}F-FDG PET/CT demonstrated mild to moderate uptake on nasal, cricoid, and tracheobronchial tree cartilages and costovertebral junctions. The diagnosis was relapsing polychondritis, which is a rare multisystem disease characterized by inflammation of cartilage. In addition, subsequent ^{18}F-FDG PET/CT after treatment showed complete metabolic response.

Keywords: Relapsing polychondritis, ^{18}F-FDG, PET/CT

Öz

Elli sekiz yaşında kadın hastaya nefes darlığı, kilo kaybı ve gece terlemesi şikayetleri ile malignite şüphesi nedeniyle ^{18}F-fluorodeoksiglukoz pozitron emisyon tomografisi/bilgisayarlı tomografi (^{18}F-FDG PET/BT) çalışması yapıldı. ^{18}F-FDG PET/BT'de nazal, krikoid, trakeobronşiyal ağaç kıkırdaklarında ve kostovertebral bileşkelerde ve hafif orta düzeyde tutulumlar gözlendi. Hastanın tanısı nadir görülen, multisistemik bir hastalık olan ve kıkırdakların enflamasyonu ile karakterize tekrarlayan polikondrit ile uyumlu idi. Tedavi sonrası yapılan ^{18}F-FDG PET/BT çalışmasında tam metabolik yanıt görülmekte idi.

Anahtar kelimeler: Tekrarlayan polikondrit, ^{18}F-FDG, PET/BT

Address for Correspondence: Caner Civan MD, İstanbul University, İstanbul Faculty of Medicine, Department of Nuclear Medicine, İstanbul, Türkiye
Phone: +90 535 559 39 25 **E-mail:** dr.canercivan@gmail.com ORCID ID: orcid.org/0000-0003-4745-3501
Received: 11.08.2023 **Accepted:** 26.11.2023 **Epub:** 19.02.2024

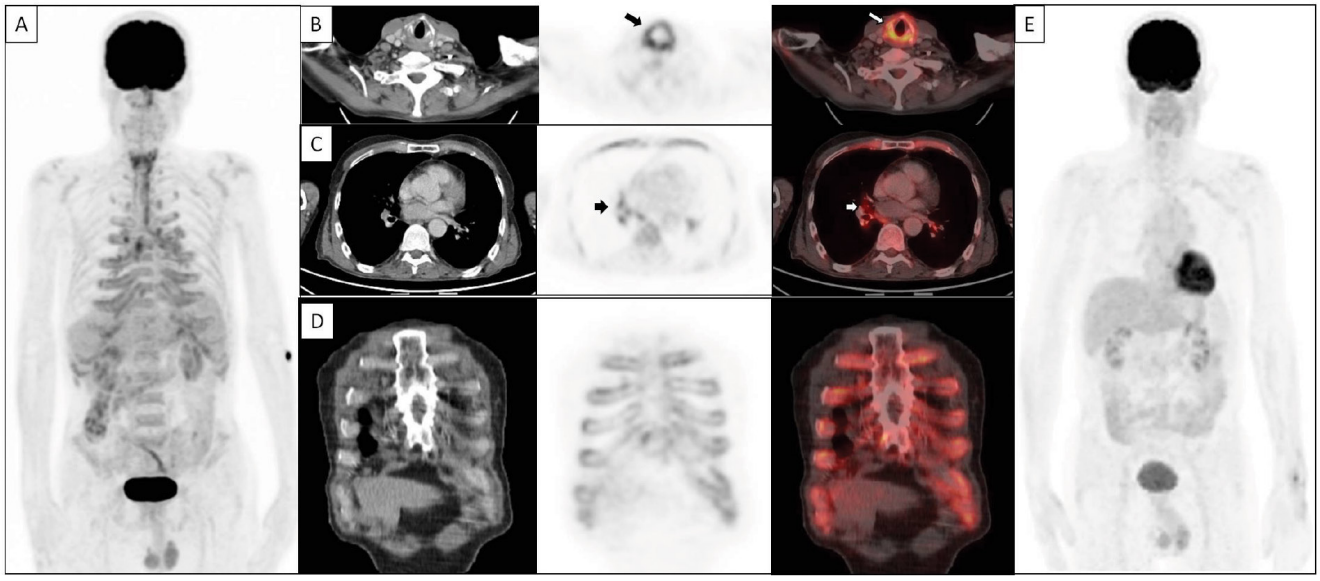

Figure 1. A 58-year-old man with a history of granulomatosis with polyangiitis presented with shortness of breath, hoarseness, myalgia, arthralgia, and weight loss of 10 kg within two months. Laboratory findings were as follows: C-reactive protein (CRP), 144 mg/L, erythrocyte sedimentation rate (ESR): 93, white blood cell counts, 12,000; and hemoglobin level, 10 g/dL. Due to anemia and age, the patient underwent gastroscopy and colonoscopy, which revealed esophagitis and gastritis. Because of suspected malignancy, the patient underwent ^{18}F-fluorodeoxyglucose positron emission tomography/computed tomography (^{18}F-FDG PET/CT) [A: maximum intensity projection, (MIP)], which showed increased FDG uptake in multiple cartilage joints. Transaxial images demonstrated increased uptake on the cricoid cartilage of the larynx [B: CT, PET and fuzed PET/CT images, arrow, maximum standardized uptake value (SUV_{max}): 6.8] and tracheobronchial cartilages (C: CT, PET and fuzed PET/CT images, arrow, SUV_{max}: 5.4). Coronal images of the thorax show (D: CT, PET and fuzed/CT images) increased FDG uptake at costochondral junctions (SUV_{max}: 3.4). Considering these findings, which were chondritis of the nasal cartilage and respiratory tract with a combination of clinical features, the diagnosis was confirmed as relapsing polychondritis (RPC). The patient received treatment with corticosteroids and methotrexate as anti-inflammatory agents. Subsequently, the patient underwent ^{18}F-FDG PET/CT (E: MIP) for response evaluation, which showed complete metabolic response and acute phase reactants within normal range (CRP: 1.58 mg/L, ESR: 8, white blood cell counts: 7,500). RPC is an orphan disease with an estimated incidence rate of 3.5 in 1 million people (1). RPC, which is associated with progressive autoimmune disorder of cartilage, presents with heterogeneous signs and symptoms in compliance with involvement of structures (2). Because of non-specific symptoms in the early stage of the disease, diagnosis has been delayed in most of the cases (2). Indeed, laboratory findings, part of the diagnostic work-up of RPC, were consistent with inflammation but non-specific to RPC (3). Based on the clinical features, various diagnostic criteria were proposed, including chondritis, which mainly involved auricular, nasal, and laryngotracheobronchial diseases, and arthropathy, which was mainly acute, asymmetric polyarthritis, or oligoarthritis (4). In the last decade, the utility of ^{18}F-FDG PET/CT has been proven in not only oncological purposes but also in non-oncological settings, including inflammatory disorders (5,6). The clinical importance of ^{18}F-FDG PET/CT in RPC for early diagnosis, targeted biopsy site, extent of disease, and treatment response evaluation has been shown in limited studies (7,8). This case highlights the importance of recognizing the typical distribution patterns of RPC on ^{18}F-FDG PET/CT for accurate diagnosis. Furthermore, ^{18}F-FDG PET/CT may play a role in evaluating the treatment response in RPC.

Ethics

Informed Consent: Patient consent was obtained.

Authorship Contributions

Surgical and Medical Practices: C.C., E.G.I., D.H.Ş., M.A., S.K., Concept: C.C., E.G.I., D.H.Ş., Design: C.C., E.G.I., D.H.Ş., Data Collection or Processing: C.C., M.A., Analysis or Interpretation: C.C., E.G.I., D.H.Ş., S.K., Literature Search: C.C., D.H.Ş., Writing: C.C., E.G.I., D.H.Ş., M.A., S.K.

Conflict of Interest: No conflicts of interest were declared by the authors.

Financial Disclosure: The authors declare that this study has received no financial support.

References

1. Luthra HS. Relapsing polychondritis. Primer on the rheumatic diseases, Springer 2008;451-454.
2. Longo L, Greco A, Rea A, Lo Vasco VR, De Virgilio A, De Vincentiis M. Relapsing polychondritis: A clinical update. Autoimmun Rev 2016;15:539-543.
3. Kingdon J, Roscamp J, Sangle S, D'Cruz D. Relapsing polychondritis: a clinical review for rheumatologists. Rheumatology (Oxford) 2018;57:1525-1532.
4. Borgia F, Giuffrida R, Guarneri F, Cannavò SP. Relapsing polychondritis: an updated review. Biomedicines 2018;6:84.
5. Zhuang H, Codreanu I. Growing applications of FDG PET-CT imaging in non-oncologic conditions. J Biomed Res 2015;29:189-202.
6. Pijl JP, Nienhuis PH, Kwee TC, Glaudemans AWJM, Slart RHJA, Gormsen LC. Limitations and pitfalls of FDG-PET/CT in infection and inflammation. Semin Nucl Med 2021;51:633-645.
7. Kubota K, Yamashita H, Mimori A. Clinical value of FDG-PET/CT for the evaluation of rheumatic Diseases: rheumatoid arthritis, polymyalgia rheumatica, and relapsing polychondritis. Semin Nucl Med 2017;47:408-424.
8. Kwok SH, Choi F. Relapsing polychondritis: the oto-rhino-tracheobronchial triad on 18 F-FDG PET/CT. Clin Nucl Med 2023;48:699-701.

Interesting Image

Mol Imaging Radionucl Ther 2024;33:112-114 *DOI:10.4274/mirt.galenos.2023.90582*

Late ^{68}Ga PSMA-positive Pancreatic Metastasis From Renal Cell Carcinoma in a Patient with Metastatic Prostate Cancer: A Mission Impossible

Metastatik Prostat Kanserli Bir Hastada Renal Hücreli Karsinomdan Geç ^{68}Ga PSMA-pozitif Pankreas Metastazı: İmkansız Bir Görev

Gabriela Mateva[1], Nikolina Novoselska[1], Assen Dudov[2], Marina Garcheva-Tsacheva[1], Pavel Bochev[1]

[1]*Acibadem City Clinic UMBAL Mladost Hospital, Department of Nuclear Medicine, Sofia, Bulgaria*
[2]*Acibadem City Clinic UMBAL Mladost Hospital, Department of Medical Oncology, Sofia, Bulgaria*

Abstract

We present the case of a patient with newly diagnosed high-risk prostate cancer. The patient underwent nephrectomy for renal cell carcinoma (RCC) in 2009. The prostate-specific membrane antigen (PSMA) scan revealed a primary tumor with seminal vessel involvement, PSMA-positive regional lymph nodes, several nodular lung lesions with mild PSMA uptake, PSMA-positive mediastinal lymph nodes, and a PSMA-positive mass in the pancreatic head. Ultrasound-guided biopsy was performed for the pancreatic lesions revealing metastasis from a RCC. Simultaneous treatment for prostate cancer and metastatic RCC was initiated. To separate metastatic sites for both primaries, we attempted to use fluorodeoxyglucose positron emission tomography/computed tomography, which was moderately positive for the pancreatic mass but not for the other locations. RCC is a ^{68}Ga PSMA-positive tumor; the synchronous combination of RCC with prostate cancer can be confusing and requires more complex clinical interpretation.

Keywords: PSMA, FDG, PET/CT, prostate cancer, RCC, pancreatic metastasis

Öz

Bu olgu sunumunda yeni tanı almış yüksek riskli prostat kanseri olan bir hastayı sunuyoruz. Hastaya 2009 yılında renal hücreli karsinom (RHK) nedeniyle nefrektomi uygulandı. Prostat spesifik membran antijeni (PSMA) taramasında seminal vezikül tutulumu olan primer bir tümör, PSMA pozitif bölgesel lenf nodları, hafif PSMA tutulumu olan birkaç nodüler akciğer lezyonu, PSMA-pozitif mediastinal lenf nodları ve pankreas başında PSMA pozitif kitle saptandı. Pankreas lezyonları için ultrason eşliğinde biyopsi yapıldı ve bu lezyonların RHK metastazı olduğunu ortaya çıkardı. Prostat kanseri ve metastatik RHK'nin eşzamanlı tedavisine başlandı. Her iki primer için metastatik bölgeleri ayırmak amacıyla, florodeoksiglukoz pozitron emisyon tomografisi/bilgisayarlı tomografiyi kullanmayı denedik; bu, pankreas kitlesi için orta derecede pozitifti, ancak diğer lokasyonlar için pozitif değildi. RHK, ^{68}Ga PSMA pozitif bir tümördür; RHK'nin prostat kanseri ile eşzamanlı kombinasyonu kafa karıştırıcı olabilir ve daha karmaşık klinik yorumlama gerektirir.

Anahtar kelimeler: PSMA, FDG, PET/BT, prostat kanseri, RHK, pankreas metastazı

Address for Correspondence: Gabriela Mateva MD, Acibadem City Clinic UMBAL Mladost Hospital, Department of Nuclear Medicine, Sofia, Bulgaria
Phone: +359894680648 **E-mail:** gabriela.mateva@abv.bg ORCID ID: orcid.org/0000-0001-8834-995X
Received: 28.08.2023 **Accepted:** 07.12.2023 **Epub:** 19.02.2024

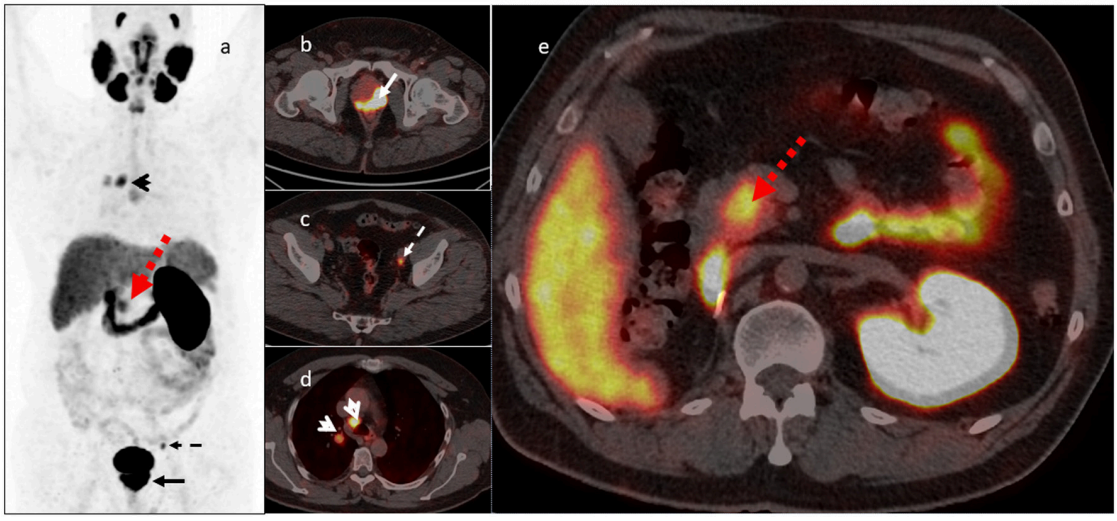

Figure 1. ^{68}Ga prostate-specific membrane antigen (PSMA) scan performed for staging of prostate cancer [Gleason score of 7 (4+3), grade group 3, initial prostate-specific antigen (PSA) 206 ng/mL] [a, maximum intensity projection (MIP) image], revealing a highly positive primary prostate tumor (b, arrow-axial hybrid image) with parailiac lymph node metastasis (c, dashed arrow-axial hybrid image), a PSMA-positive paratracheal lymph node, and a round, well-shaped lung metastasis (d, open arrow-axial hybrid image). PSMA-positive lesion in the pancreatic head (e, red arrow-axial hybrid image). The patient underwent nephrectomy for renal cell carcinoma (RCC) in 2009 and was considered to be in remission. Knowing that the pancreas is a possible location for late RCC metastasis and can be PSMA-positive (1,2), we recommended an ultrasound-guided biopsy for the pancreatic lesion, which proved infiltration by a typical clear cell renal carcinoma, PAX 8 and GATA3 positive, although RCC negative on immunohistochemistry. Simultaneous treatment for prostate cancer and metastatic RCC was initiated as follows: hormone therapy maximal androgen blockade for prostate cancer and bevacizumab/interferon, later changed to pazopanib for RCC.

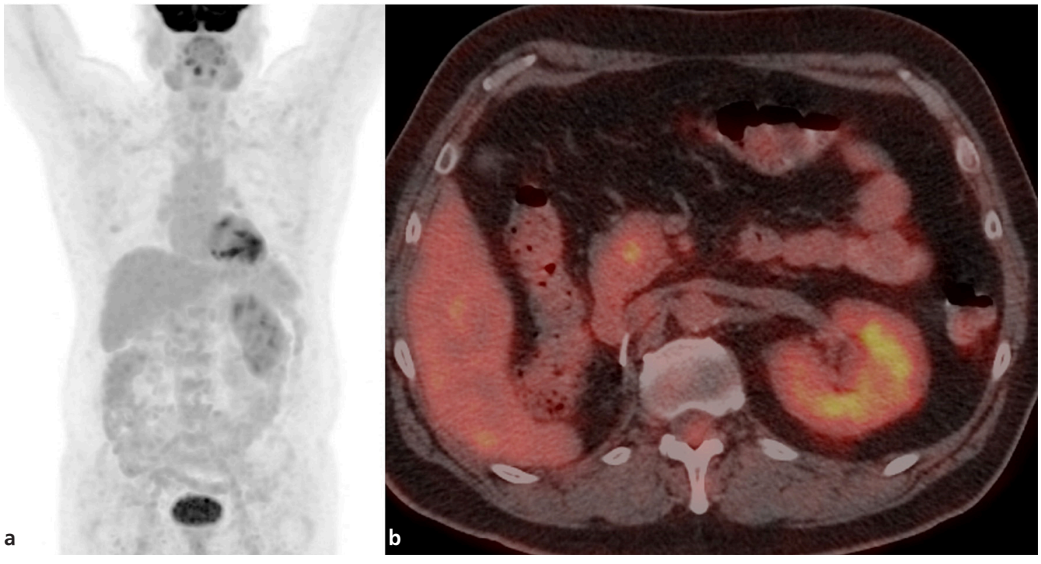

Figure 2. Fluorodeoxyglucose (FDG) positron emission tomography scan: pancreatic lesion is faintly FDG positive. The other lesions did not show substantial FDG uptake (should be borne on mind that the patient is under treatment at the time of the FDG scan). a. ^{18}F-FDG MIP image; b. ^{18}F-FDG axial hybrid imaging faint FDG uptake in the pancreatic lesion. To separate metastatic sites for both primaries, we attempted to use FDG PET/computed tomography (CT) (Figure 2) as a discriminator, as proposed in the literature (3). The scan was obtained after starting treatment for both and at PSA levels of 3.24 ng/mL. FDG was moderately positive for the pancreatic mass but not for the other locations (lung nodules were small volume) (Figure 2). On a size basis, there was no change in the pancreatic mass, but there was a reduction in the lung, mediastinal, and primary prostate sites, which additionally confused the interpretation. However, as a final decision, the patient had partial response for prostate cancer and non-progression (partial response or stable disease) for RCC and remained on the same treatment. This actually shows the inability of separating metastatic locations for all imaging modalities used (^{68}Ga PSMA, FDG, and CT) and the need for an individual approach and more complex clinical interpretation of the case.

Ethics

Informed Consent: The patient has consented to the use of his medical record for scientific purposes.

Authorship Contributions

Surgical and Medical Practices: A.D., P.B., Concept: P.B., Design: P.B., Data Collection or Processing: G.M., N.N., P.B., Analysis or Interpretation: G.M., N.N., M.G.-T., P.B., Literature Search: P.B., Writing: G.M., P.B.

Conflict of Interest: No conflicts of interest were declared by the authors.

Financial Disclosure: The authors declare that this study has received no financial support.

References

1. Katsourakis A, Noussios G, Hadjis I, Alatsakis M, Chatzitheoklitos E. Late solitary pancreatic metastasis from renal cell carcinoma: a case report. Case Rep Med 2012;2012:464808.
2. Demirci E, Ocak M, Kabasakal L, Decristoforo C, Talat Z, Halaç M, Kanmaz B. (68)Ga-PSMA PET/CT imaging of metastatic clear cell renal cell carcinoma. Eur J Nucl Med Mol Imaging 2014;41:1461-1462.
3. Tariq A, Kwok M, Pearce A, Rhee H, Kyle S, Marsh P, Raveenthiran S, Wong D, McBean R, Westera J, Dunglison N, Esler R, Navaratnam A, Yaxley JW, Thomas P, Pattison DA, Roberts MJ. The role of dual tracer PSMA and FDG PET/CT in renal cell carcinoma (RCC) compared to conventional imaging: A multi-institutional case series with intra-individual comparison. Urol Oncol 2022;40:66.e1-66.e9.

Interesting Image

Mol Imaging Radionucl Ther 2024;33:115-117 *DOI:10.4274/mirt.galenos.2023.17894*

Misdiagnosis of a Drain-site Hernia Containing Fallopian Tube Fimbria on ^{18}F-FDG PET/CT

^{18}F-FDG PET/BT'de Fallop Tüpü Fimbriası İçeren Drenaj Yeri Fıtığının Yanlış Teşhisi

Hui Li[1]*, Le Song[1]*, Bing-Qi Li[2], Na Guo[1], Weifang Zhang[1]

[1]Peking University Third Hospital, Department of Nuclear Medicine, Beijing, China
[2]Peking University Third Hospital, Department of General Surgery, Beijing, China
**H.L. and L.S. contributed equally to this work as co-first authors.*

Abstract

In a 55-year-old woman with sigmoid colon cancer, a subcutaneous mass in the left lower abdomen was incidentally found and gradually enlarged. For further diagnosis and staging, an ^{18}F-fluorodeoxyglucose (FDG) positron emission tomography/computed tomography scan was performed, which revealed a subcutaneous mass in the left lower abdomen with mild uptake of ^{18}F-FDG, suggesting the possibility of metastasis. However, post-surgery and pathological confirmation, this mass was diagnosed as a drain-site hernia containing fallopian tube fimbria, which is extremely rare but should be considered in the differential diagnosis of subcutaneous mass in the lower abdomen.

Keywords: Subcutaneous mass, ^{18}F-FDG PET/CT, drain-site hernia, fallopian tube fimbria

Öz

Sigmoid kolon kanserli 55 yaşındaki kadın hastada tesadüfen sol alt karın bölgesinde deri altı kitle saptandı ve bu kitle giderek büyüdü. Daha ileri tanı ve evreleme için ^{18}F-florodeoksiglukoz (FDG) pozitron emisyon tomografisi/bilgisayarlı tomografi taraması yapıldı ve bu taramada sol alt karın bölgesinde hafif ^{18}F-FDG tutulumuyla birlikte metastaz olasılığını düşündüren deri altı kitle saptandı. Ancak ameliyat sonrasında patolojik olarak bu kitlenin, son derece nadir görülen ancak alt karın bölgesindeki deri altı kitlelerin ayırıcı tanısında dikkate alınması gereken, fallop tüpü fimbriası içeren drenaj yeri fıtığı olduğu anlaşıldı.

Anahtar kelimeler: Deri altı kitle, ^{18}F-FDG PET/BT, drenaj yeri fıtığı, fallop tüpü fimbriası

Address for Correspondence: Weifang Zhang Prof. MD, Peking University Third Hospital, Department of Nuclear Medicine, Beijing, China
Phone: +86-010-82264935 **E-mail:** tsy1997@126.com ORCID ID: orcid.org/0000-0003-3879-1285
Received: 26.09.2023 **Accepted:** 07.12.2023 **Epub:** 09.02.2024

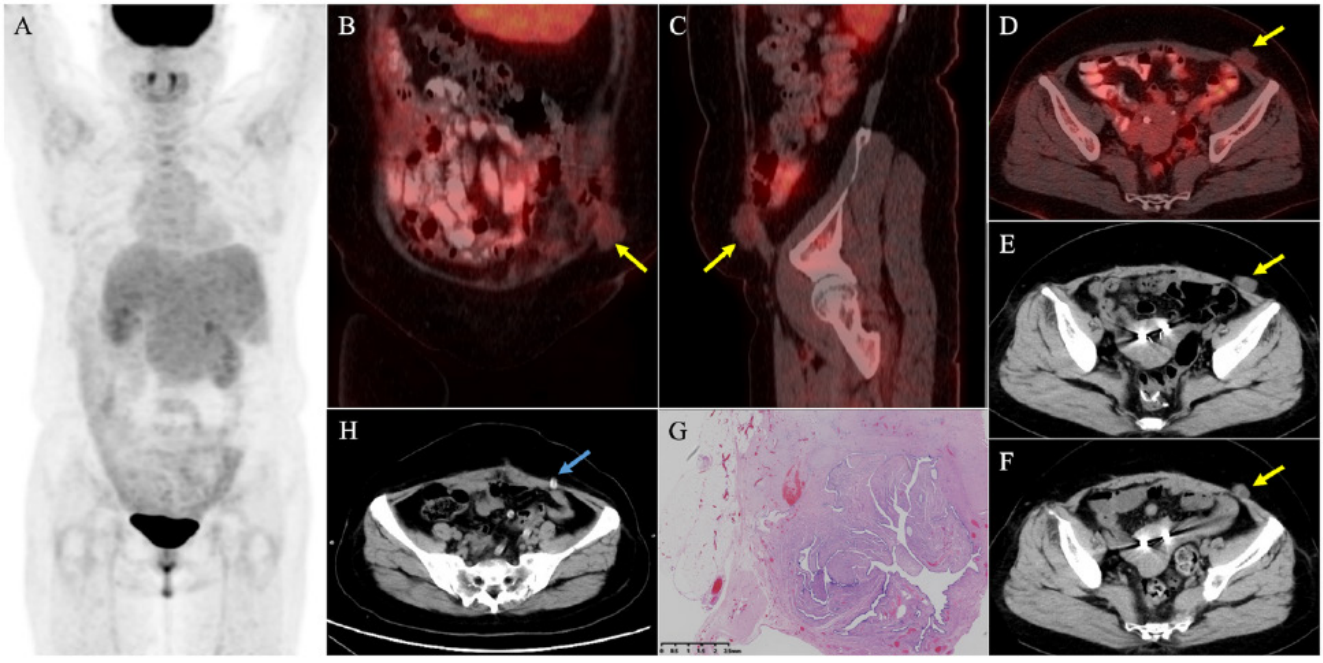

Figure 1. A 55-year-old woman with sigmoid colon cancer underwent laparoscopic sigmoid colectomy three years ago. Eight months after colectomy, she underwent right hepatectomy and chemotherapy because of newly diagnosed liver metastasis. Eight months after chemotherapy, the patient incidentally found a subcutaneous palpable hard mass in the left lower abdomen with slight intermittent abdominal discomfort. During follow-up, the mass gradually enlarged, while serum carcinoembryonic antigen levels remained within the normal range (2.6 to 3.3 ng/mL, normal reference range: 0-5.0 ng/mL). Twelve months after the discovery of the mass, an ^{18}F-fluorodeoxyglucose (FDG) positron emission tomography/computed tomography (PET/CT) scan was conducted for further diagnosis and staging [(A) maximum intensity projection, (B) coronal PET/CT, (C) sagittal PET/CT, (D) axial PET/CT], revealing an irregularly shaped subcutaneous mass in the left lower abdomen (B, C, and D, yellow arrow). The mass was closely related to the abdominal wall (without a remarkable defect) and showed mild uptake of ^{18}F-FDG (maximum standardized uptake value: 1.2). We then reviewed the serial CT scans (E and F, 6 and 12 months before the PET/CT scan), which demonstrated that the mass enlarged and became irregular. Therefore, the possibility of metastasis was raised. However, post-surgery and pathological confirmation (G, fallopian tube tissue could be seen in the fibrous and fatty tissue), this mass was finally diagnosed as a drain-site hernia (DSH) containing fallopian tube fimbria. We reviewed all previous CT scans of the patient and confirmed that the mass was indeed located above the former 5 mm drain site (H, blue arrow). In addition, the mass appeared six months post-colectomy and gradually enlarged, but it was missed by the radiologist. This misdiagnosis should serve as a reminder of the following three lessons. First, we should enhance and broaden our understanding of rare hernias. Trocar site hernia (TSH) is rare and is defined as an incisional hernia occurring at the trocar incision site after laparoscopic surgery (1). Among TSH, DSH is an even rarer type, occurring at the port site where the drainage tube is placed (2). Its prevalence ranges from 0.1% to 3.4% according to the literature. Trocar size is the dominant risk factor for DSH, which often occurs at the ≥10 mm port site and rarely occurs at the 5 mm port site (as observed in this patient) (3,4,5). Second, we need to broaden and improve our knowledge of the atypical contents of hernias. The most common contents of hernias are the small bowel and omentum. The uncommon hernia contents, such as the fallopian tube in this case, appendix, ovary, gall bladder, and bladder, are rare but cannot be ignored (2,6,7,8). It should be noted that any organ within the abdominal cavity might herniate. DSH-containing fallopian tubes are extremely rare, with only three cases reported (6,7,8). Finally, a thorough review of previous clinical image data and patient history is essential for accurate diagnosis. If we could comprehensively review all previous CT scans, this misdiagnosis might be avoided. In summary, although a DSH containing the fallopian tube fimbria is extremely rare, this misdiagnosed case suggests that it should be considered in the differential diagnosis of a subcutaneous mass in the lower abdomen.

Ethics

Informed Consent: Written informed consent has been obtained from the patient.

Authorship Contributions

Surgical and Medical Practices: B.Q.L., Concept: W.Z., Design: W.Z., Data Collection or Processing: N.G., Analysis or Interpretation: L.S., Literature Search: H.L., L.S., Writing: H.L.

Conflict of Interest: No conflict of interest was declared by the authors.

Financial Disclosure: This work was supported by the Key Clinical Projects of Peking University Third Hospital (no: BYSY2022060).

References

1. Gao X, Chen Q, Wang C, Yu YY, Yang L, Zhou ZG. Rare case of drain-site hernia after laparoscopic surgery and a novel strategy of prevention: A case report. World J Clin Cases 2020;8:6504-6510.
2. Makama JG, Ameh EA, Garba ES. Drain Site Hernia: A Review of the Incidence and Prevalence. West Afr J Med 2015;34:62-68.
3. Su J, Deng C, Yin HM. Drain-site hernia after laparoscopic rectal resection: A case report and review of literature. World J Clin Cases 2022;10:2637-2643.
4. Nacef K, Chaouch MA, Chaouch A, Khalifa MB, Ghannouchi M, Boudokhane M. Trocar site post incisional hernia: about 19 cases. Pan Afr Med J 2018;29:183.
5. Helgstrand F, Rosenberg J, Bisgaard T. Trocar site hernia after laparoscopic surgery: a qualitative systematic review. Hernia 2011;15:113-121.
6. Sharma L, Singh A, Bhaskaran S, Radhika AG, Radhakrishnan G. Fallopian tube herniation: an unusual complication of surgical drain. Case Rep Obstet Gynecol 2012;2012:194350.
7. Ergin A, Işcan Y, Ağca B, Karip B, Memisoğlu K. Fallopian tube herniation from trocar-site after laparoscopic appendectomy. Ulus Travma Acil Cerrahi Derg 2020;26:639-641.
8. Hussain K, Masood J. Fallopian Tube Herniation through Left Sided Abdominal Drain Site. J Coll Physicians Surg Pak 2016;26:S19-20.

Interesting Image

Mol Imaging Radionucl Ther 2024;33:118-120 *DOI:10.4274/mirt.galenos.2023.37980*

Lincoln Sign: A Rare Presentation of Medication-related Osteonecrosis of the Jaw

Lincoln İşareti: İlaçla İlişkili Çene Osteonekrozunun Nadir Bir Göstergesi

Tsz-Kit Chow, Jocelyn Chu

Tuen Mun Hospital, Department of Radiology and Nuclear Medicine, Nuclear Medicine Unit, Hong Kong, China

Abstract

A 52-year-old female patient with metastatic breast cancer receiving denosumab for 7 years presented with marked diffuse tracer uptake in the mandible on Tc-99m-methylene diphosphonate bone scintigraphy, resembling the Lincoln sign. A diagnosis of medication-related osteonecrosis of the jaw (MRONJ) was confirmed, leading to immediate discontinuation of denosumab. Conservative therapy, including limited debridement and oral rinses, was initiated. MRONJ, a potential complication of bone-modifying agents, is more prevalent in advanced malignancy cases. The Lincoln sign has not been previously reported in MRONJ, emphasizing its consideration in cancer patients undergoing bone-modifying agent treatment.

Keywords: Lincoln sign, medication-related osteonecrosis of the jaw, Tc-99m-methylene diphosphonate bone scintigraphy

Öz

Yedi yıl boyunca denosumab tedavisi alan metastatik meme kanseri olan 52 yaşındaki kadın hastaya yapılan Tc-99m-metilen difosfonat kemik sintigrafisinde mandibulada Lincoln işaretine benzeyen belirgin radyoaktivite tutulumu saptandı. İlaca bağlı çene osteonekrozu (MRONJ) tanısı doğrulandı ve denosumab derhal kesildi. Sınırlı debridman ve ağız gargarasını içeren konservatif tedavi başlandı. Kemik düzenleyici ajanların potansiyel bir komplikasyonu olan MRONJ, ileri malignite olgularında daha yaygındır. Lincoln işaretinin daha önce MRONJ'de bildirilmemiş olması, kemik düzenleyici ajan tedavisi gören kanser hastalarında dikkate alınması gerektiğini vurgulamaktadır.

Anahtar kelimeler: Lincoln işareti, ilaca bağlı çene osteonekrozu, Tc-99m-metilen difosfonat kemik sintigrafisi

Address for Correspondence: Tsz-Kit Chow MD, Tuen Mun Hospital, Department of Radiology and Nuclear Medicine, Nuclear Medicine Unit, Hong Kong, China
Phone: +852-38942527 **E-mail:** ctk594@ha.org.hk ORCID ID: orcid.org/0000-0002-1736-8771
Received: 17.10.2023 **Accepted:** 17.12.2023 **Epub:** 09.02.2024

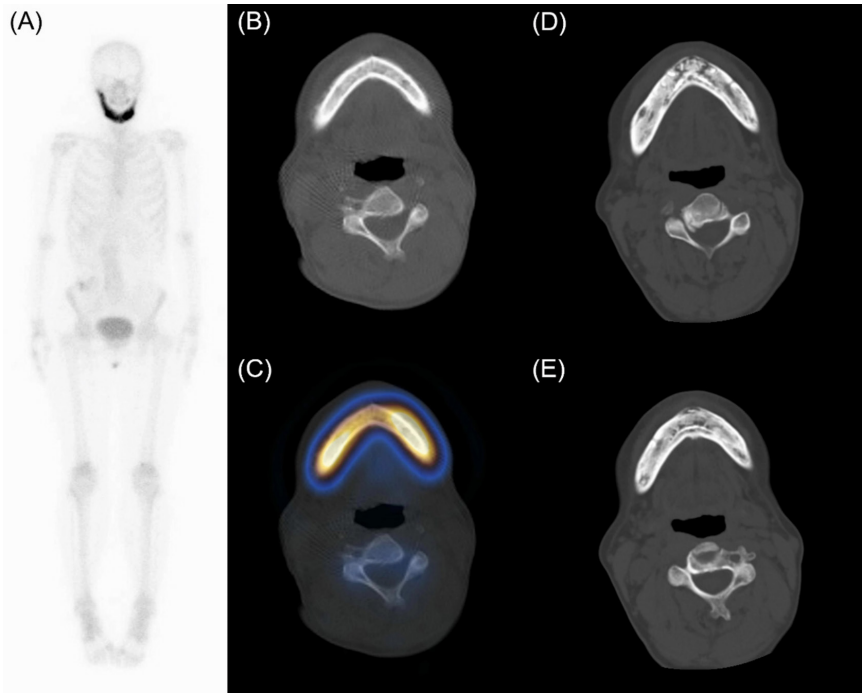

Figure 1. A 52-year-old woman, who was known to have stage IV breast cancer with metastasis to bone and liver and was administered a subcutaneous injection of denosumab for 7 years, presented with gradual onset of non-mobile submental hard mass and oral ulcer. There was no history of radiation therapy or metastatic disease of the jaws. The patient was referred for Tc-99m-methylene diphosphonate (MDP) bone scintigraphy to rule out progression of bone metastasis. Whole-body Tc-99m-MDP bone scintigraphy showed marked diffuse tracer uptake in the mandible, resembling the Lincoln sign (A). Single photon emission computed tomography/computed tomography (CT) demonstrated diffuse sclerosis with periosteal reaction in the mandible (B, C). No other abnormal bony tracer uptake focus was observed. Physical examination by a dental surgeon revealed bilateral orocutaneous fistulas at the lower border of the mandible with exposed bone. A clinical diagnosis of stage III medication-related osteonecrosis of the jaw (MRONJ) was made. Denosumab was discontinued immediately. The patient opted for conservative therapy with limited debridement and oral rinses with chlorhexidine. A subsequent CT study performed three years later showed diffuse sclerotic appearance of the mandible with multiple irregular lucency in the mandibular body and cortical bone loss (D, E), consistent with MRONJ. MRONJ is a potentially serious complication of bone modifying agent (BMA), which is more common in patients with advanced malignancy than in patients with osteoporosis (1). The cumulative incidence rates of MRONJ increase with longer duration of BMA exposure, with an incidence of 0.7%-1.4% during the first year of therapy and increasing to 2%-3.4% with continued treatment beyond one year (2). Other risk factors of MRONJ include previous oral surgery, periodontal disease, use of dentures, smoking, angiogenesis inhibitors, and diabetes (3). MRONJ can be classified into stages I-III, depending on the presence of exposed and necrotic bones, fistulas that probe to bone, symptoms, evidence of infection, and extent of lesions (3). Symptomatic treatment with antibacterial mouth rinse and analgesics can be administered to patients with early-stage disease, whereas surgical debridement or resection may be required for those with advanced-stage disease. The Lincoln sign on bone scintigraphy is characteristic of monostotic Paget's disease of the mandible and is less commonly observed in primary mandibular tumors (4), contiguous spread of oral malignancies (4), or distant metastases to the mandible (5). The Lincoln sign has not been reported in MRONJ previously, and this condition should be considered in cancer patients treated with BMA.

Ethics

Informed Consent: Informed consent was obtained from the patient.

Authorship Contributions

Surgical and Medical Practices: T.-K.C., J.C., Concept: T.-K.C., Design: T.-K.C., Data Collection or Processing: T.-K.C., Analysis or Interpretation: T.-K.C., Literature Search: T.-K.C., Writing: T.-K.C.

Conflict of Interest: All authors have disclosed no conflicts of interest.

Financial Disclosure: The authors declared that this study received no financial support.

References

1. Goodwin JS, Zhou J, Kuo YF, Baillargeon J. Risk of Jaw Osteonecrosis After Intravenous Bisphosphonates in Cancer Patients and Patients Without Cancer. Mayo Clin Proc 2017;92:106-113.
2. Stopeck AT, Fizazi K, Body JJ, Brown JE, Carducci M, Diel I, Fujiwara Y, Martín M, Paterson A, Tonkin K, Shore N, Sieber P, Kueppers F, Karsh L, Yardley D, Wang H, Maniar T, Arellano J, Braun A. Safety of long-term denosumab therapy: results from the open label extension phase of two phase 3 studies in patients with metastatic breast and prostate cancer. Support Care Cancer 2016;24:447-455.
3. Yarom N, Shapiro CL, Peterson DE, Van Poznak CH, Bohlke K, Ruggiero SL, Migliorati CA, Khan A, Morrison A, Anderson H, Murphy BA, Alston-Johnson D, Mendes RA, Beadle BM, Jensen SB, Saunders DP. Medication-Related Osteonecrosis of the Jaw: MASCC/ISOO/ASCO Clinical Practice Guideline. J Clin Oncol 2019;37:2270-2290.
4. Bal CS, Sahoo MK, Damle N. Lincoln's sign: where should we expect on 99mTc-MDP bone scintigraphy? Clin Nucl Med 2013;38:e390-e391.
5. Kulkarni M, Soni A, Shetkar S, Amer M, Mulavekar A, Joshi P. Coexistent Superscan and Lincoln Sign on Bone Scintigraphy. Clin Nucl Med 2017;42:630-632.

Interesting Image

Mol Imaging Radionucl Ther 2024;33:121-124 *DOI:10.4274/mirt.galenos.2023.69672*

An Uncommon Case of Pediatric Nasopharyngeal Carcinoma with Bone Metastases and Enchondromas Evaluated Using ^{18}F-FDG PET/CT

^{18}F-FDG PET/BT Taraması ile Değerlendirilen, Kemik Metastazları ve Enkondromları Olan Nadir Bir Pediatrik Nazofaringeal Karsinom Olgusu

Natale Quartuccio[1]*, Salvatore Ialuna[1]*, Salvatore Poma[2], Vincenzo Luca Lentini[3], Alessandro Pitruzzella[4], Giuseppe Mario Galfano[2], Antonino Maria Moreci[1], Domenico Michele Modica[2,4]

[1]Ospedali Riuniti Villa Sofia-Cervello, Department of Nuclear Medicine, Palermo, Italy
[2]Ospedali Riuniti Villa Sofia-Cervello, U.O.C. Otolaryngology, Palermo, Italy
[3]Ospedali Riuniti Villa Sofia-Cervello, Unit of Pathology, Palermo, Italy
[4]University of Palermo, Neurosciences and Advanced Diagnostics (BIND), Institute of Human Anatomy and Histology, Department of Biomedicine, Palermo, Italy

Abstract

Nowadays, the utility of positron emission tomography/computed tomography (PET/CT) is well established in nasopharyngeal carcinoma (NPC). The incidence of NPC in the West population, especially in children, is very low. We present the first Italian case of a pediatric patient with NPC followed up with ^{18}F-fluorodeoxyglucose (^{18}F-FDG) PET/CT scan in addition to the standard follow-up imaging methods, including CT and magnetic resonance imaging. The ^{18}F-FDG PET/CT scan was helpful in discriminating between metastatic and benign osseous lesions, thereby helping clinicians to determine the most appropriate therapeutic regimen. These findings support the clinical utility of ^{18}F-FDG PET/CT in the diagnostic work-up of pediatric patients with NPC.

Keywords: Positron emission tomography, ^{18}F-fluorodeoxyglucose, nasopharyngeal carcinoma, pediatrics

Öz

Günümüzde nazofaringeal karsinomda (NFK) pozitron emisyon tomografisi/bilgisayarlı tomografinin (PET/BT) kullanımı iyice yerleşmiştir. Batı popülasyonunda, özellikle de pediatrik yaşta NFK'nin görülme sıklığı çok düşüktür. BT ve manyetik rezonans görüntüleme dahil olmak üzere standart takip görüntüleme yöntemlerine ek olarak ^{18}F-florodeoksiglukoz (^{18}F-FDG) PET/BT taraması yoluyla takip edilen NFK'li ilk İtalyan pediatrik hastayı sunuyoruz. ^{18}F-FDG PET/BT taraması, metastatik ve iyi huylu kemik lezyonları arasında ayrım yapılmasında ve klinisyenlerin en uygun terapötik rejimi belirlemesine yardımcı olmuştur. Bu bulgular, NFK'li pediatrik hastaların tanısal çalışmalarında ^{18}F-FDG PET/BT taramasının klinik faydasını desteklemektedir.

Anahtar kelimeler: Pozitron emisyon tomografisi, ^{18}F-florodeoksiglukoz, nazofaringeal karsinom, pediatri

Address for Correspondence: Natale Quartuccio MD, Ospedali Riuniti Villa Sofia-Cervello, Department of Nuclear Medicine, Palermo, Italy
*These authors contributed equally to this work.
Phone: +390917804242 **E-mail:** n.quartuccio@villasofia.it ORCID ID: orcid.org/0000-0001-9845-1384
Received: 20.08.2023 **Accepted:** 27.12.2023 **Epub:** 19.02.2024

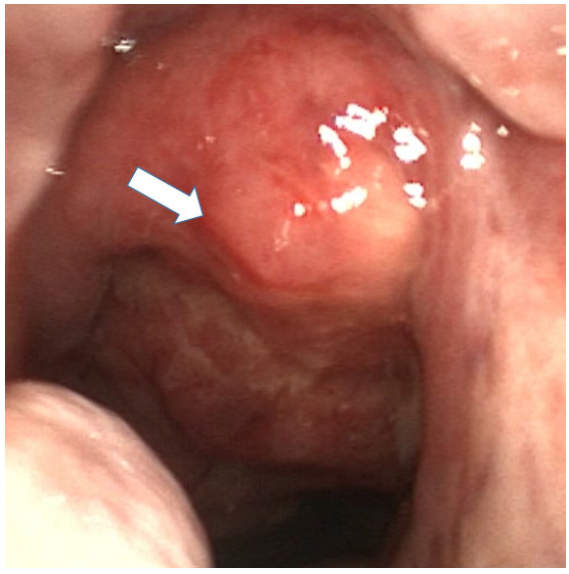

Figure 1. A 15-year-old adolescent was directed to our care because of recent occurrences of bloody nasal discharge, nasal blockage, and pain in the right ear. These symptoms had appeared approximately a month earlier. A video examination of the nose and throat revealed a lesion (indicated by a white arrow) on the right side of the nasopharynx, which was subsequently subjected to a biopsy procedure performed under general anesthesia.

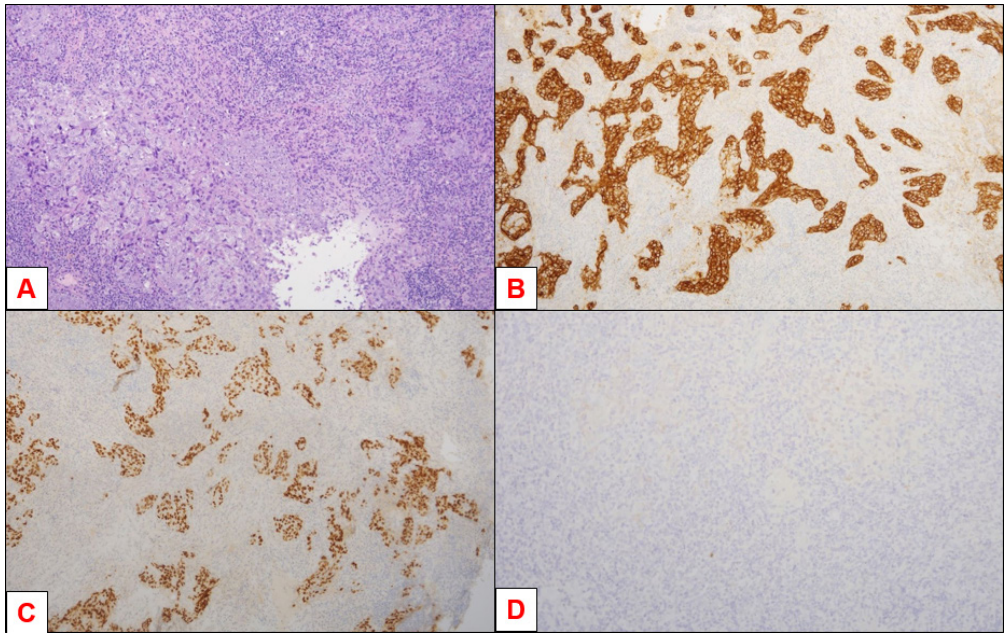

Figure 2. The tissue sample was sent for pathology. Histological examination (A-D) of the lesion identified a non-keratinizing undifferentiated carcinoma [classified as World Health Organization (WHO) type 3] located in the nasopharynx/rhinopharyn revealed non-keratinizing undifferentiated carcinoma (WHO type 3) of the nasopharynx. A: Hematoxylin and eosin staining (at 10x magnification) demonstrates lymphoid tissue mixed to an undifferentiated, atypical neoplastic cell population. B: At 10x magnification, immunohistochemical staining revealed positivity for an antibody targeting cytokeratin (Monoclonal Mouse Anti-Human Cytokeratin, Clone MNF116, Isotype: IgG1, kappa, 1:300; Dako Deutschland GmbH, Hamburg, Germany). C: The immunohistochemical staining at 10x magnification demonstrated p40 immunostaining positivity, supporting the diagnosis of squamous cell differentiation. D: At 20x magnification, immunohistochemical staining demonstrated Epstein-Barr virus (EBV)-encoded RNA positivity, indicating the EBV viral genome within neoplastic cells.

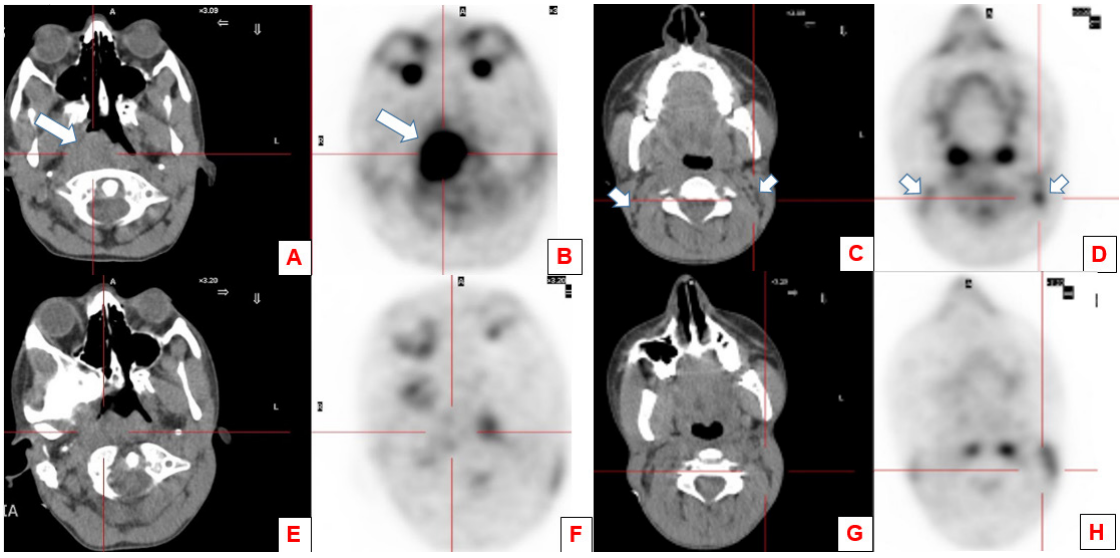

Figure 3. In addition to contrast-enhanced (CE) computed tomography (CT) and head and neck magnetic resonance imaging (MRI), the patient underwent a ^{18}F-fluorodeoxyglucose positron emission tomography/CT (^{18}F-FDG PET/CT) scan for local staging of nasopharyngeal carcinoma (NPC). PET/CT scans were acquired on an integrated PET/CT scanner (Discovery ST, General Electric Medical System, Milwaukee, WI, USA). The lesion identified on the CT component (white arrow, A) of the PET/CT scanner demonstrated anterior extension toward the septum and involvement of the retropharyngeal and prevertebral regions. PET/CT scan demonstrated increased ^{18}F-FDG uptake [maximum standardized uptake value (SUV_{max}): 14.3] (white arrow, B) within a solid right-sided mass. The mass had a maximum diameter of 47 mm on the axial plane and was located in the right vault wall of the nasopharynx. In addition, bilateral ^{18}F-FDG-avid (SUV_{max}: 7.5) superior jugular lymph nodes (white arrows, C, D), suspected for metastatic lesions, were noted. The child underwent three courses of induction chemotherapy (cisplatin/5-fluorouracil) and a further PET/CT scan, which demonstrated decreased size and uptake of the nasopharyngeal mass (E, F) and lymph nodes (G, H). Subsequently, the patient underwent radiotherapy (64.8 Gy) with concomitant chemotherapy.

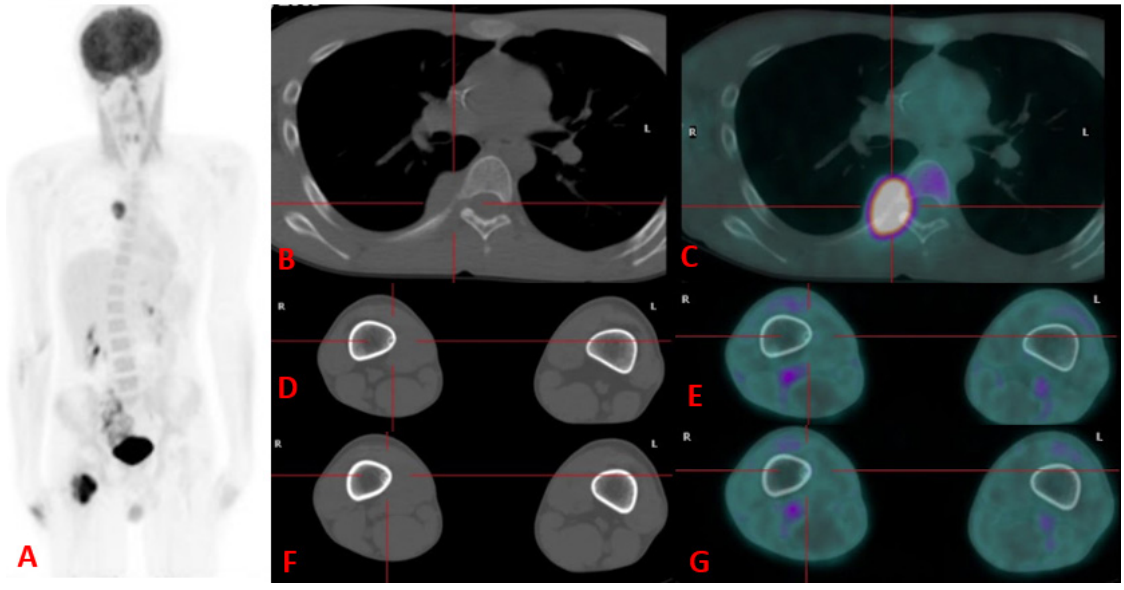

Figure 4. Two months later, the patient experienced right leg pain, prompting the referring clinician to order a leg CE MRI. MRI revealed a pathological tissue with a likely heteroplastic appearance, displaying prominent contrast enhancement in the intertrochanteric and lesser trochanter regions of the right femur. This tissue did not involve the cortical bone but infiltrated the muscular plane adjacent to the lesion in the medial region of the thigh. Additionally, two further doubtful well-defined lesions, measuring 4 and 2 cm, were observed in the distal diaphysis of the right femur.

An additional ^{18}F-FDG PET/CT was conducted, highlighting increased uptake in the intertrochanteric and lesser trochanter lesions, whereas the other two distal diaphysis lesions showed no significant ^{18}F-FDG uptake. Furthermore, a further hypermetabolic lesion (SUV_{max}: 8.4) was noted in the right-sided sixth costovertebral joint. On the left box (A) maximum intensity projection image showing ^{18}F-FDG-avid metastases in the intertrochanteric and lesser trochanter regions of the right femur and in the sixth right-sided rib, with corresponding CT and fuzed PET/CT images in boxes B and C, respectively. An additional ^{18}F-FDG-avid lesion involving the great and lesser trochanter of the right femur was observed, whereas tiny lesions seen on CT images were confirmed to be enchondromas with no significant FDG uptake (D, E, F, G).

Based on the PET/CT findings, chemotherapy with gemcitabine and oxaliplatin was administered, and radiation therapy (30 Gy) was delivered to the proximal region of the right femur. After 5 months, post-therapy PET/CT revealed the disappearance of the hypermetabolic lesions in keeping with a complete metabolic response to therapy. Since then, the boy has been followed up by two further ^{18}F-FDG PET/CT scans with no evidence of disease recurrence. The lesions in the distal diaphysis of the right femur were followed up by MRI and after 1 year remained unchanged, in keeping with enchondromas, according to the radiologist.

The incidence of NPC in the Western countries is low (especially in the pediatric age) compared with that in South-Eastern Asia (one vs. 8 per 100,000 person per year) (1,2). Although most nasopharyngeal lesions in the pediatric population are benign, the possibility of NPC should be considered when symptoms last long (3). Current imaging methods used to assess NPC at diagnosis and follow-up include CT, MRI, and bone scan. To the best of our knowledge, this is the first pediatric case of NPC evaluated by ^{18}F-FDG PET/CT reported in Italy. ^{18}F-FDG PET/CT emerged as an additional tool because of its metabolic information, helping characterize doubtful findings at conventional imaging (4). In our case, ^{18}F-FDG PET/CT played a crucial role in characterizing the enchondromas in the distal femur, as these well-defined lesions on the MRI scan demonstrated no significant uptake of ^{18}F-FDG, consistent with previous findings in the literature. Only three pediatric case reports (5,6,7) and one original study (4) including exclusively pediatric patients with NPC have been published in western countries so far. In that original study, Cheuk et al. (4) proved in a group of 86 children that MRI is superior to ^{18}F-FDG PET/CT in the local staging and detection of local lymph node metastases. Nevertheless, ^{18}F-FDG PET/CT was useful to address the correct nature of ambiguous findings suspected for distant metastases and to estimate complete disease remission at 3-6 months after months, a timeline earlier than that achievable with MRI (4).

Ethics

Informed Consent: Informed consent was obtained from all patients included in the study.

Authorship Contributions

Surgical and Medical Practices: S.I., S.P., A.P., Concept: D.M.M., Design: S.P., Data Collection or Processing: V.L.L., A.M.M., Analysis or Interpretation: S.I., A.P., G.M.G., Literature Search: N.Q., Writing: N.Q., D.M.M.

Conflict of Interest: No conflicts of interest were declared by the authors.

Financial Disclosure: The authors declare that this study has received no financial support.

References

1. Gatta G. Epidemiological Aspects in Nasopharyngeal Cancer. In: Vermorken JB, Budach V, Leemans CR, Machiels J-P, Nicolai P, O'Sullivan B (eds.) Critical Issues in Head and Neck Oncology. Cham, Springer 2021;319-325.
2. Boussen H, Bouaouina N, Mokni-Baizig N, Gamoudi A, Chouchane L, Benna F, Ladgham A. Les carcinomes du nasopharynx: donnée actuelles [Nasopharyngeal carcinoma. Recent data]. Pathol Biol (Paris) 2005;53:45-51.
3. Ben-Ami T, Kontny U, Surun A, Brecht IB, Almaraz RL, Dragomir M, Pourtsidis A, Casanova M, Fresneau B, Bisogno G, Schneider DT, Reguerre Y, Bien E, Stachowicz-Stencel T, Österlundh G, Wygoda M, Janssens GO, Zsiros J, Jehanno N, Brisse HJ, Gandola L, Christiansen H, Claude L, Ferrari A, Rodriguez-Galindo C, Orbach D. Nasopharyngeal carcinoma in children and adolescents: The EXPeRT/PARTNER diagnostic and therapeutic recommendations. Pediatr Blood Cancer 2021;68:e29018.
4. Cheuk DK, Sabin ND, Hossain M, Wozniak A, Naik M, Rodriguez-Galindo C, Krasin MJ, Shulkin BL. PET/CT for staging and follow-up of pediatric nasopharyngeal carcinoma. Eur J Nucl Med Mol Imaging 2012;39:1097-1106.
5. Stolten M, Moak S, Chauhan A, Warrier R. Facial pain in a child with attention deficit hyperactivity disorder. Clin Pediatr (Phila) 2016;55:196-198.
6. Muzaffar R, Vacca F, Guo H, Mhapsekar R, Osman MM. Pediatric nasopharyngeal carcinoma as seen on 18F-FDG PET/CT. Front Oncol 2019;9:110.
7. Stokken J, Manz RM, Flagg A, Kate Gowans L, Anne S. Synchronous occurrence of nasopharyngeal carcinoma and Hodgkin lymphoma. Int J Pediatr Otorhinolaryngol 2014;78:154-156.

Interesting Image

Mol Imaging Radionucl Ther 2024;33:125-128 *DOI:10.4274/mirt.galenos.2023.83435*

^{18}F-FDG and ^{68}Ga-FAPI-04 PET/CT Findings of a Rare Epithelial-myoepithelial Carcinoma Arising From Ex Pleomorphic Adenoma of Parotid

Parotidin Eski Pleomorfik Adenomundan Kaynaklanan Nadir Bir Epitelyal-miyoepitelyal Karsinomun ^{18}F-FDG ve ^{68}Ga-FAPI-04 PET/CT Bulguları

Caner Civan[1], Duygu Has Şimşek[1], Doğu Vurallı Bakkaloğlu[2], Serkan Kuyumcu[1]

[1]İstanbul University, İstanbul Faculty of Medicine, Department of Nuclear Medicine, İstanbul, Türkiye
[2]İstanbul University, İstanbul Faculty of Medicine, Department of Pathology, İstanbul, Türkiye

Abstract

Epithelial-myoepithelial carcinoma (EMC) is a rare low-grade salivary gland neoplasm. Distant metastasis is rare, and ^{18}F-fluorodeoxyglucose positron emission tomography/computed tomography (^{18}F-FDG PET/CT) has been used to determine the metastatic disease in EMC. ^{68}Ga-fibroblast activation protein inhibitors (FAPI) PET/CT is a promising imaging modality for diagnostic and theognostic purposes in various malignancies. Comparison studies with ^{18}F-FDG have investigated the role of ^{68}Ga-FAPI PET/CT. Herein, we present ^{18}F-FDG and ^{68}Ga-FAPI-04 PET/CT findings of a 51-year-old woman with metastatic EMC arising from ex-pleomorphic adenoma of the parotid.

Keywords: ^{68}Ga-FAPI, ^{18}F-FDG, PET/CT, epithelial myoepithelial carcinoma

Öz

Epitelyal-miyoepitelyal karsinom (EMK), nadir görülen düşük gradlı tükürük bezi neoplazmıdır. Uzak metastazlar nadir görülmekte olup EMK'de metastatik hastalığı tespit etmek için ^{18}F-florodeoksiglukoz pozitron emisyon tomografisi/bilgisayarlı tomografi (^{18}F-FDG PET/BT) kullanılmaktadır. ^{68}Ga-fibroblast aktivasyon proteini inhibitörleri (FAPI) PET/BT, çeşitli malignitelerde tanıda ve teranostik amaçla kullanılan umut verici bir görüntüleme yöntemidir. ^{18}F-FDG PET/BT ile karşılaştırmalı yapılan çalışmalar ^{68}Ga-FAPI PET/BT'nin rolünü araştırmaktadır. Bu olguda parotisin eks pleomorfik adenomundan kaynaklanan metastatik EMK tanılı 51 yaşında kadın hastanın ^{18}F-FDG ve ^{68}Ga-FAPI-04 PET/BT bulgularını sunuyoruz.

Anahtar kelimeler: ^{68}Ga-FAPI, ^{18}F-FDG, PET/BT, epitelyal miyoepitelyal karsinom

Address for Correspondence: Caner Civan MD, İstanbul University, İstanbul Faculty of Medicine, Department of Nuclear Medicine, İstanbul, Türkiye
Phone: +90 535 559 39 25 **E-mail:** dr.canercivan@gmail.com ORCID ID: orcid.org/0000-0003-4745-3501
Received: 12.08.2023 **Accepted:** 27.12.2023 **Epub:** 19.02.2024

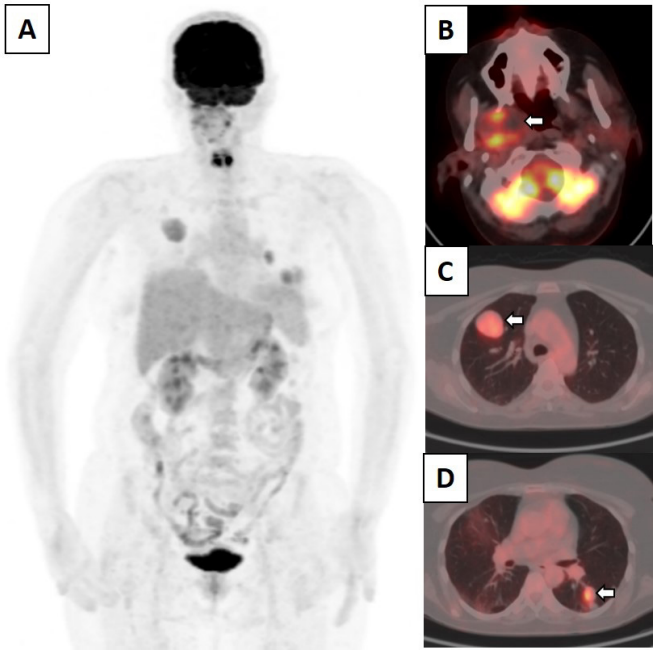

Figure 1. A 51-year-old woman with a history of parotidectomy due to pleomorphic adenoma five years ago was referred for ^{18}F-fluorodeoxyglucose positron emission tomography/computed tomography (^{18}F-FDG PET/CT) due to suspicious lung nodules. Maximum intensity projection (A: MIP) and transaxial fused ^{18}F-FDG PET/CT images showing a hypermetabolic mass located in the right parapharyngeal region (B: arrow), in addition to multiple lung lesions with mild to moderate FDG uptake (C, D: arrows).

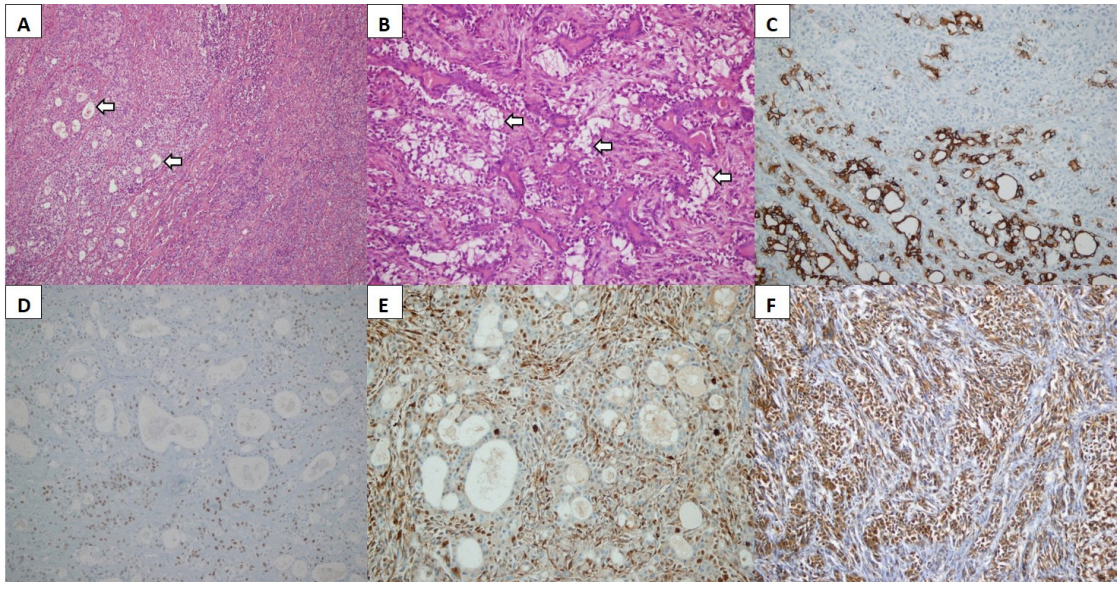

Figure 2. Microscopic examination demonstrated that the tumor was composed of a bilayered arrangement of inner ductal cells (A: arrows) and outer myoepithelial cells (B: arrows). The inner luminal cells were immunoreactive for cytokeratin 7 (C) and EMA, whereas the outer myoepithelial layer exhibited p63 (D), S100 expression (E), and calponin (F). Histomorphological and immunohistochemical findings confirmed the diagnosis of epithelial-myoepithelial carcinoma (EMC). In the literature, few cases reports have demonstrated distant metastasis in EMC, and therapy management remains unclear based on the limited efficacy results of recommended therapies (1,2). Because the tumors had mild to moderate FDG avidity and therapy options were limited, ^{68}Ga-fibroblast activation protein inhibitors-04 (^{68}Ga-FAPI-04) PET/CT was planned to improve diagnostic accuracy and assess eligibility for radionuclide therapy.

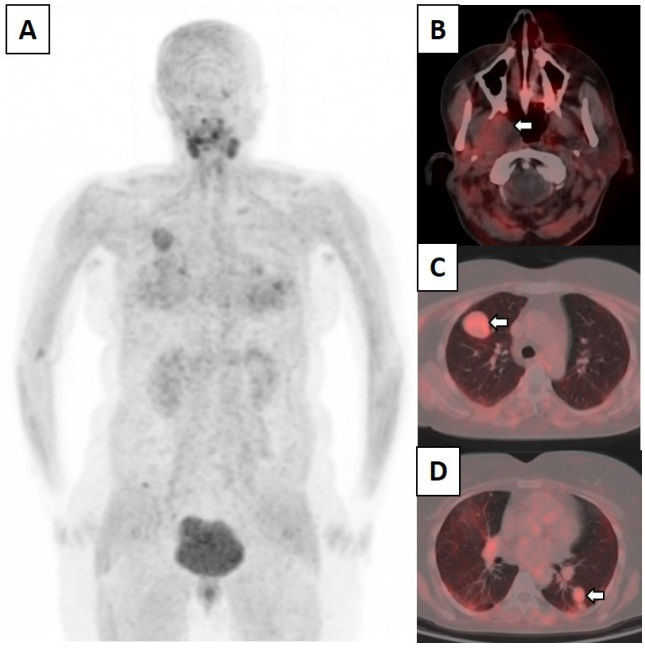

Figure 3. ^{68}Ga-FAPI-04 PET/CT (A: MIP) showed no significant uptake in the parapharyngeal mass (B: transaxial fusion, arrow), and only mild uptake was demonstrated in the lung lesions (C, D:, arrows). The patient was referred to chemotherapy regime (capecitabine + cisplatin). EMC is a very rare low-grade neoplasm of the salivary gland in which distant metastasis has been reported in only 4.5% of all cases (3). The histological diagnosis of EMC could be challenging because other benign salivary gland tumors present similar features (4). EMC mostly shows high FDG avidity based on the case reports, and it should be considered for differential diagnosis, especially in patients with a history of salivary gland surgery (5). Distant metastasis of EMC has been demonstrated in only a few case reports, and therapy options are uncertain due to the limited results in the literature (1,2). Recently, ^{68}Ga-FAPI PET/CT has opened up new opportunities, including the theognostic approach using cancer-associated fibroblasts (6). Dendl et al. (7) emphasized the value of ^{68}Ga-FAPI PET/CT in different rare malignancies, including epithelial carcinomas. Although intense FAPI expression has been demonstrated in salivary gland malignancies, especially for adenoid cystic carcinoma (8), FAPI expression has not been demonstrated in EMC. We herein present the findings of ^{18}F-FDG and ^{68}Ga-FAPI-04 PET/CT in this rare metastatic EMC case. ^{18}F-FDG PET/CT seems feasible for determining the spread of disease; however, ^{68}Ga-FAPI-04 PET/CT does not seem to have theranostic potential in EMC.

Ethics

Informed Consent: Patient consent was obtained.

Authorship Contributions

Surgical and Medical Practices: C.C., D.H.Ş., D.V.B., S.K., Concept: C.C., D.H.Ş., Design: C.C., D.H.Ş., D.V.B., Data Collection or Processing: C.C., D.H.Ş., D.V.B., S.K., Analysis or Interpretation: C.C., D.H.Ş., Literature Search: C.C., D.V.B., Writing: C.C., D.H.Ş., D.V.B., S.K.

Conflict of Interest: No conflicts of interest were declared by the authors.

Financial Disclosure: The authors declare that this study has received no financial support.

References

1. Wakasaki T, Kubota M, Nakashima Y, Tomonobe E, Mihara T, Fukushima J. Invasive myoepithelial carcinoma ex pleomorphic adenoma of the major salivary gland: two case reports. BMC Cancer 2016;16:827.
2. Pierard S, Gregoire V, Weynand B, Machiels JP. Epithelial-myoepithelial carcinoma of the submandibular gland with symptomatic lung metastases treated with chemotherapy. Eur Arch Otorhinolaryngol 2006;263:1158-1160.
3. Gore MR. Epithelial-myoepithelial carcinoma: a population-based survival analysis. BMC Ear Nose Throat Disord 2018;18:15.
4. Kusafuka K, Yamashita M, Muramatsu A, Arai K, Suzuki M. Epithelial-myoepithelial carcinoma ex-pleomorphic adenoma of the parotid gland: report of a rare case with immunohistochemical and genetic analyses. Med Mol Morphol 2021;54:173-180.
5. Takumi K, Fukukura Y, Kamiyama T, Nakajo M, Ohori J, Kurono Y, Higashi M. Epithelial-myoepithelial carcinoma of the parotid gland: correlation of dynamic magnetic resonance imaging, (18)F-fluorodeoxyglucose-

positron emission tomography, and pathological findings. Jpn J Radiol 2010;28:618-622.

6. Kratochwil C, Flechsig P, Lindner T, Abderrahim L, Altmann A, Mier W, Adeberg S, Rathke H, Röhrich M, Winter H, Plinkert PK, Marme F, Lang M, Kauczor HU, Jäger D, Debus J, Haberkorn U, Giesel FL. 68Ga-FAPI PET/CT: tracer uptake in 28 different kinds of cancer. J Nucl Med 2019;60:801-805.
7. Dendl K, Finck R, Giesel FL, Kratochwil C, Lindner T, Mier W, Cardinale J, Kesch C, Röhrich M, Rathke H, Gampp H, Ristau J, Adeberg S, Jäger D, Debus J, Haberkorn U, Koerber SA. FAP imaging in rare cancer entities-first clinical experience in a broad spectrum of malignancies. Eur J Nucl Med Mol Imaging 2022;49:721-731.
8. Röhrich M, Syed M, Liew DP, Giesel FL, Liermann J, Choyke PL, Wefers AK, Ritz T, Szymbara M, Schillings L, Heger U, Rathke H, Kratochwil C, Huber PE, von Deimling A, Debus J, Kauczor HU, Haberkorn U, Adeberg S. 68Ga-FAPI-PET/CT improves diagnostic staging and radiotherapy planning of adenoid cystic carcinomas - Imaging analysis and histological validation. Radiother Oncol 2021;160:192-201.

Interesting Image

Mol Imaging Radionucl Ther 2024;33:129-131 *DOI:10.4274/mirt.galenos.2023.99810*

Jejunal Undifferentiated Spindle Cell Sarcoma with Intussusception Revealed by ^{18}F-FDG PET/CT

^{18}F-FDG PET/BT ile Gösterilen İntussusepsiyonlu Jejunal Farklılaşmamış İğsi Hücreli Sarkom

Haiyan Li, Xia Lu

Northern Jiangsu People's Hospital, Clinic of Nuclear Medicine, Medical School of Nanjing University, Yangzhou, China

Abstract

Spindle cell sarcoma is a malignant tumor with low incidence. They can occur in the soft tissue, bone, or viscera. The characteristics of morphology, density, and metabolism of spindle cell sarcoma are related to the location of the lesion. A 61-year-old woman presented with vomiting after eating for 2 weeks. Signs of peritoneal irritation were involved, but no response for symptomatic treatment included antiemetic and antispasmodic therapy. Abdominal computed tomography (CT) indicated a mass in the intestinal tract in the pelvic cavity. Then, ^{18}F-fluorodeoxyglucose (^{18}F-FDG) positron emission tomography/CT was performed, which interestingly detected a jejunal malignancy mass in the left upper abdomen with annular high uptake of ^{18}F-FDG, which was complicated by intussusception and intestinal obstruction. Finally, the jejunal mass was pathologically clarified as an undifferentiated spindle cell sarcoma.

Keywords: ^{18}F-FDG PET/CT, jejunum, undifferentiated spindle cell sarcoma, intussusception, intestinal obstruction

Öz

İğsi hücreli sarkom düşük insidanslı malign bir tümördür. Yumuşak dokuda, kemikte veya iç organlarda oluşabilirler. İğsi hücreli sarkomun morfolojisi, yoğunluğu ve metabolik özellikleri lezyonun bulunduğu yer ile ilişkilidir. Altmış bir yaşında kadın hasta, 2 haftadır olan yemek yedikten sonra kusma şikayetiyle başvurdu. Peritoneal irritasyon belirtileri söz konusuydu ancak antiemetik ve antispazmodik tedaviye yanıt alınamadı. Batın bilgisayarlı tomografisinde (BT) pelvik kavitede bağırsaklarda kitle olduğu görüldü. Daha sonra ^{18}F-florodeoksiglukoz (^{18}F-FDG) pozitron emisyon tomografi/BT yapıldı ve ilginç bir şekilde sol üst karın bölgesinde, intussusepsiyon ve bağırsak tıkanıklığı ile komplike olan, halka şeklinde yüksek ^{18}F-FDG tutulumu olan jejunal malign kitle tespit edildi. Son olarak jejunal kitlenin patolojik olarak farklılaşmamış iğsi hücreli sarkom olduğu belirlendi.

Anahtar kelimeler: ^{18}F-FDG PET/BT, jejunum, farklılaşmamış iğ hücreli sarkom, intususepsiyon, bağırsak tıkanıklığı

Address for Correspondence: Prof. Xia Lu, Northern Jiangsu People's Hospital, Clinic of Nuclear Medicine, Medical School of Nanjing University, Yangzhou, China

Phone: +18051061486 **E-mail:** lxgf2222@163.com ORCID ID: orcid.org/0000-0002-8378-1943

Received: 27.09.2023 **Accepted:** 29.12.2023 **Epub:** 19.02.2024

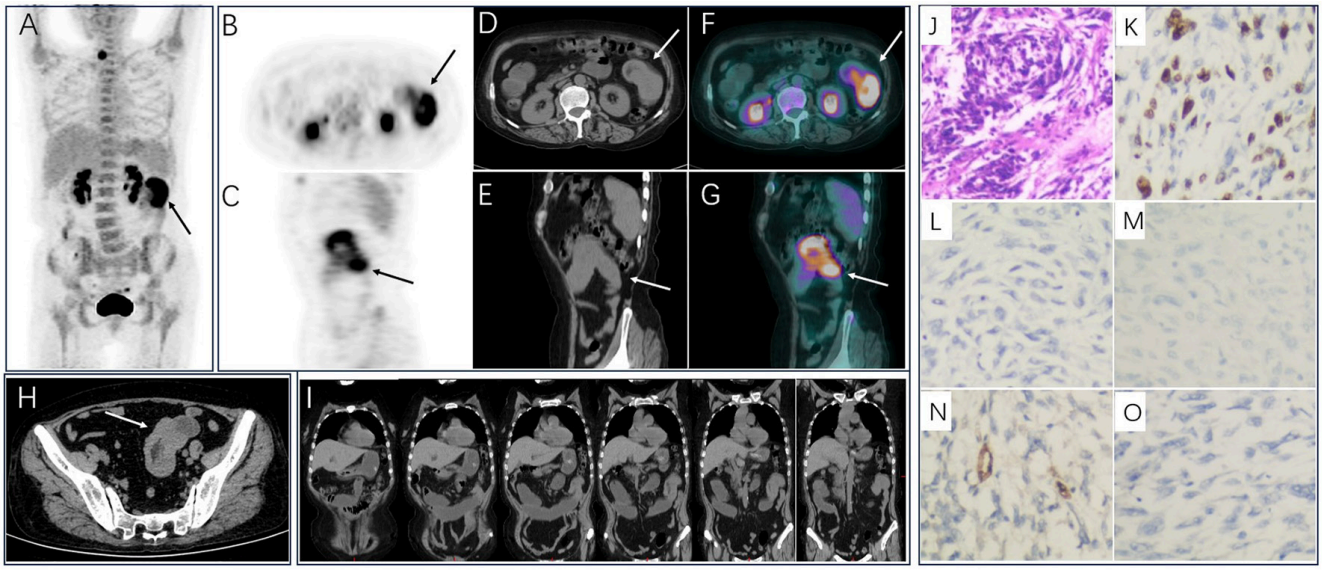

Figure 1. A 61-year-old woman presented with vomiting after eating for 2 weeks. Signs of peritoneal irritation were involved, but no response for symptomatic treatment included antiemetic and antispasmodic therapy. Abdominal computed tomography (CT) (image H) indicated a mass in the intestinal tract in the pelvic cavity (white arrow). Then ^{18}F-fluorodeoxyglucose positron emission tomography/CT (^{18}F-FDG PET/CT) was performed (60 min post-injection 335MBq) to assist differentiate the character of the mass and assess the state of the patient's illness. Maximum intensity projection ^{18}F-FDG PET image (A) showed an increased FDG uptake lesion in the left upper abdomen (black arrow). Axial and sagittal PET (B&C), CT (D&E), and fuzed CT (F&G) images of the abdomen revealed markedly increased ^{18}F-FDG uptake (maximum standardized uptake value: 10.9) corresponding to a jejunal mass with clear boundaries (arrows), which was complicated by intussusception and intestinal obstruction (I). These findings indicated that this patient could be diagnosed with a malignant small bowel tumor, and successful surgical resection was conducted shortly thereafter. Pathological examination showed spindle-shaped cell proliferation, arranged in bundles or vortices, with large and deeply stained nuclei, easy to see nuclear division (J, H&E, ×100). Immunohistochemical staining analysis revealed that the specimen was positive for Ki67 (K, ×100, 40%), CD117 (focal area), smooth muscles actin, Vim, and α-1-antichymotrypsin but negative for epithelial membrane antigen (L, ×100), S-100 (M, ×100), CD34 (N, ×100), cytokeratin (O, ×100), DOG-1, desmin, Lyso, H-caldesmon, calponin, and MyoD1. The patient's diagnosis was suggested to be undifferentiated spindle cell sarcoma. Spindle cell sarcoma is a malignant tumor with low incidence and worse prognosis with a high rate of recurrence and metastasis (1). The incidence of jejunal tumors is very low compared with other primary gastrointestinal malignancies, in which sarcoma only accounts for 12% of jejunal tumor (2), let alone undifferentiated spindle cell sarcoma of the jejunum, which is rarely reported (3,4,5). Undifferentiated spindle cell sarcoma in the jejunum can lead to intestinal obstruction (4,5). Capsule endoscopy can be used to detect lesions in the small intestine when conventional endoscopy cannot be achieved, except for intestinal obstruction formed (6). This case suggested that undifferentiated spindle cell sarcoma occurs in the jejunum with high uptake of ^{18}F-FDG as in other tissues and organs (7,8). The boundaries were clearly without lymphatic gland and peritoneum metastasized (4,5). This case reported that undifferentiated spindle cell sarcoma occurs in the jejunum with marked uptake of ^{18}F-FDG that distinguished from simple intussusception and intestinal obstruction suggested by CT scan and suggested ^{18}F-FDG PET/CT might compensate for the shortcomings of endoscopic examination in the jejunum when intestinal obstruction formed.

Ethics

Informed Consent: We obtained informed consent from study subjects for publishing their data.

Authorship Contributions

Concept: X.L., Design: X.L., Data Collection or Processing: H.L., Analysis or Interpretation: H.L., Literature Search: X.L., Writing: H.L.

Conflict of Interest: No conflicts of interest were declared by the authors.

Financial Disclosure: This work was supported by foundation of "Lvyang Jinfeng" talents attracting plan (LYJF00040) and project of Jiangsu provincial health commission (H2023055) and Jiangsu shuangchuang talent as well as the Jiangsu provincial medical key discipline cultivation unit (JSDW202251).

References

1. Fisher C. Spindle cell sarcomas. Surg Pathol Clin 2011;4:721-744.
2. Bouvier AM, Robaszkiewicz M, Jooste V, Cariou M, Drouillard A, Bouvier V, Nousbaum JB; French Network of Cancer Registries (FRANCIM). Trends in incidence of small bowel cancer according to histology: a population-based study. J Gastroenterol 2020;55:181-188.
3. Lambrinow J, Świątkowski F, Jurga M, Gajdzis P, Chabowski M. Intussusception caused by an extremely rare tumor: undifferentiated spindle cell sarcoma. Pol Arch Intern Med 2023;133:16491.

4. Cheng WH, Chen JJ, Tsou YA, Tseng GC. Jejunal undifferentiated spindle cell sarcoma with glossal metastasis. Kaohsiung J Med Sci 2012;28:120-121.
5. Gao YH, Huang JJ, Chen P. A case of non-gastrointestinal stromal spindle cell sarcoma of the small intestine. Chin J Gastrointest Surg 2018;21:1181-1182.
6. Hong SM, Jung SH, Baek DH. Diagnostic yields and clinical impacts of capsule endoscopy. Diagnostics (Basel) 2021;11:1842.
7. Treglia G, Bongiovanni M, Paone G, Ceriani L, Giovanella L. Metastatic undifferentiated spindle cell sarcoma of the thyroid gland evaluated by 18F-FDG PET/CT. Clin Nucl Med 2015;40:e208-e210.
8. Wu X, Zhang C, Huang Y, Wang H, Jiang L. Maxillofacial spindle cell sarcoma with lung metastases on FDG PET/CT imaging. Clin Nucl Med 2018;43:703-704.

Interesting Image

Mol Imaging Radionucl Ther 2024;33:132-133 *DOI:10.4274/mirt.galenos.2023.17037*

Isolated Diffuse Bone Marrow Metastases From Signet-ring Cell Gastric Carcinoma

Taşlı Yüzük Hücreli Mide Karsinomunun İzole Yaygın Kemik İliği Metastazları

Tsz-Kit Chow

Tuen Mun Hospital, Clinic of Radiology and Nuclear Medicine, Nuclear Medicine Unit, Hong Kong, China

Abstract

A 71-year-old female patient with a known history of signet-ring cell carcinoma presented with diffuse bone pain and anemic symptoms. An ^{18}F-fluorodeoxyglucose (FDG) positron emission tomography/computed tomography study revealed diffuse heterogeneous hypermetabolic sclerotic lesions in the axial and proximal appendicular skeleton. No other ^{18}F-FDG-avid lesions were detected. Subsequent bone marrow biopsy confirmed the diagnosis of metastatic carcinoma originating from the gastric primary site. Palliative treatment was initiated; however, the patient's condition deteriorated, and she succumbed to the disease two months later.

Keywords: Bone marrow metastasis, signet-ring cell gastric carcinoma, ^{18}F-FDG PET/CT

Öz

Bilinen taşlı yüzük hücreli karsinom öyküsü olan 71 yaşında kadın hasta, yaygın kemik ağrısı ve anemik semptomlarla başvurdu. ^{18}F-florodeoksiglukoz (FDG) pozitron emisyon tomografisi/bilgisayarlı tomografi görüntülemesinde, aksiyal ve proksimal apendiküler iskelette yaygın heterojen hipermetabolik sklerotik lezyonlar saptandı. Başka hiçbir FDG avid lezyonu tespit edilmedi. Daha sonra yapılan kemik iliği biyopsisi primer olarak mideden kaynaklanan metastatik karsinom tanısını doğruladı. Palyatif tedavi başlandı; ancak hastanın durumu kötüleşti ve iki ay sonra hasta öldü.

Anahtar kelimeler: Kemik iliği metastazı, taşlı yüzük hücreli mide karsinomu, ^{18}F-FDG PET/BT

Address for Correspondence: Tsz-Kit Chow MD, Tuen Mun Hospital, Clinic of Radiology and Nuclear Medicine, Nuclear Medicine Unit, Hong Kong, China
Phone: +852-38942527 **E-mail:** ctk594@ha.org.hk ORCID ID: orcid.org/0000-0002-1736-8771
Received: 17.10.2023 **Accepted:** 29.12.2023 **Epub:** 09.02.2024

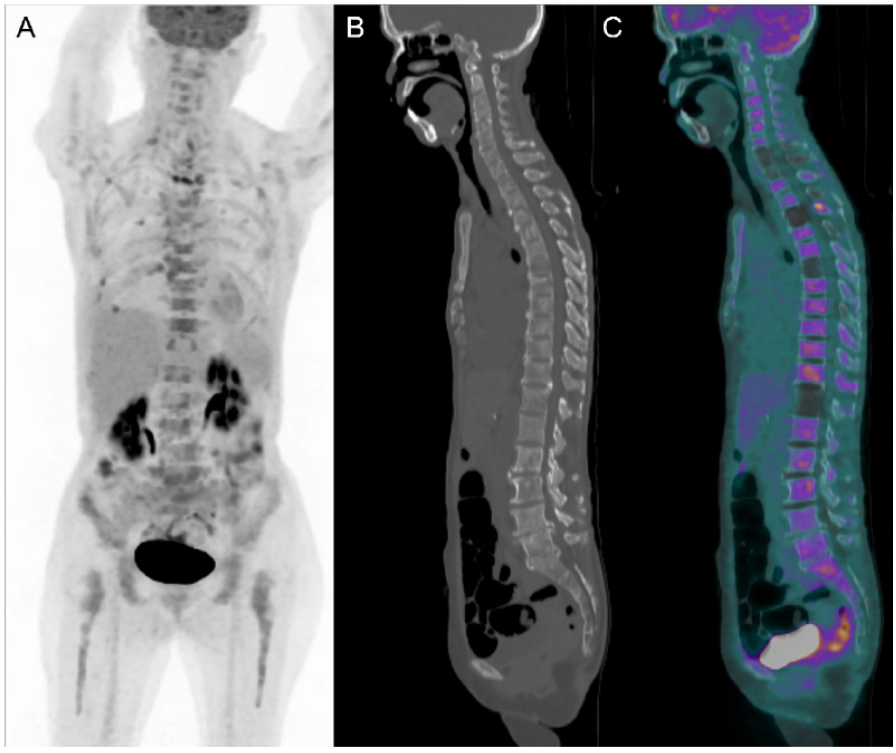

Figure 1. A 71-year-old female patient with a history of signet-ring cell gastric carcinoma (SRCC) (tumor, node, metastasis stage: pT1aN0M0) presented with diffuse bone pain and anemic symptoms. She underwent distal radical gastrectomy and extended lymph node dissection 6 years ago with no evidence of disease recurrence. She was referred for ^{18}F-fluorodeoxyglucose (FDG) positron emission tomography/computed tomography (PET/CT) for evaluation. Maximum intensity projection PET revealed diffuse heterogeneous uptake in the axial and proximal appendicular skeleton (A). Sagittal CT and fusion images demonstrated multiple mildly ^{18}F-FDG-avid sclerotic lesions in the spine (B, C). No other ^{18}F-FDG-avid lesions were detected. Subsequent bone marrow biopsy revealed metastatic carcinoma of gastric origin. She received palliative treatment and died two months later. SRCC of the stomach is a subtype of poorly cohesive gastric carcinoma, comprising 17% of all cases of gastric cancer (1). Gastric cancer is classified as SRCC if more than 50% of the tumor cells are scattered malignant cells containing intracytoplasmic mucin (2). Patients with SRCC are more likely to present at a later stage, have a poorer tumor grade, and have a similar prognosis compared with other gastric adenocarcinoma (3,4,5). SRCC of the stomach more commonly metastasizes to the peritoneum and bone and less frequently to the lymph nodes, lungs, and liver compared with other histologic types (2,6,7). Isolated diffuse metastatic involvement of the bone marrow in SRCC of the stomach is highly uncommon (8).

Ethics

Informed Consent: Informed consent was obtained from the patient.

Financial Disclosure: The author declared that this study received no financial support.

References

1. Benesch MGK, Mathieson A. Epidemiology of Signet Ring Cell Adenocarcinomas. Cancers (Basel) 2020;12:1544.
2. Zhang C, Liu R, Zhang WH, Chen XZ, Liu K, Yang K, Chen XL, Zhao LY, Chen ZX, Zhou ZG, Hu JK. Difference Between Signet Ring Cell Gastric Cancers and Non-Signet Ring Cell Gastric Cancers: A Systematic Review and Meta-Analysis. Front Oncol 2021;11:618477.
3. Taghavi S, Jayarajan SN, Davey A, Willis AI. Prognostic significance of signet ring gastric cancer. J Clin Oncol 2012;30:3493-3498.
4. Zaafouri H, Jouini R, Khedhiri N, Khanchel F, Cherif M, Mesbahi M, Daghmouri A, Mahmoudi W, Akremi S, Sabbah M, Benzarti Y, Hadded D, Gargouri D, Bader MB, Maamer AB. Comparison between signet-ring cell carcinoma and non-signet-ring cell carcinoma of the stomach: clinicopathological parameters, epidemiological data, outcome, and prognosis-a cohort study of 123 patients from a non-endemic country. World J Surg Oncol 2022;20:238.
5. Efared B, Kadi M, Tahiri L, Lahmidani N, Hassani KM, Bouhaddouti HE, Benbrahim Z, Adil IS, Chbani L. Gastric Signet Ring Cell Carcinoma: A Comparative Analysis of Clinicopathologic Features. Cancer Control 2020;27:1073274820976596.
6. Riihimäki M, Hemminki A, Sundquist K, Sundquist J, Hemminki K. Metastatic spread in patients with gastric cancer. Oncotarget 2016;7:52307-52316.
7. Zhao S, Lv L, Zheng K, Tian Y, Zheng JC, Jiang CG. Prognosis and Biological Behavior of Gastric Signet-Ring Cell Carcinoma Better or Worse: A Meta-Analysis. Front Oncol 2021;11:603070.
8. Dittus C, Mathew H, Malek A, Negroiu A. Bone marrow infiltration as the initial presentation of gastric signet ring cell adenocarcinoma. J Gastrointest Oncol 2014;5:E113-E116.

Case Report

Mol Imaging Radionucl Ther 2024;33:134-137 *DOI:10.4274/mirt.galenos.2024.89106*

Revision of the Histopathological Examination Following ^{68}Ga-DOTA-FAPI-04 PET/CT of a Breast Tumor Diagnosed as Invasive Ductal Carcinomatosis

İnvaziv Duktal Karsinoma Tanılı Meme Tümörünün ^{68}Ga-DOTA-FAPİ-04 PET/BT Sonrası Histopatolojik İncelemesinin Revizyonu

Nalan Alan Selçuk[1], Kaan Akçay[1], Gamze Beydağı[1], Ömer Sönmez[1], Serkan Çelik[2], Bala Başak Öven[2], Levent Kabasakal[3]

[1]*Yeditepe University Faculty of Medicine, Department of Nuclear Medicine, İstanbul, Türkiye*
[2]*Yeditepe University Faculty of Medicine, Department of Medical Oncology, İstanbul, Türkiye*
[3]*İstanbul University-Cerrahpaşa, Cerrahpaşa Faculty of Medicine, Department of Nuclear Medicine, İstanbul, Türkiye*

Abstract

Neuroendocrine tumors (NETs) of the breast represent 1% of breast carcinomas. Histopathological misinterpretation of breast NET is common. We present the case of a female patient who had a breast mass diagnosed as invasive ductal carcinoma initially by histopathological examination. Fluorodeoxyglucose positron emission tomography/computed tomography (FDG PET/CT) revealed 2 ametabolic hypodense liver lesions. Subsequently, the patient underwent fibroblast activation protein inhibitor (FAPI)-PET/CT, which did not reveal any FAP expression in the liver lesions, but increased FAP expression was observed in the soft tissue mass of the mesenteric root. Consequently, the pathology of the biopsy taken from the nodule in the right breast was revised, and a diagnosis of grade 2 NET was established. The benefit of FAPI-PET/CT on NETs has been previously investigated. Further prospective studies are required to establish the role of FAPI-PET/CT in NET management.

Keywords: Fibroblast activation protein, PET/CT, neuroendocrine tumor, ^{68}gallium DOTATATE

Öz

Memenin nöroendokrin tümörleri (NET), meme karsinomlarının %1'inden daha azını temsil eder. Meme NET'nin histopatolojik olarak yanlış tanı alması yaygındır. Meme kitlesi histopatolojik inceleme ile başlangıçta invaziv duktal karsinom tanısı alan bir kadın hastayı sunuyoruz. Florodeoksiglukoz pozitron emisyon tomografisi/bilgisayarlı tomografide (FDG PET/BT) 2 ametabolik hipodens karaciğer lezyonu saptandı. Akabinde hastaya fibroblast aktivasyon proteini inhibitör (FAPİ)-PET/BT tetkikinde karaciğer lezyonlarında FAP ekspresyonu saptanmazken mezenterik kökteki yumuşak doku kitlesinde artmış FAP ekspresyonu izlendi. Bunun üzerine, sağ memedeki nodülden alınan biyopsinin patolojisi revize edildi ve 2. derece NET tanısı konuldu. FAPİ-PET/BT'nin NET'ler üzerindeki faydası daha önce literatürde gösterilmiştir. FAPİ-PET/BT'nin NET'lerin yönetimindeki rolünün ortaya konması için daha fazla prospektif çalışma gerekmektedir.

Anahtar kelimeler: Fibroblast aktivasyon proteini, PET/BT, nöroendokrin tümör, ^{68}galyum DOTATATE

Address for Correspondence: Prof. Nalan Alan Selçuk, Yeditepe University Faculty of Medicine, Department of Nuclear Medicine, İstanbul, Türkiye
Phone: +90 216 578 43 53 **E-mail:** nalanselcuk@yahoo.com ORCID ID: orcid.org/0000-0002-3738-6491
Received: 15.06.2023 **Accepted:** 01.01.2024 **Epub:** 09.02.2024

Introduction

Metastatic neuroendocrine tumors (NETs) are exceedingly rare in breast cancer, representing less than 1% of all breast carcinomas (1,2). A study examining 18 cases of NETs metastasizing to the breast revealed that 62% of these tumors originated from the gastrointestinal tract and 28% from the lungs. Notably, 44% of these tumors were initially misdiagnosed as primary breast carcinoma (1). We present a rare case of metastatic NET initially reported as invasive ductal carcinoma (IDC), which was demonstrated through [^{68}Ga]gallium-fibroblast activation protein inhibitor (^{68}Ga-FAPI) positron emission tomography/computed tomography (PET/CT) and [^{68}Ga]Ga-DOTATATE PET/CT imaging.

Case Report

A 59-year-old female patient presented with a 1-year history of nausea, vomiting, and flushing. During a physical examination, a breast mass was detected, which led to a tru-cut biopsy. Histopathological analysis initially indicated IDC (Figure 1). She was subsequently referred to our clinic for staging. Fluorodeoxyglucose (FDG) PET/CT revealed a slightly hypermetabolic 7-mm nodule in the right breast and two hypodense, ametabolic liver lesions (Figure 2A). Considering the ametabolic nature of these liver lesions, lobular carcinoma was suspected, prompting [^{68}Ga]Ga-DOTA-FAPI-04 PET/CT. This imaging did not demonstrate any FAP expression in the liver lesions, but increased FAP expression was observed in the mesenteric root soft tissue mass and right breast nodular lesion (Figure 2B). Maximum standardized uptake value of uptake in the mesenteric root was 16. Upon retrospective re-evaluation of the patient's clinical findings, the mesenteric root soft tissue mass, as demonstrated by [^{68}Ga]Ga-DOTA-FAPI-04 PET/CT, along with symptoms such as nausea, vomiting, and flushing, were consistent with a diagnosis of NET. Based on these findings, the histopathological examination was repeated, and the diagnosis was revised to NET (Figure 3). In addition to revising the primary pathological sample, histopathological examination of biopsies obtained from the mesentery and liver confirmed the diagnosis of grade 2 NET. Consequently, [^{68}Ga]Ga-DOTATATE PET/CT was performed. Imaging revealed a soft tissue mass in the mesenteric root with increased somatostatin receptor (SSTR) expression, multiple SSTR-positive bone, liver, and lymph node metastases, and metastatic SSTR-positive nodules in both breasts (Figure 2C).

Informed consent was obtained from the patient for all modalities.

Literature Review and Discussion

Although the FAPI uptake pattern of NETs is not exactly established, heterogeneous uptake has been reported (3). In addition to that, [^{68}Ga]Ga-FAPI PET/CT's utility in primary and metastatic NETs was previously demonstrated in case reports (4,5,6,7). Despite the high FAP expression of the primary tumor (mass in mesenteric root) in our case, the absence of FAPI uptake by liver and bone metastases was remarkable. In this case, ^{18}F-FDG PET/CT was requested

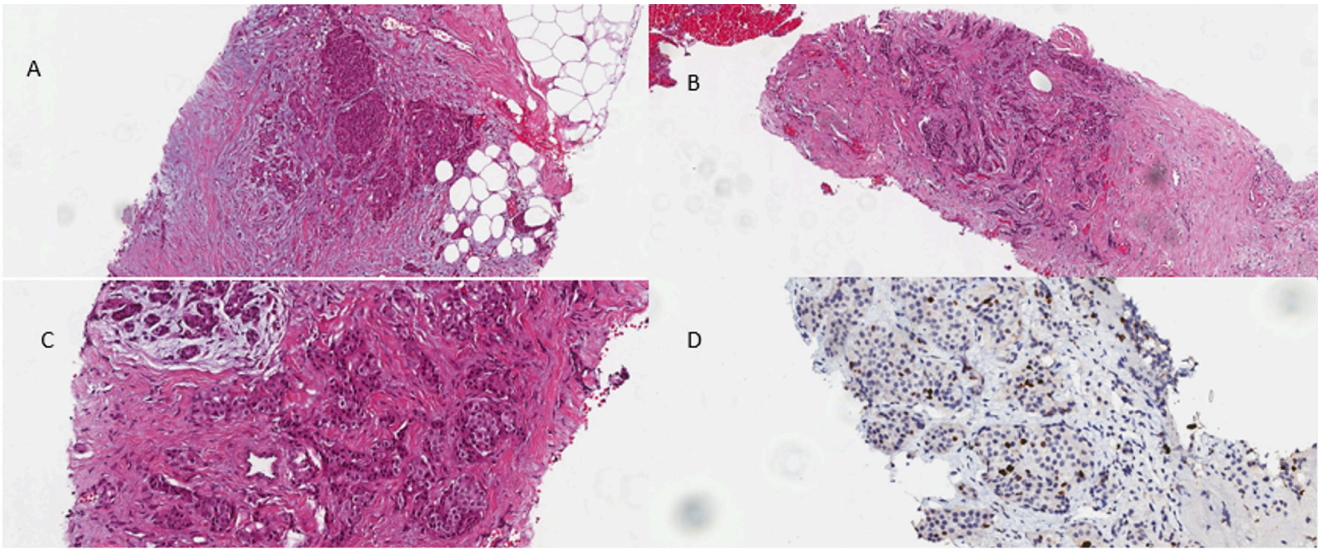

Figure 1. (A, B): Neoplastic cells are arranged in small and large nests, small groups with irregular borders, trabecula and occasional single cells in desmoplastic and collagenous stroma. Hematoxylin and eosin x100. (C): Neoplastic cells are oval-polygonal with amphophilic-granular cytoplasm, round-oval nuclei with occasional hyperchromasia and small nucleoli. Hematoxylin and eosin x200. (D): Ki67 proliferation index in the neoplasia is 10%; Ki67 x200

for the preoperative staging of breast cancer. However, the ^{18}F-FDG PET/CT scan revealed a mildly FDG-avid nodule in the right upper outer quadrant of the breast. In addition, soft tissue mass in the mesenteric root and hypodense nodules in the right hepatic lobe were FDG-negative. Concurrently, magnetic resonance imaging of the liver interpreted these liver nodules as suggestive of metastases. In the literature, there is a substantial amount of data suggesting that [^{68}Ga]Ga-FAPI PET/CT, because of the absence of background liver activity, can better detect metastatic lesions (8). Therefore, we performed [^{68}Ga]Ga-FAPI PET/CT to evaluate the possibility of lobular breast carcinoma and its metastasis in the liver. However, [^{68}Ga]Ga-[^{68}Ga]Ga-FAPI PET/CT images did not show uptake in the liver lesions. Instead, an additional FAPI-avid mass within the mesenteric root that was inseparable from the bowel loops was detected in the abdominal region, along with multiple metastatic nodules in both breast lobes, raising the suspicion that the primary tumor might not be in the breast but rather in the abdominal mass, possibly a NET. As a result, a biopsy was recommended to the lesion in the mesenteric root and revealed a diagnosis of G2 NET. Afterwards [^{68}Ga]Ga-DOTATATE PET was performed for staging of NET. [^{68}Ga]Ga-DOTATATE imaging revealed SSTR positivity in the breast, abdominal, and liver lesions. Additional multiple bone metastases were detected.

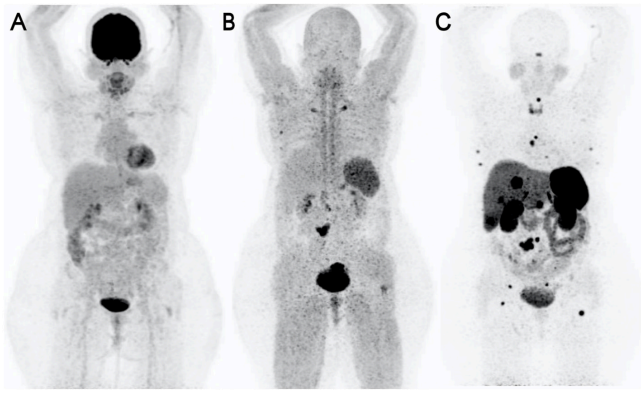

Figure 2. Cancer integrin imaging with [^{68}Ga]Ga-Trivehexin PET/CT for a patient with breast cancer and neuroendocrine neoplasm: a case both ^{18}F-FDG PET/CT and [^{68}Ga]Ga-DOTATATE positive but integrin αvβ6 negative lesion on [^{68}Ga]Ga-Trivehexin PET

PET/CT: Positron emission tomography/computed tomography, ^{18}F-FDG: ^{18}F-fluorodeoxyglucose

In this case, following these three imaging modalities, the patient's clinical diagnosis and stage changed significantly. Initially referred to our clinic for preoperative staging of breast cancer, the patient was ultimately diagnosed with metastatic NET, leading to the initiation of systemic treatment. NET metastases in the breast are quite rare, and biopsy alone may not be sufficient. In such cases, molecular imaging techniques such as [^{68}Ga]Ga-FAPI and [^{68}Ga]Ga-DOTATATE can be beneficial.

The images of PET/CTs using 3 different tracers all showed multiple foci of increased uptake of radiopharmaceutical in the abdomen and breast, in which [^{68}Ga]Ga-FAPI PET/CT displayed the highest tumor-to-background ratio. However, [^{68}Ga]Ga-DOTATATE PET/CT detected more metastatic lesions and liver and bone metastases, which were missed by both ^{18}F-FDG and [^{68}Ga]Ga-FAPI PET/CT.

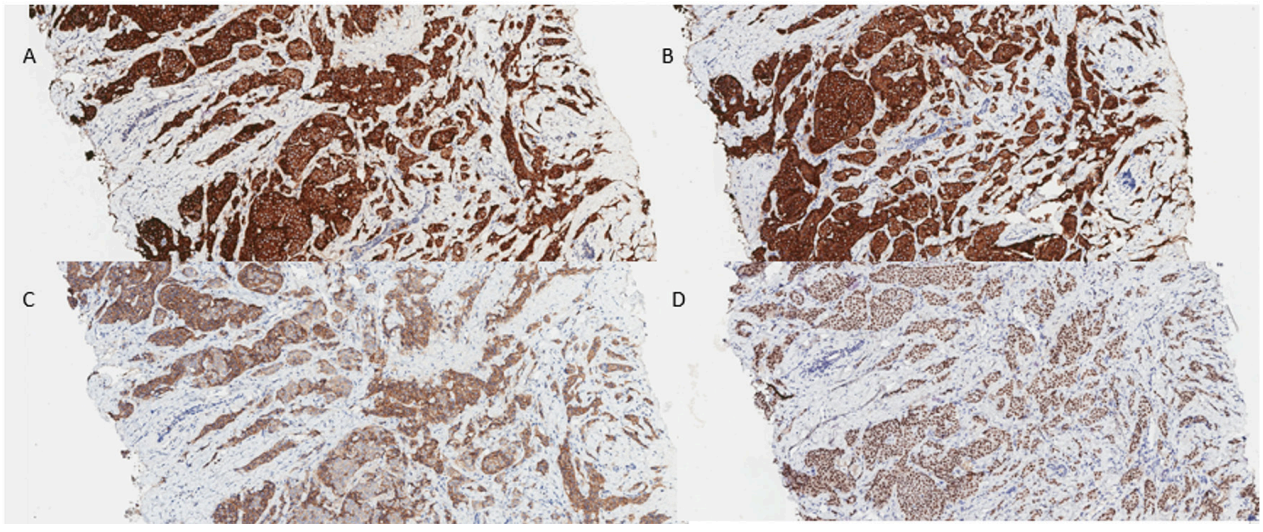

Figure 3. (A): Neoplastic cells are positive for chromogranin A; chromogranin A x100. (B): Neoplastic cells are positive for synaptophysin; synaptophysin x100. (C): Neoplastic cells are positive for CD56; CD56 x100. (D): Neoplastic cells are positive for CDX2; CDX2 x100

In this study, both modalities led to a complete change in the patient's histopathological diagnosis and, concurrently, a shift in the treatment algorithm.

Ethics

Informed Consent: Informed consent was obtained from the patient for all modalities.

Authorship Contributions

Surgical and Medical Practices: N.A.S., S.Ç., B.B.Ö., Concept: N.A.S., S.Ç., B.B.Ö., L.K., Design: N.A.S., L.K., Data Collection or Processing: K.A., G.B., Ö.S., Analysis or Interpretation: N.A.S., L.K., Literature Search: K.A., G.B., Ö.S., Writing: N.A.S., K.A., G.B., Ö.S., S.Ç., B.B.Ö., L.K.

Conflict of Interest: No conflict of interest was declared by the authors.

Financial Disclosure: The authors declared that this study received no financial support.

References

1. Perry KD, Reynolds C, Rosen DG, Edgerton ME, T Albarracin C, Gilcrease MZ, Sahin AA, Abraham SC, Wu Y. Metastatic neuroendocrine tumour in the breast: a potential mimic of in-situ and invasive mammary carcinoma. Histopathology 2011;59:619-630.
2. Adams RW, Dyson P, Barthelmes L. Neuroendocrine breast tumours: breast cancer or neuroendocrine cancer presenting in the breast? Breast 2014;23:120-127.
3. Kreppel B, Gonzalez-Carmona MA, Feldmann G, Küppers J, Moon ES, Marinova M, Bundschuh RA, Kristiansen G, Essler M, Roesch F, Gaertner FC. Fibroblast activation protein inhibitor (FAPi) positive tumour fraction on PET/CT correlates with Ki-67 in liver metastases of neuroendocrine tumours. Nuklearmedizin 2021;60:344-354.
4. Kömek H, Gündoğan C, Can C. 68Ga-FAPI PET/CT Versus 68Ga-DOTATATE PET/CT in the Evaluation of a Patient With Neuroendocrine Tumor. Clin Nucl Med 2021;46:e290-e292.
5. Cheng Z, Zou S, Cheng S, Song S, Zhu X. Comparison of 18F-FDG, 68Ga-FAPI, and 68Ga-DOTATATE PET/CT in a Patient With Pancreatic Neuroendocrine Tumor. Clin Nucl Med 2021;46:764-765.
6. Wang H, Du Z, Huang Q, Ren S, Guan Y, Xie F, Lu L, Zhu W. The superiority of [^{68}Ga]Ga-FAPI-04 over [^{18}F]-FDG in a case of neuroendocrine tumour with hepatic metastasis. Eur J Nucl Med Mol Imaging 2021;48:3005-3006.
7. Ergül N, Yılmaz B, Cin M, Çermik TF. 68Ga-DOTA-FAPI-04 PET/CT in Neuroendocrine Carcinoma of the Liver With Elevated AFP Level: Comparison With 18F-FDG PET/CT. Clin Nucl Med 2022;47:e29-e31.
8. Giesel FL, Kratochwil C, Schlittenhardt J, Dendl K, Eiber M, Staudinger F, Kessler L, Fendler WP, Lindner T, Koerber SA, Cardinale J, Sennung D, Roehrich M, Debus J, Sathekge M, Haberkorn U, Calais J, Serfling S, Buck AL. Head-to-head intra-individual comparison of biodistribution and tumor uptake of ^{68}Ga-FAPI and ^{18}F-FDG PET/CT in cancer patients. Eur J Nucl Med Mol Imaging 2021;48:4377-4385.